MODELING of the DYNAMICAL EVOLUTION of CLASSICAL RADIO SOURCES

Elżbieta Kuligowska

Contents

Outline of the Thesis

Even after a few decades of research and investigations, the dynamical evolution of powerful radio galaxies is still far away of full understanding. The classical dynamical approach to a description of the interaction between the "light" relativistic jets, carrying an outstanding amount of energy from the Active Galactic Nucleus (AGN) and interacting with the external gaseous environment, cannot provide an unique solution for a number of detailed parameters describing the underlied physical processes. The problem is that besides the observed linear size of a source (although projected on the sky) that can be interpreted as a length of the jets, the above processes result in time-dependent shape of the radio spectrum of a given source.

All existing analytical models of dynamical evolution of classical radio sources are based on some uncertain assumptions about, for example: 1) initial power-law energy spectrum, 2) equipartition of energy between the relativistic electrons and magnetic field, 3) possible reacceleration of these electrons, 4) participation of protons in the energy losses. However, recently these models can be partly confined by X-ray mapping, unfortunately only for nearby and the brightest sources. In spite of the above, the existing models suffer other severe deficiencies. All of these models assume: 1) exponential profile of the ambient environment (simplified King's model, King 1972), which is valid for a limited external halo and is not justified for the largest (thus old) radio galaxies, 2) continuous injection of energy via the jets of constant power that is evidently not the case for the observed, so called double-double radio structures in which two pairs of twin lobes are observed and interpreted by a termination of the primary jet activity and the appearance of a new, secondary activity.

In this Thesis I address some of the above issues and modify the basic analytical model of Kaiser, Dennet-Thorpe and Alexander, 1997 (hereafter referred to as KDA), as well as compare observed spectra of a few exemplary radio sources with predictions of both the KDA model and its modified versions.

The outline of the Thesis is as follows: Section 1 summarize different apparent morphologies of radio sources and define the type of sources for which analytical models of their dynamical evolution is considered here. Section 2 outlines physical processes resulting in the observed morphology, brightness distribution, and spectral shape of the sources. Section 3 describes the existing dynamical models of radio galaxy's evolution and its limitation due to the real examples of observed radio galaxies. Section 4 presents the application of original KDA model in case of studying the observed asymmetries of FR II type radio sources. Section 5 is dedicated to the revision of the existing model, assuming that radio sources evolve in two-media environment. Section 6 describes an attempt to extend the classical KDA model of the source's evolution with for assumed continous nuclear activity to its generalization applicable to the case of sources with non-continous injection of relativistic electrons. Finally, Section 7 presents application of the extended model to a few real radio galaxies with steeply bent high-frequency spectra.

PART I

1 Types of radio sources

All existing radio sources can be defined as celestial objects that emit rather strong radio waves. However, they are basically divided into two general cases. The first case includes all of "normal" galaxies in which the dominant radiation in the radio domain results from the star-formation processes, supernovae remnants (e.g. Cassiopeia A), and the existence of clouds of ionized hydrogen (HII regions). The angular extent of the source in this case does not exceed a solid angle of the optical galaxy itself. The second case consists of the galaxies with the dominant radio emission originating from the nuclear activity - so-called classical radio sources. Their optical spectra are not the simple superpositions of the spectra of particular stars in the galaxy, but show also characteristic emission lines due to the high-energy processes taking place in their centers. Such a classical radio source has linear, elongated, so-called "double" structure extending usually far outside the parent galaxy.

Classical radio sources had been divided by Fanaroff and Riley (1974) into two morphological types: FRI and FRII. This classification in based on the observed morphology of the large-scale radio structures. The FRI type radio sources are brighter towards its center, while FRII sources are the brightest at the edges or their two radio lobes. The two FR types are also broadly separated by the luminosity; FRII sources are more luminous in the radio wavelengths than FR I types. The original dividing line was placed at 5×10^{25} W Hz^{-1} at observing frequency of 178 MHz. This division is due to the efficiency of the energy transport into the source's radio structure - the central engines of FRII sources supply the lobes with the energetic particles more efficiently than in the FRI case. The jets of the latter appear to be subsonic close to the nucleus and radiate a significant amount of their total energy on their way to the radio lobes. In turn, the jets in FRII sources remain relativistic on their entire length, and the so-called hot spots visible on the ends of the radio lobes can be interpreted as the manifestation of supersonic shocks formed when the jet abruptly terminates encountering the external intergalactic medium of some density and pressure.

Figures (1) and (2) show archetypes of the above two morphologies: radio galaxies 3C405 (Cygnus A) of FR II type and 3C31 of FRI type. The content of this thesis is related entirely to the FRII type of radio sources.

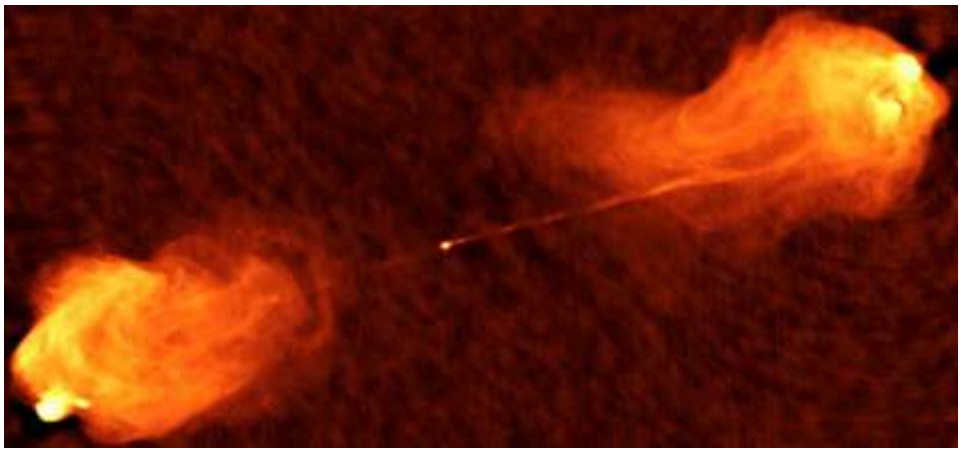

Figure 1: Example of FR II type radio source: Cygnus A radio map at 5 GHz (VLA). Image courtesy of NRAO/AUI.

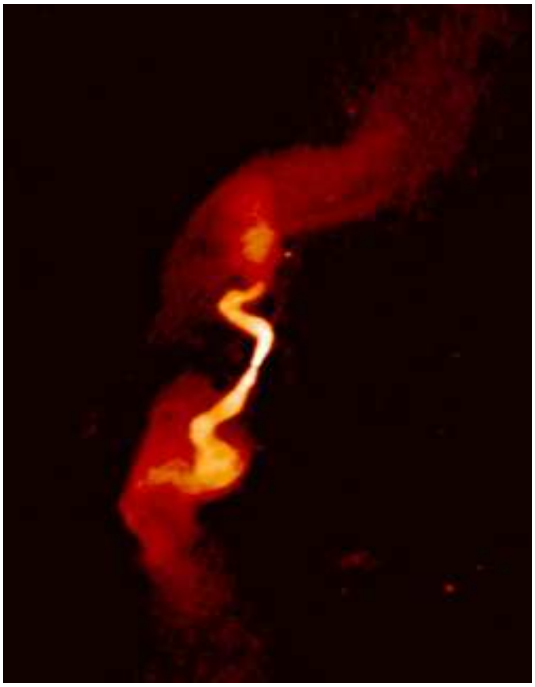

Figure 2: Example of FR I type radio source: 3C31 radio map at 5 GHz (VLA). Image courtesy of NRAO/AUI.

1.1 FRII type radio sources

FR II type radio sources are composed of double, ellipsoidal, radio-emitting regions (so-called radio lobes) situated more or less symmetrically on the both sides of their host galaxies which in most cases are large elliptical galaxies containing super massive black holes (SMBH) of masses $10^6 - 10^9 M_\odot$ in their center. These lobe structures are originated from twin jets outflowing in opposite directions from the Active Galactic Nucleus (hereafter referred to as AGN). The radio emission of these lobes results from the electrons ejected at nearly the speed of light through a long jet from the core of the galaxy and deposited in radio lobes. The electrons are trapped by the magnetic field around the galaxy and produce radio waves. In most of the powerful observed FR II sources their jets end in significantly brighter regions situated at the ends of the lobes - hot spots clearly seen in Figure (1).

The most famous example of FR II type radio sources is Cygnus A. It has been discovered by Grote Reber in 1939. Cygnus A is one of the strongest radio sources seen from the Earth and, along with Cassiopeia A and Puppis A, had been the first radio source identified with optical source (Baade and Minkowski, 1954) and, so, the first even observed classical radio galaxy.

1.2 Size of FR II type radio sources from Gigahertz-Peaked-Spectrum Sources to Giant Radio Galaxies

FRII type radio galaxies show a large variety of their linear sizes. The size of radio galaxies is defined here as the linear distance between the bright edges of the both radio lobes. These sizes range from less then 100 pc - Gigahertz-Peaked-Spectrum (GPS) sources up to about 4 Mpc - Giant Radio Galaxies (GRG). Between these extreme cases we observe a lot of medium size radio galaxies. Their typical size is about 100 to 400 kpc. In general, this size is dependent of the age of the source - the older it is, the more time the jets had to act forming a large radio structure. On the other side, the source's large size may result from the locally occurred low density of the ambient medium in which the source evolves (cf. Section 3.1).

GPS sources have a maximum of flux density in their radio spectra at about 1 GHz and linear sizes not exceeding 1 kpc. They are considered to be young, recently formed sources. Several studies show that they probably expand during their time evolution and transform to Compact Steep Spectrum (CSS) sources with linear sizes of about 10 - 15 kpc. Then, in a next stage of the evolution, they transform into the phase of typical FR I of FR II type radio source. In a specific condition they can evolve to the ultimate phase, i.e. GRGs. They are defined as radio sources with linear sizes of at least 1 megaparsec (for a fixed Hubble Constant H_0=0.71 km s^{-1}Mpc^{-1} and the cosmological parameters $\Omega_m = 0.27$ and $\Omega_\Lambda = 0.73$ (ΛCDM model). GRGs are interesting because of the fact that their existence brings out important questions about their evolution,

age, and the origin of so large sizes. GRGs are usually much older than typical radio galaxies what suggests they can be the final stage of source's evolution.

Until recently the largest radio galaxy was 3C236 that features a "double-double" morphology consisting of the giant relic of ∼4.4 Mpc size and an inner structure of ∼2 kpc size which is a young, compact steep spectrum source. (Willis, Strom & Wilson 1974.) However, in 2005 the larger radio galaxy have been discovered. J1420-0545 has its linear projected size of 4.69 Mpc (Machalski et al. 2008). Despite of this, J1420-0545 is also interesting due to its relatively high redshift ($z = 0.3067$).

An analysis of the reached sources' size (and their age) in the function of their temporary radio luminosity was considered by Kaiser & Best (2007). A summary of their considerations is given in Section 2.2.

1.3 Cycles of the activity

The activity of radio galaxies results from the processes of accretion of a matter on the black hole with magnetic field and angular momentum. This activity evidently cannot be infinite; it can be stopped after a time defined as "jet cut-off" time. It was estimated to be no longer then about 10^8 years (Komissarov & Gubanov 1994). When the activity ends even temporarily, the lobes are not longer powered with the inflow of relativistic particles, so as the result, the luminosity of the radio structure tends to cease. This effect is observed mostly on higher radio frequencies (ν>1000 MHz) and this effect seems to be common in the case of old, large-sized radio sources. In a study of the radio structures of some giant radio galaxies, Subrahmanyan, Saripalli & Hunstead (1996) drew attention to a variety of morphological features in the GRGs which were indicative of interrupted or episodic nuclear activity. It implies that GRGs may had attained their large sizes as a result of restarting of their nuclear activity in multiple phases.

Observations also indicate the existence of some specific case of radio sources - so called Double - Double Radio Galaxies (DDRGs). Their extended radio structures consist of the inner, younger double structures with almost pure power-law spectra and the outer, larger, steepened spectrum structure, considered to be the older one. Observations suggest also that such double-double structures predominantly occur in the case of the largest radio galaxies. However, only a small fraction of GRGs has double-double structures (Schoenmakers et al. 2000). Studies of the possible nuclear recurrence in radio sources are in their early days and the role of such a recurrent activity in the formation of GRGs should be enlightened.

2 Theoretical basis

2.1 Physical processes in the FRII type sources

The radio galaxy's activity connected with jets formation results from the processes of accretion of a matter on the super massive black hole (hereafter referred to SMBH) with magnetic field and angular momentum. AGNs are characterized by a high rate of the accretion of gaseous matter situated close to the central SMBH. Accreted matter forms so-called accretion discs where the rotational energy of the SMBH is transformed into plasma's internal energy, and then, radiated in the wide range of the electromagnetic spectrum. Magnetic field of the SMBH links the accretion disc with the plasma placed outside the ergosphere. That implies that the high fraction of the plasma can be accelerated in the direction defined by the spin of the AGN.

Jets (and double radio structures) are formed only in some fraction of all observed AGNs. Wilson & Colbert (1995) and Blandford (1999) suggest that jets of so-called radio loud AGNs are only produced in the case of central SMBH with very strong magnetic field and high spin. High values of the spin results probably from the merging event of two SMBH (Merrit & Ekers, 2002.) Physical processes leading to the observed structure of FR II type radio source are determined by so-called "Standard AGN model" (Blanford, Rees & Scheuer 1974). The schematic diagram of the source's components is shown on Figure (3).

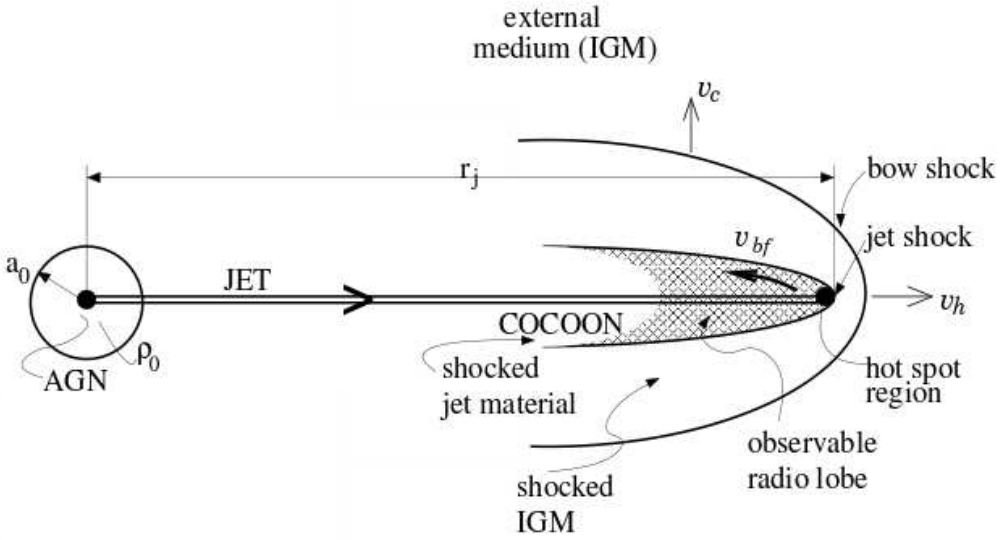

Figure 3: Schematic diagram of the structure and physics of FR II type radio source.

A well collimated jet composed of relativistic particles starts its travel encountering the host galaxy, then the medium of the cluster containing that galaxy, and finally it may reach the Intergalactic Medium (hereafter IGM) whose density can be higher than the density of the jet. Interaction of the jet with those media produces a bow shock. This shock form an interface between the shocked and the unperturbed external medium. A compression of relativistic jet material has place at hot spots, the brightest regions of the ends of the jets where external medium interacts with the jet, resulting in medium's particles accelerations after their transition through the bow shock. The jet's power depends on the total AGN rotational energy. The higher this energy is, the faster the relativistic particles of the jets move. If the AGN is relatively weak, the radio lobes are powered with poorly collimated jets in which turbulent forces occur and the velocity of the relativistic particles slows down.

2.2 Energy losses

The FR II type sources have predominantly power-law spectra. Non-thermal continuum radio emission of the lobes is due to both synchrotron process and inverse-Compton scattering of ambient photons of the cosmic microwave background (CMBR). The synchrotron radiation arises from ultra relativistic charged particles (with Lorentz factor of $\gamma \sim 10^4$) that interact with the magnetic field. This emission in highly polarized and can be observed within the entire electromagnetic spectrum, so it can be easily recognized. According to classical electrodynamics the life-time of relativistic electrons emitting medium and short radio waves has to be relatively short. Because the radio lobes are stable, long-living structures (as the observations indicate), they have to be continuously powered with the amounts of new particles. The source of these particles can be only the central part of the galaxy - AGN. Due to so-called synchrotron losses, the most energetic particles loose their energy in the fastest rate. It implies that, in the absence of the constant injection of the new particles, synchrotron losses in the radio lobes result a violent steepening of the observed radio spectra of the sources. Most energetic electrons preferentially emit at high frequencies, so the high-frequency part of the spectrum rapidly steepens and finally cuts off.

The Inverse Compton effect originates from the interaction of the jet's relativistic particles with CMBR photons. According to Kardashev (1962), this process need to be taken into account in the analysis of the source's total energetics, as well as the adiabatic expansions of the lobes (resulting in both energy losses and gains), Coulomb losses (occurring when relativistic particles collide with thermal electrons of a given density), and energy acquisition by systematic or stochastic acceleration. It had been proved that Coulomb losses play a major role in total energy losses only at very low energies ($\gamma < 10$). Both radiative and adiabatic losses are dominant at higher particle's energies, especially for $\gamma > 10^3$ (Murgia 1996).

As it has been mentioned in Section 1.2, Kaiser & Best (2007) analyzed evolution

of the luminosity (L) as the function of the source's size (D). Their $L - D$ diagram is reproduced in Figure (4).

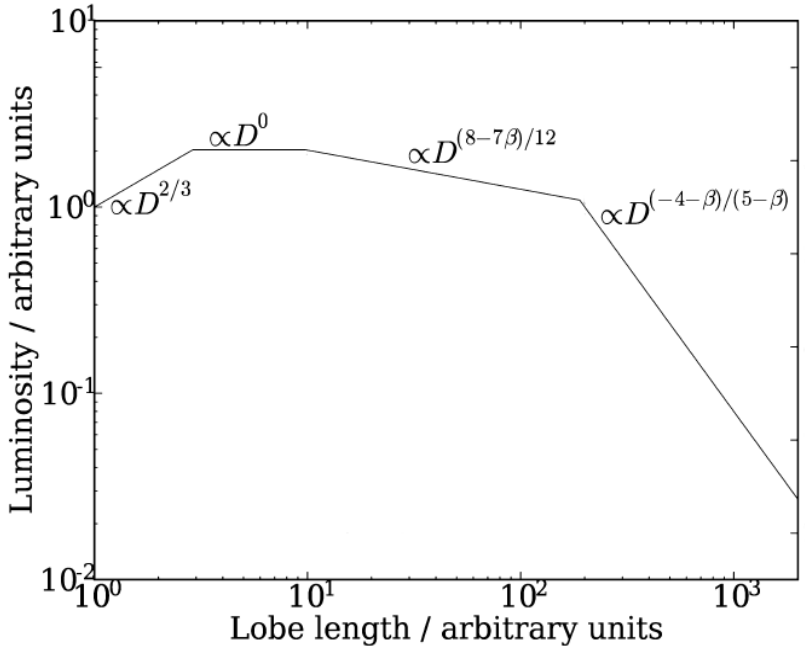

Figure 4: The FR II type source's luminosity evolution of a lobe.

The source's luminosity is linked to a stage of the its life and the dominant energy losses at a this stage. For the case of dominant adiabatic loses, the radiation losses could be neglected. In this regime the radio luminosity depends on sources size as $L \propto D^{(8-7\beta)/12}$. It implies that at this stage the expected luminosity can decrease or increase depending on whether $\beta > \frac{8}{7}$ or $\beta < \frac{8}{7}$, respectively. The synchrotron losses are the most important at the early time of source's life because the energy density of the magnetic field in which particles radiates decrease while the source grows and grows older. The radio luminosity in this regime is the constant function of its size $L \propto D^0 \sim$ const. The external density profile is now approximated by a power law and the relation between the length D and the source age t depends on the value of the power-law exponent Îš. In this regime synchrotron losses dominate over the Inverse Compton effect.

As the magnetic field decreases due to the ageing of the source, Inverse Compton losses remain constant and finally dominate over synchrotron losses. At this phase very strong total energy losses are observed $L \propto D^{(-4-\beta)/(5-\beta)}$ (cf. Figure (4)).

2.3 Source's sizes vs. other physical factors

The lobe's length is not only the simple function of its age. The total size depends also on amount of energy released from the AGN and the properties of the IGM in which the source evolves. For example GRGs are only a fraction of 6% of the total population of luminous radio galaxies (Laing, Riley & Longair, 1983). It may imply that their enormous sizes result from the "density voids" in the IGM. Additionally, only about 10% of known GRGs lie at redshift larger than 0.5. The maximum linear size of observed radio galaxies decreases as $D \propto (1+z)^{-3}$ (Gopal-Krishna & Wiita 1987). This fact is in a good agreement with the theory assuming that in the adiabatically expanding Universe, filled up with hot, uniform IGM, its density increases as $\varrho_{\mathrm{IGM}} \propto (1+z)^3$, (Kapahi 1989) and its kinetic temperature grows up proportionally to $T_k \propto (1+z)^2$. It implies that the pressure of IGM changes as $p \propto (1+z)^5$ (Cotter 1998). The pressure of the external medium likely decides how far the radio structure can expand. That explain why most of the GRGs are situated close to us. However, finding GRGs at much higher redshift may prove that parts of the IGM, with significantly lower density then an average one, are also in early cosmological epochs. For this reason GRGs are useful tool for studying the evolution of radio sources itself, as well as the cosmological evolution of the IGM - especially its density and homogenity.

3 Analytical models of FRII type radio sources

All analytical models take into account known physical processes occuring in FR II type radio sources. They characterize these sources in terms of their dynamics and energetics connected to the luminosity evolution. All of them originate from the "standard model" for double radio sources (e.g. Blandford & Rees 1974) in which lobes are composed of a shocked jet and IGM material. The axial length of a lobe results from the balance between the jet's thrust and the ram pressure of the external medium, and its width is a function of the jet's particles internal pressure.

3.1 Source dynamics

This balance is a base for the source's dynamics described by the more sophisticated analytical model of Kaiser & Alexander (1997; hereafter referred to KA). The jets thrust, Π_{jet}, and its balance with the ram pressure of the gaseous environment is given by

$$\Pi_{jet} \sim \left(\frac{Q_{jet}}{v_{jet}}\right) \approx \rho_a v_h^2 A_h, \tag{1}$$

where Q_{jet} and v_{jet} are the jet's power and speed; the later one is assumed to be close to the speed of light ($v_{jet} \approx c$). ρ_a is the ambient density, v_h is velocity of the jet's head (cf. Figure (3)), and A_h is the cross-section area of the bow shock there the time-averaged Π_{jet} is discharged over.

Transforming Eq.(1) we have

$$v_h = \frac{d}{dt} r_j \approx \left(\frac{Q_{jet}}{\rho_a c A_h}\right)^{1/2}. \tag{2}$$

Taking into account that A_h is an increasing function of time (cf. Murgia 1996), and assuming that the density distribution of the unperturbed ambient gas surrounding the radio sources has a power-law radial density distribution (the simplified King's (1972) profile) scaling with the distance r from the center of the host galaxy as:

$$\rho_a(r) = \rho_0 \left(\frac{r}{a_0}\right)^{-\beta}, \tag{3}$$

where ρ_0 is central density of the radio core, a_0 is its radius, and β is exponent of the power-law density profile in the King's model. Integration of Eg.(2) gives the total length of the jet at a given age t as

$$r_j(t) = c_1 \left(\frac{Q_{jet}}{\rho_0 a_0^{\beta}} \right)^{1/5-\beta} t^{3/5-\beta}. \tag{4}$$

where r_j is identified with one half of the source's linear size, $r_j = D/2$. A value of the coefficient c_1 is a complex function of equations of state of the unperturbed external medium and shocked jet and surrounding environment material (cf. Kaiser & Alexander 1997). The shocked jet material inflates a space volume (hereafter referred to as cocoon) within, so-called, contact discontinuity. The observed lobes of an FR II type source are identified with the radiating parts of this cocoon (cross-hatched area in Figure (3)).

The lobe expand due to the hotspot plasma pressure, p_h, and the cocoon pressure itself - p_c. The pressure ratio is proportional to the axial ratio - R_t, defined as the ratio of lobe's length to its base diameter:

$$P_{hc} \equiv \left(\frac{p_h}{p_c} \right) \simeq 4\, R_t. \tag{5}$$

In particular, the coefficient c_1 is dependent on P_{hc} also (cf. Eqs. (32) and (38) in KA). It is worth notice that in the KA model the rate at which particles are transported from the AGN to the hot spots is constant during the lifetime of the source. If two of its basic free parameters: Q_{jet} and $\rho_a(r) = f(\rho_0, \beta)$, are specified, this simplified model predicts evolution of source's geometrical parameters only.

3.2 Source energetics and luminosity evolution

In order to provide another, independent relation between the parameters Q_{jet} and ρ_0, Kaiser, Dennett-Thorpe & Alexander (1997) combined the pure dynamical KA model with the analytical model (hereafter KDA model) for the total energetics of a FR II type source, i.e. for expected radio emission of its lobes (or cocoon) under influence of the energy loss processes: adiabatic losses due to their expansion, synchrotron emission in the magnetic field, and inverse Compton scattering of the CMBR photons. The exact formula for the radio power is not an analytically solvable integral in this model, but it can be solved numerically for assumed values of the model free parameters, tracing all of the source's energy losses.

The initial energy distribution of injected particles is given by $n(\gamma_i) = n_0 \gamma^{-p}$. The additional model free parameteres that have to be fixed are: a_0, β, θ (the inclination angle of the jet axis to the observer's direction of sight), γ_{min} and γ_{max} (Lorentz factors determining the energy range of the relativistic particles), p (initial power-law exponent), Γ_j, Γ_a, Γ_B and Γ_c (adiabatic indices in the equation of state for the jet material,

the external medium, "magnetic" fluid, and the source as a whole, respectively, and the ratio of the energy density of the magnetic field and relativistic particles, given by $r = u_B/u_e = (1+p)/4(1+k')$, assuming energy equipartition condition. k' is a ratio of thermal to relativistic particles, and $p = 2\alpha_{inj} + 1$.

An ensemble of $n(\gamma)$ relativistic electrons with Lorentz factor γ, placed in a volume V, in the presence of magnetic field B, emits synchrotron power per unit frequency and unit solid angle according to the relation:

$$P_\nu = \frac{\sigma_T c}{6\pi} \frac{B^2}{2\mu_0} \frac{\gamma^3}{\nu} n(\gamma) V, \tag{6}$$

where σ_T is the Thomson cross-section and μ_0 is the permeability of free space. These relativistic electrons are supposed to be injected into the lobe from the hotspot by its head (extended region of turbulent acceleration around the hotspot.) Radio spectrum evolves with time due to energy losses. The process of slowing down the particles the Lorentz factor γ can be described by the formula:

$$\frac{d\gamma}{dt} = -\frac{a_1}{3}\frac{\gamma}{t} - \frac{4}{3}\frac{\sigma_T}{m_e c}\gamma^2(u_b + u_c), \tag{7}$$

where the first term (from the right) refers to the adiabatic losses in the expanding lobes and the second - to the combined synchrotron and inverse Compton effect radiation. In this formula, m_e is the electron mass, u_b - energy density of the magnetic field, and u_c - energy density of CMBR.

Integrating Eq.(7) over time and performing some other transformations one finally obtains the formula for the radio power of infinitesimal volume elements of the cocoon at given frequency. By summing the total contribution of all of those elements we can numerically calculate this integral over the injection time t_i. However, t_i cannot be less than a minimum injection time, t_{min}, at which the cocoon material (still radiating at frequency ν) has $\gamma_i \leq \gamma_{max}$. Thus:

$$P_\nu(t) = \int_{t_{min}}^{t} dt_i \frac{\sigma_T c r}{6\pi\nu(r+1)} Q_{jet} n_0 (4R_t^2)^{(1-\Gamma_c)/\Gamma_c} \times \frac{\gamma^{3-p} t_i^{a_1/3(p-2)}}{[t^{-a_1/3} - a_2(t,t_i)\gamma)]^{2-p}} \cdot \left(\frac{t}{t_i}\right)^{-a_1(1/3+\Gamma_B)}. \tag{8}$$

As it have been mentioned, there are examples of more advanced dynamical models based on the original KA model. They are all related to the same basic consideration of source's length vs. age dependence and the mechanism of radiation and radiative losses. The major differences are due to the initial energy distribution of injected particles.

The KDA model assumes that there is a constant injection index, p, for the power-law energy distribution defined above. In this simplified scenario, the radiating particles are injected from the hotspot into the lobe. Some authors argue that this approximation may be incorrect. For example, in the BRW (Blundell, Rawlings & Willot 1999) model, this injection index is not expected to be constant and varies between the different energy regimes due to some break frequencies. On the contrary, the MK (Manolakou & Kirk 2002) assumes that this index is also constant, but the particle's behaviour is more complicated than in a case of pure KDA model and they are additionally reaccelerated in the lobe's head. The both models are widely described and compared by Barai & Wiita (2006).

3.3 Determining dynamical age and other physical parameters for real FRII type radio sources

The original KDA model allows prediction of the jets length (i.e. the linear size of a source) and its radio power at a given frequency. This is possible if the values of the all free parameters of the model are specified. However, a special tool has been desired to solve the "reverse problem", i.e. to estimate model's physical parameters for a real radio source with all the observational parameters derived from radio maps: the size and axial ratio of its lobes and their radio spectrum, i.e. the luminosity at a number of observing frequencies.

In order to solve such "reverse problem" Machalski, Chyży, Stawarz & Kozieł (2007a; hereafter referred to as MCSK) elaborated the algorithm "DYNAGE" which allows to derive values of four of the source's unknown parameters (i.e. age, jet power, central density and the initial injected energy) from the fit to the known observables (source's size, volume, the radio power at given frequency and the shape of the spectrum). This numerical approach demands multifrequency radio observations including at least three different flux densities embracing possibly wide range of the radio spectrum. The "DYNAGE" algorithm demands also fixing values of the remaining free model parameters, i.e. values of a_0, β, θ, γ_{min}, γ_{max}, Γ_j, Γ_a, Γ_B, Γ_c, and k' indicating ratio of energy density of the thermal particles to that of the relativistic particles. Setting all of these parameters, one can estimate values of t, Q_{jet}, ρ_0, and α_{inj} for every individual FR II type radio source.

Especially, the dynamical age of a given source can be estimated. The "DYNAGE" algorithm provides the recipe for fitting "the best" model radio spectrum to the observed data. This procedure is shown in details in MCSK. So-called "age solution" is found knowing that numerically fitted values of the Q_{jet} increase with decreasing age and, on the contrary, ρ_0 tend to increase with age on the $Q_{jet} - \rho_0$ diagram (cf. their figure (1)). Therefore the crossing point for all of the frequency curves on these diagrams (or, the numerically fited age corresponding to the minimum dispersion of these values) defines the most physical "age solution" for a given set of the assumed values

of model free parameters. However, their calculations indicate that this "age solution" depends significantly on α_{inj} value. Thus, the "DYNAGE" algorithm predicts the "best age solution" resulting from the fit to the best "effective" value of the initial energy of injected particles providing a minimum of the jet's kinetic energy, $Q_{jet} \cdot t$

3.4 Limitations of the KDA model

The KDA model suffers three serious limitations in its descriptions of the physical processes and conditions governing the dynamical evolution of radio sources. These are:

1. Negligence of observed asymmetries in the lobe's length, axial ratio, and radio spectrum,

2. Unlimited decrease of the external density profile,

3. Constant relativistic particles energy distribution and the jet power during the lifetime of a source.

3.4.1 Asymmetry of radio sources

According to the classical approach based on standard model of FR II type sources, every radio source for which modeling is performed is strictly symmetrical. Therefore, the KDA model assumes that the two lobes have the same length, axial ratio, and total radio power at a given frequency. In the case of real radio sources more or less evident asymmetries in both: lobe's length and their radio luminosity are observed. In the standard modeling these differences are neglected and the values of D and P_ν, the opposite for lobes, are averaged. This simplification implies that estimated values of t, Q_{jet} and ρ_0, as well as β exponent, are always equal for both lobes of the source. In the Section 4, I analyse dependences of the ratios of the lobe size, D_1/D_2, and monochromatic power, P_1/P_2, resulting from the KDA model, on different values of a few of its basic free parameters assumed for opposite lobes of a fiducial source.

3.4.2 Unlimited external density profile

The original KDA model assumes that radio galaxy evolves in one-medium environment: a halo with decreasing density described by the simplified King's (1972) profile. Gopal-Krishna & Wiita (1987) proposed a more sophisticated model of the jet propagation in which host galaxy is surrounded by two-media environment consisting of an X-ray halo around the parent galaxy with gas density decreasing with radial distance from the galaxy and a hot IGM with constant density. In Section 5, I revised their model introducing contemporary values for the density and temperature of the considered media, as well as compare the revised model dynamical predictions with the age and linear size of several FR II type sources (forming three different samples) resulting from the fit with the KDA model (Kuligowska et al. 2009).

3.4.3 Limitation for the jet activity

KDA model has been also constructed on the assumption that the jets activity of the radio source is continuous, the power-law distribution of injected relativistic particles is constant, and the lobes are powered with constant amount of the new radiating particles. This approach is a good approximation only in the case of young radio sources. It also implies that original KDA model is applicable for young sources with regular spectra only. However, the observations indicate that there are many examples of radio sources (including giant radio galaxies) in which the high-frequency parts of their spectra are steeper than expected for the case of the KDA continuum-injection model, $\alpha_{inj} + 0.5$. This strongly suggests that their activity stopped some time ago. In such the case, the use of "DYNAGE" algorithm results a difficulty in determining a satisfactory age solution for such a source by the best fit of model's free parameters to the observables. The attempt of extending this algorithm to a version applicable for FR II type radio sources with high-frequency spectra steeper than $\alpha_{inj} + 0.5$, and the results of i its application, is given in Section 6 of this Thesis.

PART II

4 Asymmetries of FR II type radio sources predicted with the KDA model

4.1 Lobe's length and total luminosity asymmetries

As numerous observations indicate, the asymmetries of FR II type radio source's lobes (their morphology, size, brightness distribution, total luminosity, spectrum and polarization of radio emission can be meaningful. In this dissertation I consider the lobes' length, D, and monochromatic radio powers, P_ν, only.

In most cases these observed asymmetries cannot be explained by a simple projection effect only - the situation when one of the lobes, that is physically situated closer to the observer (when the jet's axis is significantly inclined to the direction of view) seems to be longer and fainter than the opposite one, according to the differences in the light travel time (Longair & Riley, 1979).

Therefore in this Section, I analyse asymmetries between the lobe's length and radio luminosity predicted by the KDA model. They appear in the model when the values of some of it's free parameters are different for the opposite lobes of a given source. Hereafter these model-predicted asymmetries are described by the ratios D_1/D_2 and $P_{\nu 1}/P_{\nu 2}$ (the latter at the observing frequency of 178 MHz.

Eqs. (4) and (8) in Sections 3.1 and 3.2 indicate the model's parameters from which the lobe's length, $D/2$, and its radio luminosity, P_ν depends. Because the parameters Q_{jet}, ρ_0, a_0 and t are expected to be rather constant for the given source - relative values of $D/2$ will be only dependent on the coefficient c_1 and β parameter, respectively. As it had been mentioned before, coefficient c_1 is a function of the following model's parameters: $\Gamma_{\rm a}$, $\Gamma_{\rm c}$, β and $P_{hc} \simeq 4\,R_t^2$ (cf. Eq. 5). However, one can assume that only values of β and R_t can be different in the opposite lobes. Similarly, relative values of P_ν depend on following parameters: $\Gamma_{\rm B}$, $\Gamma_{\rm c}$, R_t, β, α_{inj} and $r = f(k')$ (cf. Section 3.2), where the last four values only are supposed to be different in the opposite lobes. It is worth noting that R_t value parametrizes the assumed cylindrical geometry of the lobe (cocoon) and is used to calculate its volume, V.

The remaining values of the KDA model's free parameters have been set up as follows: a_0 =10 kpc, $\gamma_{min} = 1$, $\gamma_{max} = 10^7$, $\theta = 90^\circ$, $\Gamma_j = \Gamma_B = \Gamma_c = \Gamma_a = 5/3$.

4.2 Asymmetries resulting from different β exponent

One can expect that β exponent in the power-law density distribution of the external medium surrounding the radio source may have different values in directions of prop-

agation of the opposite jets. It may be due to an inhomogenity of this medium. These differences will cause different values of both: lobe's size and its radio luminosity at a given frequency without referring to any internal asymmetries due to physical processes in the source itself. In order to analyse the above asymmetries, I used a fiducial source with fixed values of $Q_{jet} = 10^{38}$ W, $\rho_0 = 10^{-22}$ kg/m^3, $\alpha_{inj} = 0.51$ (implying $p = 2.02$),$R_t = 3.0$ and $z = 0.5$.

The calculation is performed for two selected source's ages: t =10 and 100 Myr (for D_1/D_2 asymmetry) and for three scenarios in the case of $P_{\nu,1}/P_{\nu,2}$ asymmetry: $t = 10$ Myr and $k' = 0$, $t = 100$ Myr and $k' = 0$, and $t = 100$ Myr and $k' = 10$. Following Kaiser et al. (1997) I used the frequency of 178 MHz. It is assumed that the value of β may vary from 1.0 to 1.9, with the highest difference $\beta_1 - \beta_2 = 0.45$ between the lobes of this source.

Figure (5) presents predicted ratios of D_1/D_2 (plot a) and $P_{\nu,1}/P_{\nu,2}$ (in log scale, plot b), respectively, versus the difference $\beta_1 - \beta_2$. The curves on both plots indicate median values of the above ratios in a set of the model solutions for D_1 and D_2, as well as for $P_{\nu,1}$ and $P_{\nu,2}$ that are dependent on varying values of β providing the same difference of $\beta_1 - \beta_2$. The vertical bars show the standard deviation from the median value.

The diagrams show that the length and luminosity asymmetries increase with age of the source. Besides, the asymmetry in luminosity increases with increasing fraction of non-relativistic (thermal) particles in the radio lobes. Open circles on both diagrams mark the observed ratios of D_1/D_2 and $P_{\nu,1}/P_{\nu,2}$ versus difference of $\beta_1 - \beta_2$ published for the sample of 30 giant-sized radio galaxies by sample of 30 giant-sized radio galaxies by Machalski et al. (2009) and Machalski (2011). In the above papers, $P_{\nu,i}(i = 1, 2)$ are given at a number of observing frequency of 151 MHzas the closest one to the model frequency of 178 MHz. For the sample sources (or lobes) without data at 151 MHz, I use the radio power calculated with flux densities interpolated between neighbouring data points, e.g. between 74 MHz and 325 MHz. The values of β are taken from their "self consistent" solution for the opposite lobes, i.e. from the DYNAGE fit of their radio spectra with a model assuming common values of its free parameters Q_{jet} and ρ_0.

A comparison between the model prediction and the above data for real sources is given in Section 4.6.

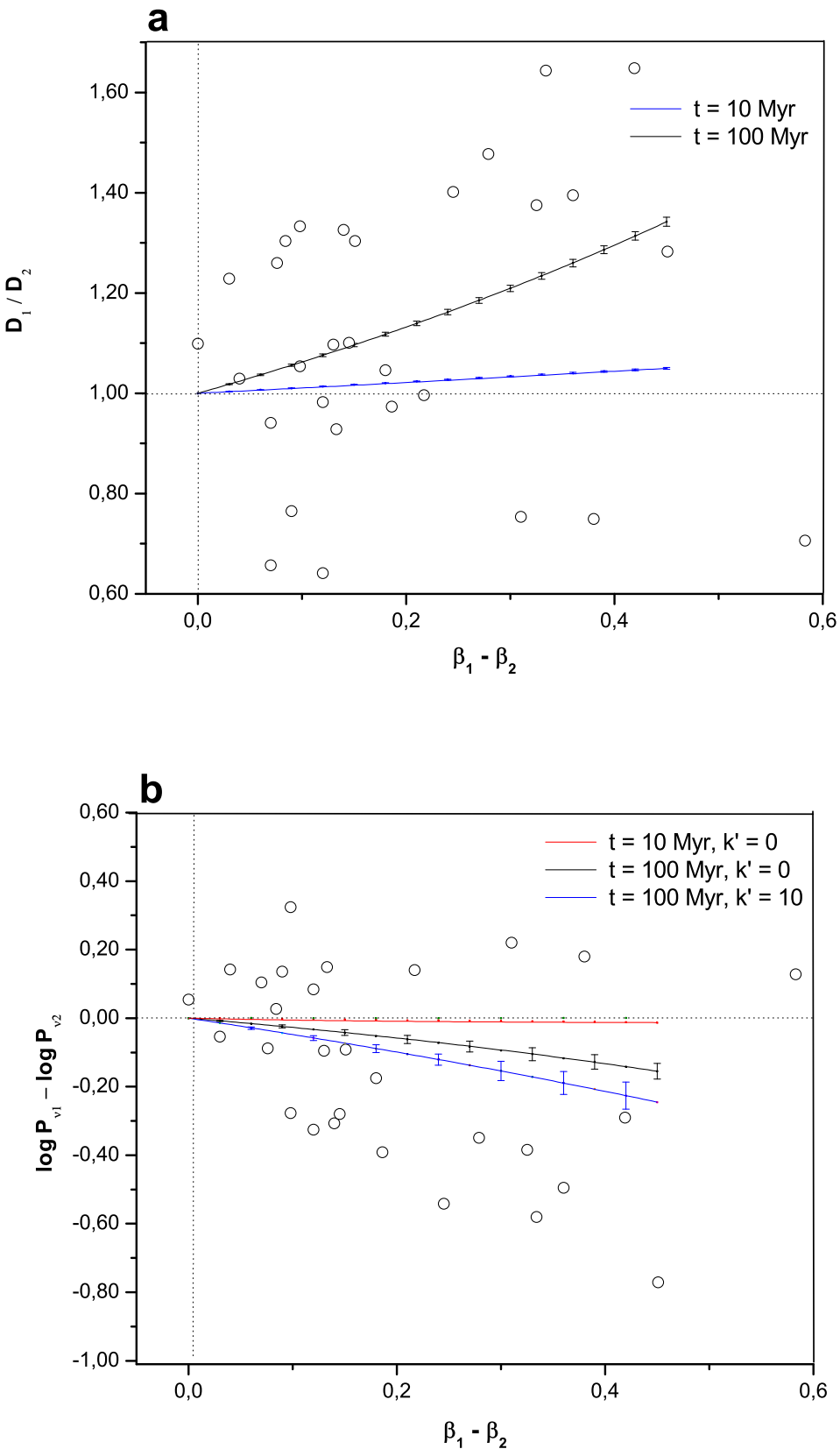

Figure 5: D_1/D_2 (plot **a**) and $logP_{\nu 1} - logP_{\nu 2}$ (plot **b**) vs. varying difference $\beta_1 - \beta_2$ for the fixed value of: α_{inj}, r, R_t and two different values of dynamical ages and k'. The curves indicate medians of the distributions of all individual model solutions for D_1/D_2 and $P_{\nu,1}/P_{\nu,2}$ ratios, calculated as the function of increasing differences between the β parameters in the opposite lobes. The error bars are the standard deviation in these distributions. Circles represent observational data available for 30 giant-sized radio galaxies (see the text above).

4.3 Asymmetries resulting from different axial ratio R_t

Observations shows that the opposite lobes may have significantly different values of R_t. Following Kaiser (2000), it is asummed that the axial and transversal expansion of the radio lobe, governed by the presssure ratio P_{hc}, is related to its axial ratio R_t (cf. Eq. 5). Therefore, observed differences in R_t values in the opposite lobes suggest different ratios of the pressure inside the external environment along and across the jets (different values of P_{hc} at the ends of the opposite jets of the same source), thus different physical conditions in the IGM surrounding the jet's material including its inhomogenity.

Different values of R_t influences both the lobe's length and luminosity, besides different β exponent can cause an observed asymmetry of these lobe's parameters. I assume that R_t varies from 1.5 to 6 with the maximum ratio of 2. Figure (6) shows expected ratios of D_1/D_2 (plot (a) and $P_{\nu,1}/P_{\nu,2}$ (in log scale, plot (b), respectively, versus the ratio of difference of $R_{t,1}/R_{t,2}$ calculated for two different ages of the fiducial sources - $t = 10$ and $t = 100$ Myr. Additionaly, plot b shows the model prediction for $t = 100$ Myr and $k' = 10$. Open circles mark the same observational data as in Section 4.2.

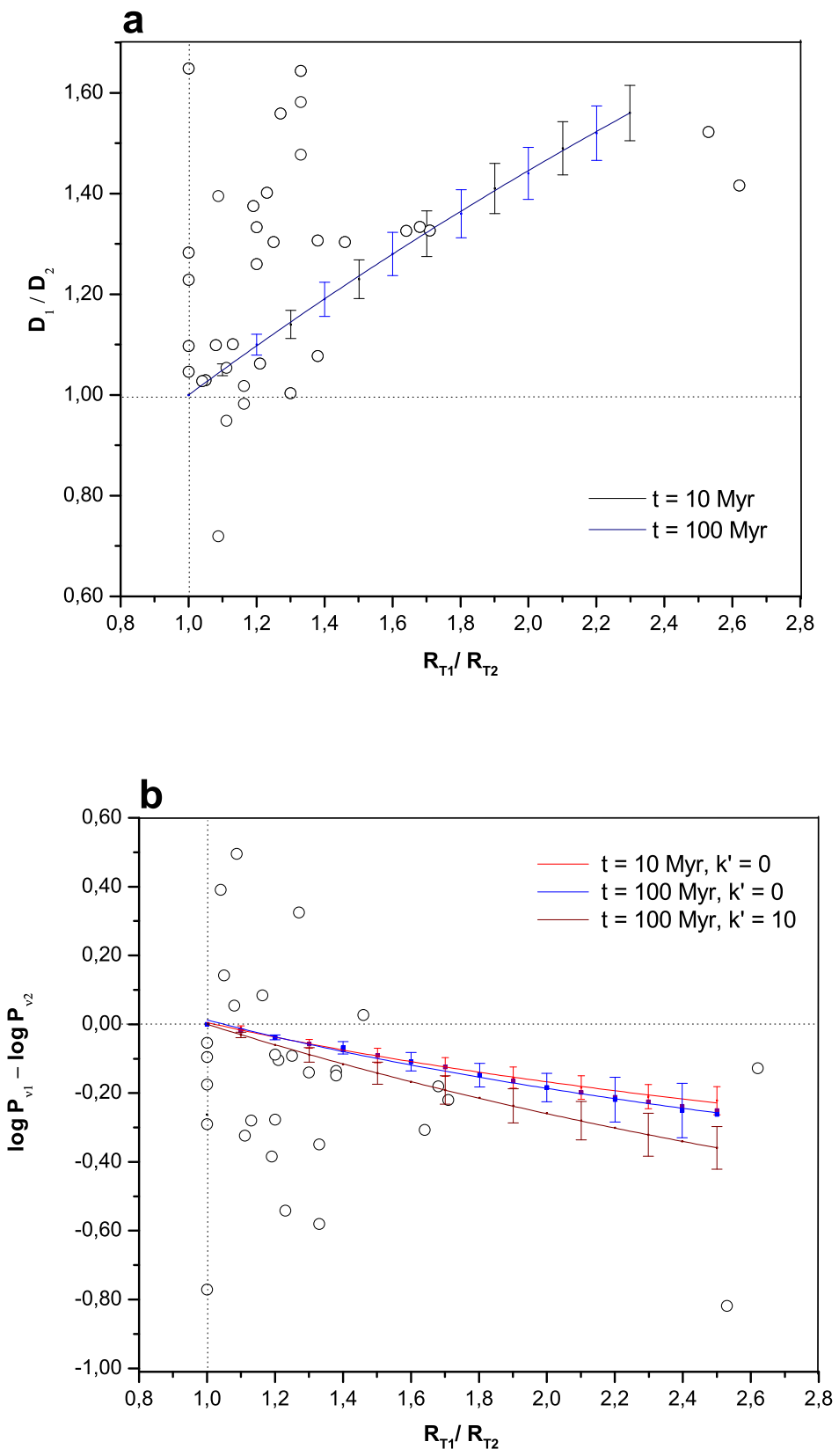

Figure 6: D_1/D_2 (plot **a**) and $logP_{\nu,1} - logP_{\nu,2}$ (plot **b**) vs. varying ratio of R_t parameter for a fixed values of: α_{inj}, r, β and two different values of dynamical ages and k'. The curves indicate medians of the distributions of all individual model solutions (as in Section 4.2.) calculated as the function of increasing differences between the β parameters in the opposite lobes. The error bars are the standard deviation in these distributions. Circles represent observational data available for 30 giant-sized radio galaxies.

4.4 Asymmetries resulting from different α_{inj} parameter

In contrast to the parameters β and R_t, α_{inj} affects only the value of the monochromatic radio power at a given frequency. It does not have any influence for the size of the lobe. Diagrams in this section show how a difference in the "effective" density distribution of relativistic particles across the bow-shock at the head of the opposite jets can result in a diverse synchrotron emission of the relevant lobes and expected symmtetry of $P_{\nu,1}/P_{\nu,2}$. The calculations are performed with identical values of the free parameters of the model as in previous two sections, but changing values of α_{inj} only. It is assumed that the values of α_{inj} may change from 0.5 to 0.8, with the maximum difference $\alpha_{inj,1} - \alpha_{inj,2} = 0.15$ for the opposite lobes of the fiducial source.

Resulting diagram is presented in Figure (7). As previously, the curves show the median values of $P_{\nu,1}/P_{\nu,2}$ in a set of the model solutions of this ratio for a given difference of $\alpha_{inj,1} - \alpha_{inj,2}$. Again, the vertical bars show the standard deviation from these median values. Open circles mark the observational data as in Sections 4.2 and 4.3.

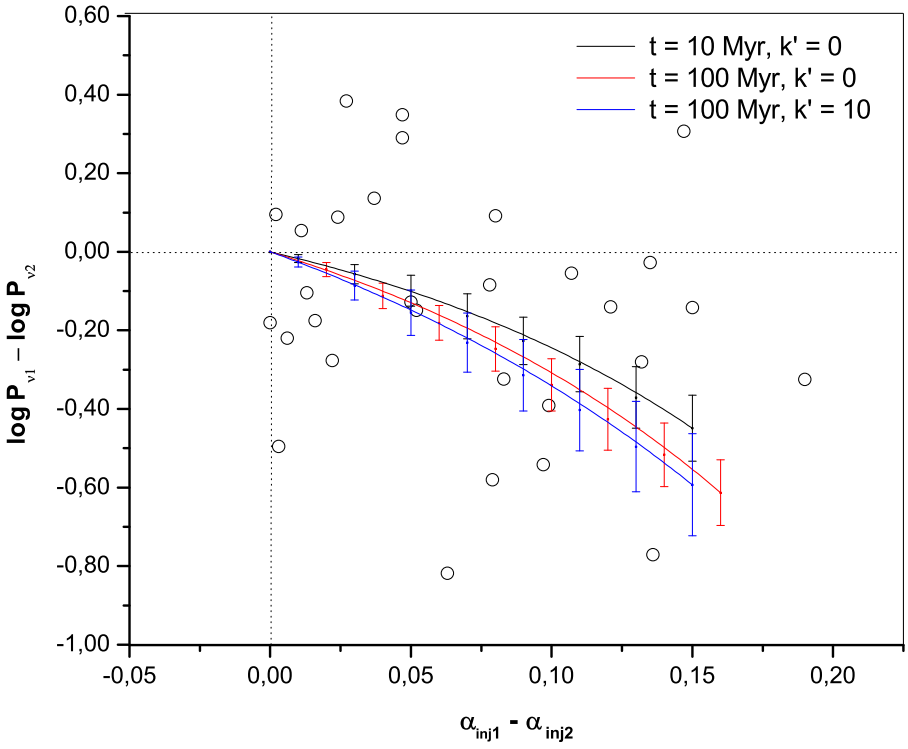

Figure 7: $logP_{\nu,1} - logP_{\nu,2}$ vs. varying difference of $\alpha_{inj,1} - \alpha_{inj,2}$ parameter for a fixed values of: : β, r, R_t and for different values of dynamical ages and k'. The curves indicate medians of the distributions of all individual model solutions (as in Section 4.2.) calculated as the function of increasing differences between the α_{inj} parameters in the opposite lobes. The error bars are the standard deviation in these distributions. Circles represent observational data available for 30 giant-sized radio galaxies.

4.5 Asymmetries resulting from different k' parameter

Different values of k' (the ratio of energy density of the thermal particles to that of the relativistic particles in the lobe's material) also cause an asymmetry in radio luminosity of the opposite lobes. It affects only the value of radio power (Section 3.2) and has no influence into linear size of the lobe. An estimation of the value of k' in real sources is very difficult. For example, Brocksopp et al. (2011), modelling the double–double radio galaxy B1450+333, considered k' values from 0 to 100.

The calculations are performed with identical values of the free parameters of the model as in previous two sections, but changing values of k' only. It is assumed that they may change from 0 (corresponding to the case of no thermal particles in the jet) to 30, with the maximum ratio $k'_1/k'_2 = 15$ for the opposite lobes of the fiducial source. Resulting diagram is presented in Figure (8). The curves show the median values of $P_{\nu,1}/P_{\nu,2}$ in a set of the model solutions of this ratio for a given ratios of k'_1/k'_2.

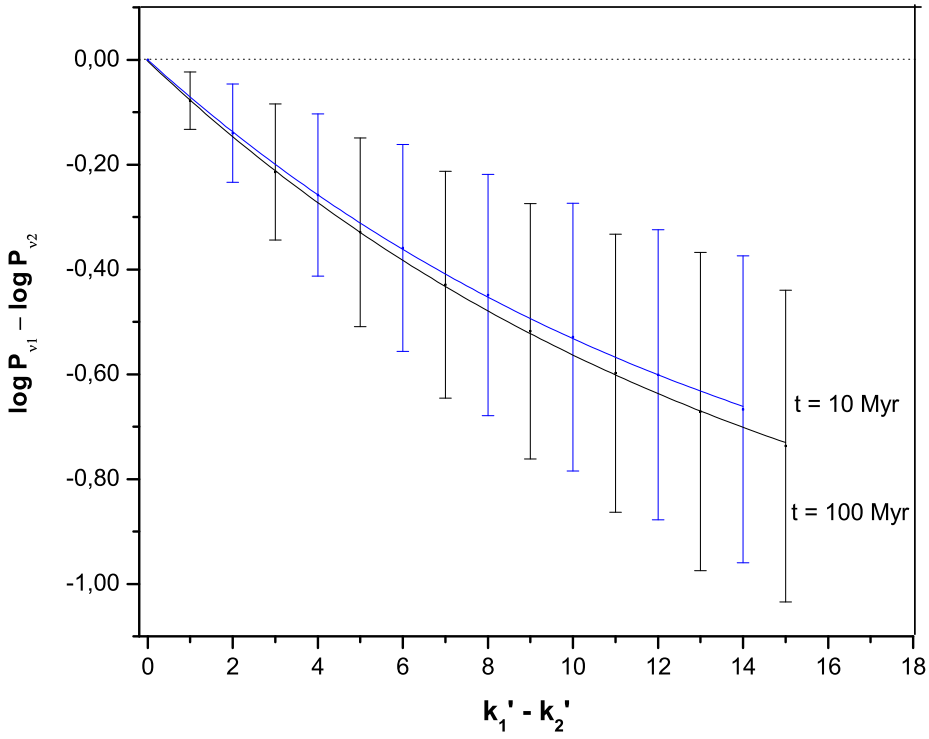

Figure 8: $logP_{\nu,1} - logP_{\nu,2}$ vs. varying ratio of k' parameter for a fixed values of: : β, r, R_t and for two different values of dynamical ages. The curves indicate medians of the distributions of all individual model solutions (as in Section 4.2.) calculated as the function of increasing differences between the k' parameters in the opposite lobes. The error bars are the standard deviation in these distributions.

4.6 Discussion and conclusions

Observed differences in linear sizes and monochromatic radio powers of the opposite lobes of FR II type radio sources are often too large to be explained by the selection effects or projection of the source on the plane of the sky only. The calculations performed in Sections 4.2, 4.3, 4.4 and 4.5 showed that such asymmetries can be easily predicted with the KDA model assuming different physical conditions in these lobes and/or their environment.

These calculations precise the influence of different values of β, R_t and t model parameters on the lobe's length asymmetry D_1/D_2 (as expected from Eg. 4), as well as confirm a supposition that a significant influence on the luminosity asymmetry, $P_{\nu 1}/P_{\nu 2}$, have the model parameters β, R_t, α_{inj}, k' and t. Although different age of the opposite lobes is rather not admissible, this is worth emphasizing that the influence of absolute age value of the fiducial source on the asymmetries considered here is meaningful.

4.6.1 Model predictions for the asymmetries

Asymmetry of lobe's length depends on the values of model parameters β and R_t. This influence is stronger in the case of R_t parameter determining the pressure ratios in the lobe, P_{hc} (cf. Figure (6a)). In turn, Figure (5a) presents very strong dependency of the source's age on the resulting D_1/D_2 asymmetry. These asymmetries increase with the age of a given source.

Asymmetries of lobe's radio brightness may result from different values number of the model parameters. In Sections 4.2, 4.3, 4.4 and 4.5 I analyzed the dependence of such asymmetry on the values of parameters β, α_{inj}, R_t and k'. A variation of the β parameter gives relatively low $P_{\nu,1}/P_{\nu,2}$ asymmetries slowly increasing with the increasing age of the source, while for parameters α_{inj}, R_t and k' the predicted degree of the asymmetry is nearly the same and highly dependent on the source's age.

As concerns the $P_{\nu,1}/P_{\nu,2}$ asymmetry, one can compare its dependence on the parameters β, α_{inj} and R_t with that resulting from different values of k'. It is almost equally strong as the impact of the change of the source's age on shape of the model curves. At the same time it is difficult to clearly determine which one of these parameter influences the greatest asymmetry. In the case of the parameters β and α_{inj} it is the age, but in turn for R_t it is a change of the parameter k'.

It is clearly seen that while in the case of asymmetry in the length of the lobes the number of factors that may cause them is relatively small, whereas the asymmetry of their radio brightness may be caused by different values of several model parameters and thus it is not easy to determine which one of them has a decisive influence in this case.

4.6.2 Model prediction in comparison with observational data

Asymmetries of lobe's length and brightness predicted by the model are confronted with the observed asymmetries in the small and heterogeneous (only available in the literature) sample of 30 "giant" radio galaxies (Machalski et al. 2009, Machalski 2011). In both of these publications the observed asymmetries D_1/D_2 and $P_{\nu,1}/P_{\nu,2}$ are reproduced by varying the values of only two model parameters, namely β and α_{inj}. In particular, different values of β in the opposite lobes (where usually different values of R_t are known from observations) are used to explain the observed asymmetry in the length of the lobes. In the next step, the observed asymmetry in the brightness of the opposite lobes of radio galaxies from those samples is reproduced by a variation of the α_{inj} parameter in these lobes. In this way the observed ratio of $P_{\nu,1}/P_{\nu,2}$ is described by a diversity of not the only one, but three parameters of the model, R_t, β and α_{inj}. Thus these observations confirm the conclusions from the previous paragraph that a given asymmetry of lobe's length and brightness cannot be described by different values of a single model parameter, however it can be provided by a combination of several different values of its free parameters only. This is in accordance with the physics of the FR II type radio source, because the radio brightness at a given frequency depends on energy distribution of relativistic particles, strength and orientation of the magnetic field, and the volume of the source (or its lobes), thus on much larger number of the model's free parameters than the length of the lobes. It is also evident from the example of the observational data of the sample sources. The diagrams illustrating $P_{\nu,1}/P_{\nu,2}$ asymmetry show much more noticeable dispersion of the sample sources around the model curves than the diagrams confronting the observed D_1/D_2 asymmetry with the model predictions.

Only the small fraction of observed asymmetries corresponds to the prediction of the model presented on Figures (5), (6) and (7). It is worth noting that these asymmetries in real radio sources mainly correspond to the model curves calculated for source's age of 100 Myr and for different values of k'. It is understandable because the samples comprise sources with very large linear sizes and ages of about $\simeq 100$ Myr, not including, however, small and relatively young sources.

In the case of the diagrams presenting the $P_{\nu,1}/P_{\nu,2}$ asymmetry one can notice strong deviations of the notable part of the observed sources from the model predictions. These sources are not even close to the curves calculated for the source age of 100 Myr (for both values of k'), though their fitted dynamical ages calculated for the sources have typical values of this range and are not exceeding the value of 250 Myr.

The above conclusions are not comprehensive in the sense that the sample is not representative for the entire FR II type sources population. As it was already mentioned, the selection effect causes that it consist of large radio galaxies only. Therefore, a future research should focus on the comparison of model predictions for the asymmetry with larger and more diverse samples of FR II radio sources.

5 The observational constraint for the model of the radio-jets propagation through the X-ray halo–IGM interface (Kuligowska et al. 2009)

Kuligowska, Jamrozy, Kozieł–Wierzbowska & Machalski, 2009, AcA, 59, 431

Extended large-sized radio sources are not easy to recognize because of their relatively low radio brightness and a difficulty to detect eventual bridge connecting brighter parts (lobes) of a common radio structure. Several observational efforts show that most of known GRGs lie at low redshifts of z<0.25. For a long time this caused a presumption that such extragalactic double radio sources, especially those of FRII-type, did not exist at redshifts higher than about one because of the expected strong evolution of a uniform IGM, $\rho_{\rm IGM} \propto (1+z)^3$, confining the lobes of sources (e.g. Kapahi 1989). The situation changed over 10 years ago when Cotter, Rawlings & Saunders (1996) and Cotter (1998) presented an unbiased sample of giant radio sources selected from the 7C survey (McGilchrist et al. 1990). Their sample comprised 12 large-size sources with 0.3<z<0.9. The list of known GRGs with z>0.5 and D>1 Mpc is very short. The undertaken search for such GRGs on the southern sky hemisphere with the 11m SALT telescope during the Performance Verification (P–V) phase has resulted in the detection of 21 GRGs with the projected linear size greater than 1 Mpc. However, one can found that their redshifts do not exceed the value of 0.4 and the energy density in only two of them is less than 10^{-14}Jm^{-3}. One of them, J1420-0545, is the largest known GRG in the Universe (cf. Machalski et al. 2008).

The dynamical evolution of a FRII radio source strongly depends on characteristics of the ambient medium. Gopal-Krishna & Wiita (1987) proposed the two-medium model consisting of an X-ray halo around the parent galaxy with gas density decreasing with radial distance from the galaxy and a much hotter intergalactic medium (IGM) with constant density. These two media were conceived to be pressure-matched at their interface. Their model allowed to predict limiting (maxima) values for the source's age and linear size depending on the environment conditions, the jet power, and the cosmic epoch characterized by the source's redshift. However, our recent detections of very large-sized radio sources with z>1 and exceeding the limits predicted by their model (hereafter referred to as G-KW model), suggests that some of its free parameters should be modified.

In this Section an observational constraint for the G-KW model is analyzed. For this purpose, an effort to determine the highest sizes and dynamical ages of FRII-type radio sources at redshifts 1<z<2 is undertaken. The original G-KW model is briefly described and modified adopting modern (contemporary) values for thermodynamic temperature and gas density of the two media. Then, the predicted relations between

the sources' physical size and the age, as well as the expansion speed of the radio lobes' head and the age are calculated.

The observational data used to constrain the two-medium model are presented. The small sample of the most distant giant-sized radio sources is revised and supplemented with two other limited samples of FRII-type sources comprising: (i) sources larger than 400 kpc within the redshift range 1<z<2, most of them found in this paper, and (ii) selected 3CRR sources in majority smaller than 400 kpc at z>0.5 forming a comparison sample of "normal"-sized radio sources. Physical parameters of the sample sources: the dynamical age, the jet power, the central radio-core density and the IGM density, and others, are derived using the "DYNAGE" algorithm (Machalski et al. 2007a). The application of this algorithm to the sample sources and the resulting values of the source's parameters are described in Section 5.2. A comparison of the model predictions with the observational data is presented and discussed in Section 5.3.

5.1 The base of the revised G-KW model

In the G-KW model, the jet propagates into a two-component medium comprised of:

– the gaseous halo with a power-law density profile $\rho_{\rm h}(d) = \rho_0\,[1 + (d/a_0)^2]^{-\delta}$ bound to the parent optical galaxy, where ρ_0 and a_0 are the density and the radius of the central radio core, respectively, and δ=5/6. This distribution is assumed to be invariant with redshift. It is also assumed that this halo has nearly uniform electron temperature $(kT)_{\rm h}$[keV] (medium 1), and

– the surrounding hotter IGM of uniform density, $\rho_{\rm IGM}$, with the temperature $(kT)_{\rm IGM}(1+z)^2$[keV] (medium 2).

Similarily to Gopal-Krishna & Wiita (1987) it is necessery to assume characteristic values for the density and temperature of the considered media. The values adopted hereafter for the two components are based on the following data:

(1) The radio core radius, a_0=3 kpc is based on the fitted X-ray surface-brightness profile of nine nearby, low-luminosity radio galaxies recently observed by Croston et al. (2008). This value of the radius is derived from the observed angular radius of about 10 arcsec.

(2) The halos' gas temperature have been determined in a number of papers. A uniform temperature $(kT)_{\rm h}$=0.7 keV was measured for a few nearby, X-ray luminous elliptical galaxies with the *Chandra Observatory* by Allen et al. (2006). Using *XXM-Newton* and *Chandra* observations, the values from 1 to 5 keV with a median of about 2.1 keV was found by Belsole et al. (2007) for the X-ray clusters surrounding 20 luminous 3CRR radio sources. For the low-luminosity radio galaxies analysed by Croston et al. (2008), a median of the fitted temperatures is about 1.4 keV. Taking the above data into account one can estimate: $(kT)_{\rm h}$=1.4 keV.

(3) The halos'gas (proton) density of $(1 - 2)\times10^4$ m^{-3} is fitted to X-ray counts by Belsole et al. (2007).

The interface between the X-ray halo and IGM is determined balancing the IGM pressure against the pressure distribution in the halo. A non-relativistic gas in thermal equilibrium that has an electron density $n_{\rm e}$[m^{-3}] and temperature $(kT)_{\rm e}$[keV] will have an electron pressure $p_{\rm e}$=$n_{\rm e}\,(kT)_{\rm e}$[Pa]. Expressing electron density by the mass density, ρ=$n\,\mu\,m_{\rm H}$, this balance will have place at the halo's radius $R_{\rm h}$ calculated from

$$\frac{\rho_0}{\mu_{\rm h} m_{\rm H}}\left[1+(R_{\rm h}/a_0)^2\right]^{-\delta}(kT)_{\rm h} = \frac{\rho_{\rm IGM}}{\mu_{\rm IGM} m_{\rm H}}(kT)_{\rm IGM}, \qquad (9)$$

where μ and $m_{\rm H}$ are the mean molecular weight and the mass of hydrogen atom, respectively. $\mu_{\rm h}$ is assumed to $\mu_{\rm h}$=0.5 and $\mu_{\rm IGM}$=1.4. Besides, for the halo (medium 1) n_p=1.5 $\times$ 10^4 m^{-3} is adopted (i.e. a mean proton density of the values given by Belsole et al. (2007), which corresponds to ρ_0=$10^{-22.6}$ kg m^{-3}, and the temperature $(kT)_{\rm h}$=1.4 keV). For the IGM density 50% of the cosmic matter density is taken, i.e. $\rho_{\rm IGM}$=$0.5\Omega_{\rm m}h^2\rho_{\rm clos}$= $0.5\times0.27\times0.71^2\times(3\,H_0^2)/(4\pi\,G)$, which gives $\rho_{\rm IGM}$= $10^{-26.9}$ kg m^{-3}. For the IGM temperature the values of $(kT)_{\rm IGM}$=25 keV is adopted. Substituting the above values into Eq. (9) one can find $R_{\rm h}$=642 kpc. This radius of X-ray halo is compatible with the radii determined by Cassano et al. (2007) for 15 Abell cluster radio haloes with the mean of $\sim$ 560$\pm$170 kpc. This is worth to notice that thit radius of 642 kpc is much larger than 171 kpc used by Gopal-Krishna & Wiita. In an expanding and uniform IGM this radius should evolve as $R_{\rm h}(z) = 642(1+z)^{-5/(2\delta)}$ kpc, i.e. $642(1+z)^{-3}$ kpc for δ=5/6.

Figure (9) (a), (b), (c) present the basic characteristics of the two-media model: the mass density $r(d)$, the electron temperature $kT(d)$, and the resulting electron gas pressure $p(d)$, as functions of the distance from the host galaxy (compact radio core), respectively. Note that the balance $p_h(R_h) = p_{IGM}$ at $d = R_h$ corresponds to a rapid transition between $r(R_h)$ and r_{IGM}, as well as between $kT(R_h)$ and kT_{IGM}, and causes an unphysical effect shown in Section 5.6.1. The dashed curves in Figure (9) (a) and (b) indicate desired smooth transitions between the relevant parameters which would introduce a better physical scenario into the model.

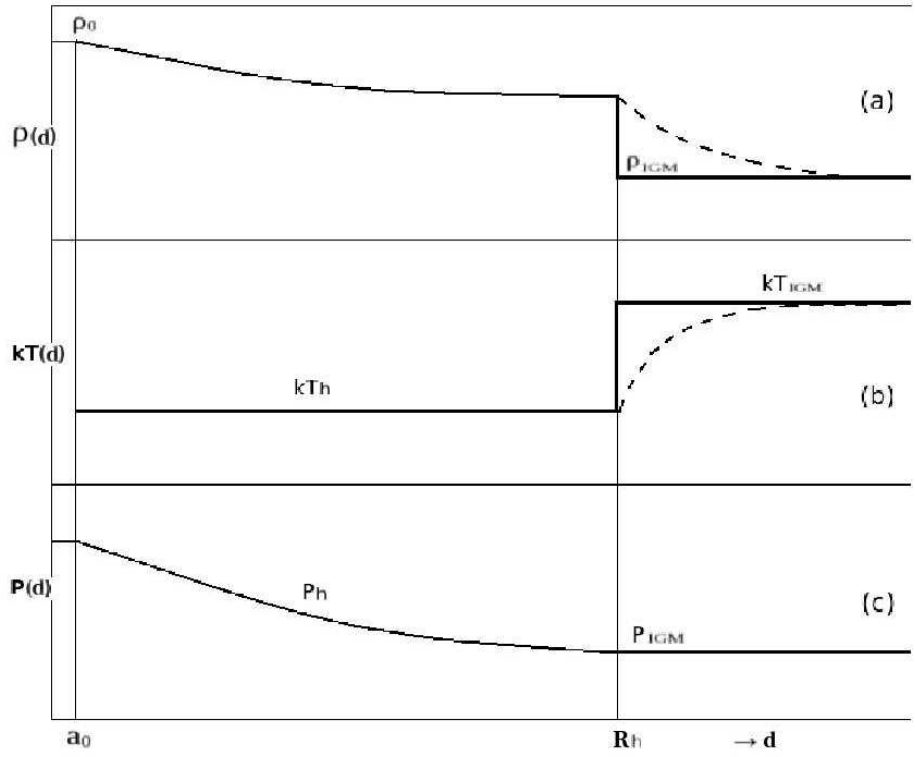

Figure 9: Properties of the two-media environment surrounding the center of radio galaxy.

5.2 Predictions of the model

For $d \leq R_{\rm h}$ it is assumed that the jet propagate (through the medium 1) with a constant opening angle, θ. Under this condition, the ram pressure balance results in the following dependences for the jet length (the radio lobe size, D) on time (the lobe's age, t) and the jet's head expansion velocity, v_h, on D or t:

$$D(t) = [(2-\delta)\, A\, t]^{\frac{1}{2-\delta}}\,, \tag{10}$$

$$v_h(D) = A\, D^{(\delta-1)}, \tag{11}$$

$$v_h(t) = \left[(2-\delta)\, A^{\frac{1}{\delta-1}} t\right]^{\frac{\delta-1}{2-\delta}}\,, \tag{12}$$

where

$$A \equiv \left(\frac{4\, c_1 Q_{\rm jet}}{\pi\theta^2 c\, \rho_0 a_0^{2\delta}}\right)^{\frac{1}{2}}. \tag{13}$$

Here c_1 is a constant with a value between 1.5 and 3.8 depending on the source's (lobe's) geometry described by its axial ratio $R_{\rm t}$ (Kaiser & Alexander 1997), while $c \approx v_{\rm jet}$ is the speed of light. The jet's opening angle is also described by $R_{\rm t}$, $\theta^2 = c_2/(4\,R_{\rm t})$, where c_2 is a constant with a value between 3.6 to 4.1 depending on specific heats for the material in the jet and the lobe (cocoon), (Eq. (17) in Kaiser & Alexander 1997). At $d = R_{\rm h}(z)$ the jet enters the hotter IGM (medium 2) at least an order of magnitude less dense but pressure-matched, as shown in Figure (9). In order to analyze the jet's propagation over this regime, Gopal-Krishna & Wiita have considered two likely extreme scenarios for the lobe's expansion:

— *Scenario A* where the jet opening angle, θ, is conserved. Due to a rapid decrease of the ambient density at the interface, $\rho_{\rm IGM} \ll \rho_{\rm h}(R_{\rm h})$, a sufficient ram-pressure will be provided only if the jet's head velocity, $v_{\rm hs}$, increases abruptly at $d{=}R_{\rm h}$ and then gradually approaches the $v_h \propto d^{-1}$ law expected for a constant density medium. In this scenario:

$$D(t) = \left\{ 2 \left(K(z) + a_0^{\delta}\, A \left[\frac{\rho_0}{\rho_{\rm IGM}(1+z)^3} \right]^{1/2} t \right) \right\}^{1/2} \qquad \text{and} \tag{14}$$

$$v_h(t) = a_0^{\delta}\, A \left[\frac{\rho_0}{\rho_{\rm IGM}(1+z)^3} \right]^{1/2} / D(t), \tag{15}$$

where

$$K(z) = \frac{1}{2} R_{\rm h}^2(z) - R_{\rm h}^{(2-\delta)}(z) \frac{a_0^{\delta}}{2-\delta} \left[\frac{\rho_0}{\rho_{\rm IGM}(1+z)^3} \right]^{1/2} \tag{16}$$

is a redshift-dependent constant providing that the time corresponding to $D{=}R_{\rm h}$ in Eqs. (10) and (14) is the same.

— *Scenario B* where the jet's head velocity across the interface remains continuous and therefore matched to the value given by Eq. (11) for $D{=}R_{\rm h}$. This can be achieved only with an abrupt flaring of the jet's opening angle. Under this condition the model predicts:

$$D(t) = \left\{ 2 \left(A\, R_{\rm h}^{\delta}(z)\, t - R_{\rm h}^2(z) \frac{\delta}{2(2-\delta)} \right) \right\}^{1/2} \qquad \text{and,} \tag{17}$$

$$v_h(t) = A\, R_{\rm h}^{\delta}(z) / D(t). \tag{18}$$

The sound speed in the IGM is given by

$$s_{\rm IGM}(z) = \left[\frac{\Gamma(kT)_{\rm IGM}}{\mu\, m_{\rm H}}\right]^{1/2} (1+z). \qquad (19)$$

Given the values Γ=5/3, μ=1.4 and $(kT)_{\rm IGM}$=25 keV, the sound speed limiting the source (lobe) axial expansion velocity is $s_{\rm IGM} \approx 0.0056\, c$ at $z \approx 0$, and $s_{\rm IGM} \approx 0.0169\, c$ at $z \approx 2$. The time dependences of the source size $D(t)$ calculated from Eqs. (10), (14) and (17), as well as of the axial expansion velocity $v(t)$ calculated from Eqs. (12), (15) and (18) for the three cases: $Q_{\rm jet}$=$10^{37.5}$ W and z=0.5, $Q_{\rm jet}$=$10^{38.5}$ W and z=1.0, and $Q_{\rm jet}$=$10^{39.5}$ W and z=2.0, are shown in Figures (10) and (11), respectively.

To compare these predictions with the observations, three different samples of FRII-type radio sources have been selected.

5.3 Selection of the samples

5.3.1 Sample 1 (GRG sample)

The revised sample of FRII-type radio sources with 0.5<z<1 and the projected linear size larger 1 Mpc, compiled from the literature, is presented in Table (1). Columns (1)–(5) are selfexplanatory. Entries in columns (6)–(10) are the data used to determine the age and other physical parameters of the sample sources. Some necessary references are given in the Notes.

5.3.2 Sample 2 (Distant-source sample)

The second sample of FRII-type sources larger than 400 kpc and having z>1 consists of a few sources known from the literature and the sources found in this paper. The latter part of this sample results from the dedicated research project attempting to determine how large linear size FRII-type radio sources can achieve at redshifts 1<z<2. This part was preselected using the modern Sloan Digital Sky Survey (hereafter referred to as SDSS: Adelman-McCarthy et al. 2007) as the finding survey. The optical objects extracted from the SDSS, fulfilling the above redshift criterion and classified either as a galaxy (G) or a QSO (Q), were then cross-correlated with the radio 1.4-GHz sky survey FIRST (Becker, White & Helfand 1995). In the second step, all optical objects strictly coinciding with a compact radio source, i.e. with a potential radio core, were subject to the further selection. In the third step, we have checked whether the (core) component is surrounded by a pair of nearly symmetric, possibly extended radio structures (lobes) with an angular separation providing a projected linear size $D \gtrsim 400$ kpc. All candidates were verified by an inspection of their images (if exist) in other available radio surveys,

namely the 1.4-GHz NVSS (Condon et al. 1998), 325-MHz WENSS (Rengelink et al. 1997), and 74-MHz VLSS (Cohen et al. 2007). The assumed cosmology predicts that a maximum of the linear size/angular size quotient at z>1 is ∼8.55 kpc/" which, in turn, implies that a source larger than 400 kpc should have $\theta \gtrsim 47$". All radio sources selected this way from the SDSS are classified as QSO. The final sample is presented in Table (2). All columns give the similar data as those in Table (1). The radio images of exemplary sample sources, made using combined UV-data from the NVSS and FIRST surveys, are shown in Figures (13) - (15).

However, in order to use this sample to constrain the analytical G-KW model, besides the redshift and linear size of the member sources, one has to determine their age and other physical parameters which is not attainable without an information about the radio spectrum within wide-enough spectral range and providing the radio luminosity of a given source at least three or more different observing frequencies. For the large part of the Sample 2 it was possible to use flux densities from the radio catalogues: VLSS (74 MHz), 6C and 7C (151 MHz; Hales et al. 1988 and Riley et al. 1999, respectively), WENSS (325 MHz), B3 (408 MHz; Vigotti et al. 1999, NVSS (1.4 GHz) and GB6 (4.85 MHz; Gregory et al. 1996). It is worth to notice that three QSOs in Sample 2 have the (projected) linear size larger than 1 Mpc.

5.3.3 Sample 3 (3CRR sample)

The third observational sample comprises 3CRR FRII-type sources with z>0.5 but size smaller than 400 kpc (except of 3C265 and 3C292 which are larger). For the reason to have homogeneous and complete data for radio spectra of the sample sources necessary for estimation of their dynamical age and corresponding physical parameters (jet power, mean expansion velocity, etc.), this sample is limited to sources with the galactic latitude of $\delta_{\rm II} > 30^o$ where good spectral data are available from the low-frequency radio surveys: VLSS, 6C, 7C and WENSS. The sample sources are listed in Table (3).

Table 1: The sample of FRII-type sources with 0.5<z<1 and D>1 Mpc. The radio luminosities are given in units of $\mathrm{WHz^{-1}s^{-1}}$. The low-frequency luminosity, P_{lf}, is determined either at 74 MHz (marked *a*) or 151 MHz (*b*) or 325 MHz (*c*).

IAU name	Survey	z	Id.	D [kpc]	$R_{\rm t}$	θ [^{o}]	log P_{lf}	log P_{1400}	log P_{4850}	Notes
(1)	(2)	(3)	(4)	(5)	(6)	(7)	(8)	(9)	(10)	(11)
J0037+0027		0.5908	G	1976	5.0	90	26.103^a	25.149	24.606	(4,5)
B0654+482	7C	0.776	G	1002	4.0	90	26.120^b	25.262	24.733	(1)
J0750+656		0.747	Q	1606	4.0	90	26.189^a	25.255	24.715	(3)
B0821+695	8C	0.538	G	2580	3.0	90	26.142^b	25.106	24.525	(2)
B0854+399	B2	0.528	G	1014	2.7	70	26.385^b	25.627	25.098	
B1058+368	7C	0.750	G	1100	4.2	90	26.192^b	25.412	24.809	(1)
J1130−1320	PKS	0.6337	Q	2033	3.8	90	27.275^a	26.198	25.613	(4,5)
B1602+376	7C	0.814	G	1376	2.6	90	26.292^b	25.486	24.936	(1)
B1636+418	7C	0.867	G	1004	3.9	90	26.006^b	25.273	24.701	(1)
B1834+620	WNB	0.5194	G	1384	4.1	90	26.361^b	25.555	25.067	(6)
J1951+706		0.550	G	1300	4.5	90	25.974^a	24.894	24.448	(3)
J2234−0224		0.55	Q	1266	4.5	90	—	24.840	—	(4,5)

Notes: (1)–Cotter et al. (1996); (2)–Lara et al. (2000); (3)–Lara et al. (2001); (4)–Koziel-Wierzbowska (2008); (5)–Machalski et al. (2007b); (6)– Schoenmakers et al. (2000)

Table 2: The sample of FRII-type sources with 1<z<2 and D>400 kpc. The radio luminosities are in units of $WHz^{-1}s^{-1}$. The low-frequency luminosity marked *a*, *b*, *c* – as in Table (1). The values in parenthesis are approximated because of less certain subtraction of the core contribution. The sources identified in this paper are marked with the asterix following their name.

IAU name	Survey	z	Id.	D [kpc]	R_t	θ [^{o}]	log P_{lf}	log P_{1400}	log P_{4850}	Notes
(1)	(2)	(3)	(4)	(5)	(6)	(7)	(8)	(9)	(10)	(11)
J0245+0108 *		1.537	Q	456	3.6	70	27.822^a	26.658	26.087	
J0809+2015 *		1.129	Q	465	3.1	70	—	(25.61)	(25.02)	(1)
J0809+2912 *		1.481	Q	1120	3.0	70	27.234^a	26.476	26.015	
J0812+3031 *		1.312	Q	1240	3.0	70	25.504^c	25.032	—	(2)
J0819+0549 *		1.701	Q	985	3.0	70	—	25.578	—	(1,2)
J0839+2928 *		1.136	Q	417	2.3	45	26.813^a	25.882	25.364	
J0842+2147 *		1.182	Q	1080	3.0	70	—	25.425	—	(1,2)
J0857+0906 *		1.688	Q	506	4.5	70	27.357^a	26.276	25.763	
J0902+5707 *		1.595	Q	862	4.0	70	25.905^c	25.325	—	(2)
J0906+0832 *		1.617	Q	682	3.6	70	—	25.750	—	(1,2)
J0947+5154 *		1.063	Q	478	3.9	70	27.002^a	25.767	25.157	
J0952+0628 *		1.362	Q	551	4.3	70	27.081^a	25.988	25.508	
B1011+365	6C	1.042	G	416	3.5	70	26.902^b	26.204	25.680	
J1030+5310 *		1.197	Q	835	3.0	90	26.336^b	25.481	24.945	
J1039+0714 *		1.536	Q	501	3.0	70	—	25.450	—	(1,2)
B1108+359	3C252	1.105	G	493	3.0	70	28.164^a	26.921	26.282	
B1109+437	B3	1.664	Q	488	4.5	70	28.092^a	27.357	26.812	
J1130+3628 *		1.072	Q	422	3.0	50	25.992^b	25.277	(24.67)	
J1207−0244 *		1.100	Q	444	3.0	50	26.590^a	25.407	—	(2)
J1434−0123 *		1.020	Q	490	3.0	50	26.894^a	25.763	—	(2)
J1550+3652 *		2.061	Q	675	3.0	70	26.771^b	26.041	25.527	
J1706+3214 *		1.070	Q	438	3.0	50	26.757^a	25.682	25.150	
B1723+510	3C356	1.079	G	614	4.0	70	27.875^b	26.916	26.304	
J2345−0936 *		1.275	Q	513	3.2	90	27.318^a	26.266	(25.62)	
B2352+796	3C469.1	1.336	G	626	4.4	70	28.269^a	27.167	26.628	

Notes: (1)–off the 7C and WENSS surveys; (2)–off the 4.85-GHz GB6 or PMN6 (Griffith et al. 1995) surveys or below their flux density limit

Table 3: 3CRR sample of FRII-type sources with z>0.5 and $\delta > 30^o$

Source	z	Id.	D	R_t	θ	log	log	log	Notes
			[kpc]		[^{o}]	P_{lf}	P_{1400}	P_{4850}	
(1)	(2)	(3)	(4)	(5)	(6)	(7)	(8)	(9)	(10)
3C6.1	0.8404	G	199	2.7	70	27.706^a	26.938	26.494	(1)
3C13	1.351	G	237	3.0	70	28.261^a	27.259	26.682	(1)
3C22	0.937	G	190	3.0	70	27.780^a	26.920	26.403	(1)
3C34	0.689	G	341	4.3	90	27.656^a	26.474	25.815	(1)
3C41	0.794	G	175	2.4	70	27.404^b	26.851	26.491	(1)
3C54	0.8284	G	401	3.9	70	27.670^a	26.644	26.168	
3C65	1.174	G	142	2.3	70	28.077^b	27.296	26.761	(1)
3C68.1	1.238	Q	386	2.4	50	27.967^b	27.239	26.767	
3C68.2	1.575	G	191	2.3	70	28.290^b	27.259	26.548	
3C169.1	0.633	G	315	2.7	70	27.287^a	26.214	25.700	(1)
3C184	0.99	G	35		70	27.832^a	27.017	26.514	(1)
3C196	0.871	Q	39	1.5	30	28.522^a	27.605	27.117	(1)
3C204	1.112	Q	257	3.4	70	28.032^a	26.857	26.267	(1)
3C205	1.534	Q	134	4.2	70	28.329^a	27.469	26.903	(1)
3C217	0.898	G	86	4.0	70	27.796^a	26.853	26.318	(1)
3C220.1	0.610	G	86	4.0	70	27.541^a	26.469	25.875	(1)
3C220.3	0.685	G	52	3.0	70	27.425^b	26.710	26.045	
3C239	1.786	G	96	1.4	70	28.483^b	27.541	26.914	
3C247	0.749	G	95	2.4	70	27.350^b	26.746	26.284	
3C254	0.734	Q	96	2.0	50	27.974^a	26.791	26.198	(1)
3C263	0.6563	Q	307	2.7	50	27.616^a	26.634	26.182	(1)
3C263.1	0.824	G	41	1.7	70	27.696^b	26.911	26.369	
3C265	0.8108	G	587	3.9	70	27.775^b	26.859	26.310	
3C266	1.275	G	36	2.4	70	27.981^b	27.137	26.509	
3C268.4	1.400	Q	83	2.8	50	28.123^a	27.273	26.774	(1)
3C270.1	1.519	Q	102	1.3	50	28.314^a	27.478	26.917	
3C272	0.944	G	461	3.3	70	27.417^b	26.708	26.135	
3C280	0.996	G	113	1.5	70	27.990^b	27.288	26.829	
3C280.1	1.659	Q	169	4.0	70	28.267^a	27.343	26.771	(1)
3C289	0.967	G	81	1.3	70	27.686^b	26.966	26.430	
3C292	0.71	G	960	4.2	90	27.406^b	26.547	26.075	
3C294	1.779	G	135	1.9	70	28.413^b	27.431	26.840	
3C322	1.681	G	283	2.5	70	28.171^b	27.485	26.954	
3C324	1.207	G	85	1.8	70	27.999^b	27.257	26.712	
3C325	0.860	G	122	2.2	70	27.657^b	27.011	26.481	
3C330	0.549	G	395	5.4	90	27.432^b	26.771	26.334	
3C337	0.635	G	295	2.5	70	27.522^a	26.599	26.125	(1)
3C352	0.8057	G	75	2.3	70	27.695^a	26.699	26.108	(1)
3C427.1	0.572	G	153	2.2	70	27.437^b	26.634	26.071	
3C437	1.48	G	316	3.9	70	28.086^b	27.481	27.030	
3C441	0.707	G	236	2.5	70	27.395^b	26.636	26.166	
3C470	1.653	G	205	4.0	70	28.269^a	27.444	26.952	(1)

5.4 Ageing analysis of the samples' sources

The dynamical age analysis is performed using the DYNAGE algorithm. It is based on the analytical KDA model (cf. Section 3.2). The original KDA model, assuming values for a number of free parameters of the model, allows to predict a time evolution of the source's length, D, and radio luminosity, P_ν, at a given observing frequency. The DYNAGE algorithm enables us to solve a reverse problem: to find values of t, $\alpha_{\rm inj}$, $Q_{\rm jet}$ and ρ_0 for a real source. Determination of these values is possible by a fit to the four observational parameters of the source: its size D, the volume V, the radio luminosity P_ν and the radio spectrum α_ν, which provides $P_{\nu,i}$ at a number of observing frequencies i=1, 2, 3,... As in KDA, a cylindrical geometry of the source's cocoon is adopted (where its volume is determined by the deprojected length $D/\sin\theta$ and the axial ratio $R_{\rm t}$).

The values of $R_{\rm t}$ are estimated from the low-frequency radio images, and an angle of orientation of the jet axis to the observer's line of sight, θ, is subjectively estimated from the observed asymmetry in the lobes' arms and brightness. The values of these two parameters are given in columns (6) and (7) of Tables (1) and (2), and in columns (5) and (6) in Table (3).

In order to determine luminosities, $P_{\nu,i}$, of the sample sources, the flux density in their lobes at a number of frequencies has to be fixed (i.e. to subtract a flux contribution from the compact components like the radio core and hot spots in these lobes.) This was especially important for the sample sources identified with quasars. The resulting luminosities at three observing frequencies: the lowest frequency applied (74, 151 or 325 MHz), the medium one of 1.4 GHz and the highest one of 4.85 GHz, are given in columns (8)–(10) in Tables (1) and (2), as well as in columns (7)–(9) in Table (3).

The values of other free parameters of the model have to be assumed. These values are listed in Table (4), where $\gamma_{i,\rm min}$ and $\gamma_{i,\rm max}$ are the Lorentz factors determining the energy range of the relativistic particles used in integration of their initial power-law distribution, $\Gamma_{\rm j}$, $\Gamma_{\rm a}$, $\Gamma_{\rm B}$, and $\Gamma_{\rm c}$ are the adiabatic indices in the equation of state for the jet material, the unshocked medium surrounding the lobes, a "magnetic" fluid, and the source (cocoon) as a whole, respectively, and k' is the ratio of the energy density of thermal particles to that of the relativistic particles. The more detailed description of application of the above algorithm to observed radio structures is published in Machalski et al. (2009).

Table 4: Assumed values of the KDA model free parameters

a_0	β	$\gamma_{i,\rm min}$	$\gamma_{i,\rm max}$	$\Gamma_{\rm j}$	$\Gamma_{\rm a}$	$\Gamma_{\rm B}$	$\Gamma_{\rm c}$	k'
10 kpc	3/2	1	10^7	5/3	5/3	5/3	5/3	0

5.5 Results of the modeling

The resulting values of the age and other physical parameters of the sample sources are given in Tables (5), (6) and (7) (for the Sample 1, 2 and 3, respectively). Columns (2) and (3) give the dynamical age, t, and the effective, initial slope of the radio spectrum $\alpha_{\rm inj}$. Columns (4) – (7): (in the logarithmic scale) the jet power, $Q_{\rm jet}$, the central core density, ρ_0, pressure along the jet axis, p_h, and the total energy radiated out during the age of source, $U_{\rm c}$. The age t and the fitted values of $Q_{\rm jet}$ and ρ_0 fulfil the dynamical equation

$$t = \left(\frac{D}{c_1}\right)^{\frac{5-\beta}{3}} \left(\frac{\rho_0 a_0^\beta}{Q_{\rm jet}}\right)^{1/3}. \tag{20}$$

The energy density fulfilling the energy equipartition condition is calculated from

$$u_{\rm eq}(t) = \frac{18\, c_1^{(2-\beta)}}{(\Gamma_{\rm x}+1)(\Gamma_{\rm c}-1)(5-\beta)^2 \mathcal{P}_{\rm hc}} \left(\rho_0 a_0^\beta\right)^{\frac{3}{5-\beta}} Q_{\rm jet}^{\frac{2-\beta}{5-\beta}} t^{-\frac{4+\beta}{5-\beta}}, \tag{21}$$

where $\mathcal{P}_{\rm hc}{=}(2.14{-}0.52\beta) R_{\rm t}^{2.04-0.25\beta}$ is the empirical formula for the pressure ratio along the jet axis and the transverse direction taken from Kaiser (2000). The total radiated energy is simply $U_{\rm c}{=}u_{\rm eq} \times V_{\rm c}$, where the source (cocoon) volume attained at the age t is $V_{\rm c}{=}(\pi/4)\, D^3/(2R_{\rm t})^2$. Column (8) gives the magnetic field strength estimate derived from

$$B = \left(\frac{6}{7}\mu_0 10^{18} u_B\right)^{1/2} = \left(\frac{24}{7} 10^{11} \pi\, u_{\rm B}\right)^{1/2} \ {\rm nT}, \tag{22}$$

where the magnetic field energy density is $u_{\rm B}{=}u_{\rm eq}(1+p)/(5+p)$. The last column (9) gives the actual expansion velocity along the jet axis which is the derivative of the $D(t)$ function

$$v(t) = \frac{dD}{dt} = \frac{3\, c_1}{5-\beta} \left(\frac{Q_{\rm jet}}{\rho_0 a_0^\beta}\right)^{\frac{1}{5-\beta}} t^{\frac{\beta-2}{5-\beta}}. \tag{23}$$

5.6 Observational constrain of the model

5.6.1 Comparison of the Model's Prediction with the Observational Data

The model's predictions, i.e. the dependences of the deprojected linear size and the jet's head velocity on the source's age ($D/sin\phi$ vs t and $v_{\rm h}/c$ vs t, respectively) – are compared with the data determined for the sampled sources and given in Tables (5), (6) and (7). Figure (10) shows the dependence of $D/sin\phi$ on t. The model's predictions are presented for three different sets of values of jet power and redshift: $z = 0.5$ and $Q_{\rm jet} = 10^{37.5}[W]$, $z = 1$ and $Q_{\rm jet} = 10^{38.5}[W]$), $z = 2$ and $Q_{\rm jet} = 10^{39.5}[W]$), marked "1", "2", and "3", respectively. The above dependences predicted in the frame of scenario A are drawn with the solid lines, while these for scenario B – with the dashed lines. The points of bifurcation of the model's predictions into scenario A and scenario B correspond to the halo diameter dependent on redshift, $2R_h(z)$ (on the ordinate axis) and to the related age (on the abscissa axis.) The ends of both solid and dashed lines indicate a maximum size and age at which the predicted expansion velocity reaches the speed of sound. The crosses show the distribution of the GRGs from Sample 1, the full circles – the distant sources (mostly QSOs) from Sample 2, and the open circles – the 3CRR sources from Sample 3.

The dependence of v_h/c on t is shown in Figure (11). The model's predictions and the sample sources are indicated with the lines and symbols as in Figure (10). The rapid increase of v_h/c in the frame of scenario A results from the discontinuities of $\rho(r)$ and $kT(r)$ at the halo-IGM interface (Figure (9)). The three horizontal dotted lines indicate the predicted lower values of the axial expansion velocity, $v_{\rm h,min}/c$, limited by the sound speed at the given values of redshift.

The maximum size which any FRII-type radio source can reach with a given value of $v_{\rm h,min}/c$, (i.e. at the corresponding redshift) depends on the jet power (Figure (12)). The size $D_{\rm max}$ in the frame of scenario A, as a function of $v_{\rm h,min}/c$ (or z), is plotted for three values of $Q_{\rm jet}$ considered above.

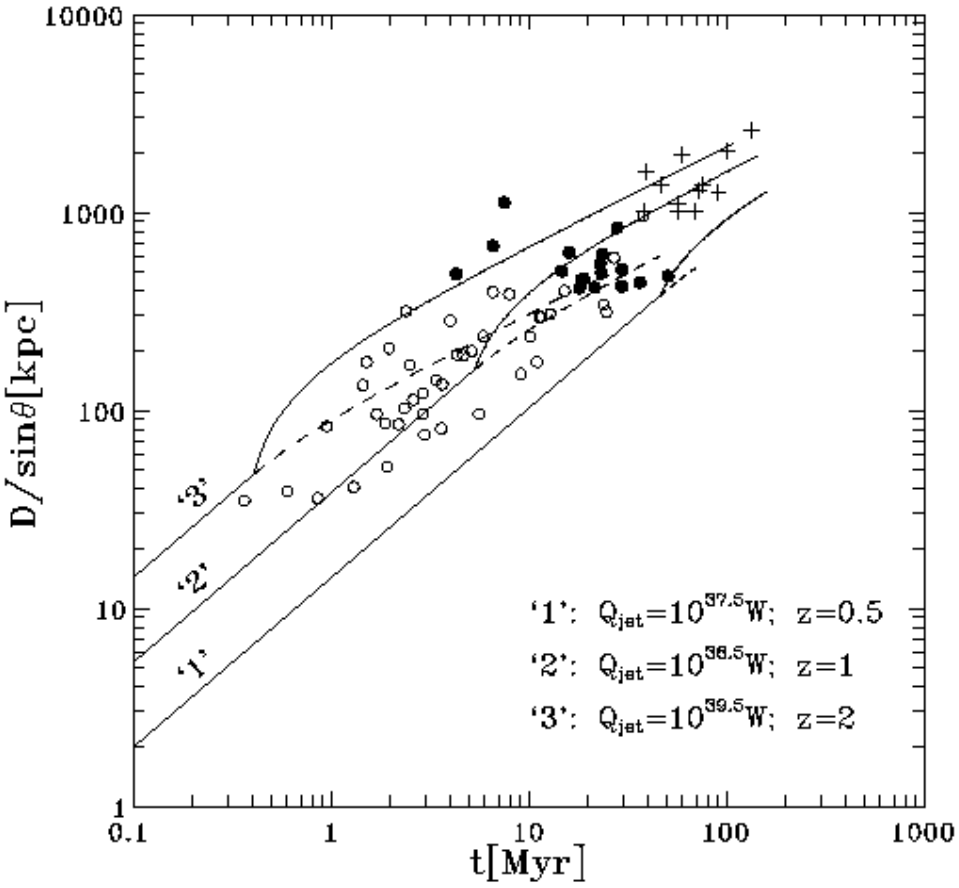

Figure 10: D vs t diagrams for three sets of the jet power and redshift. The solid lines indicate the model predictions in the frame of Scenario A, the dashed lines - in Scenario B. The sources from the Samples 1, 2, and 3 are plotted with the crosses, full dots, and open circles, respectively.

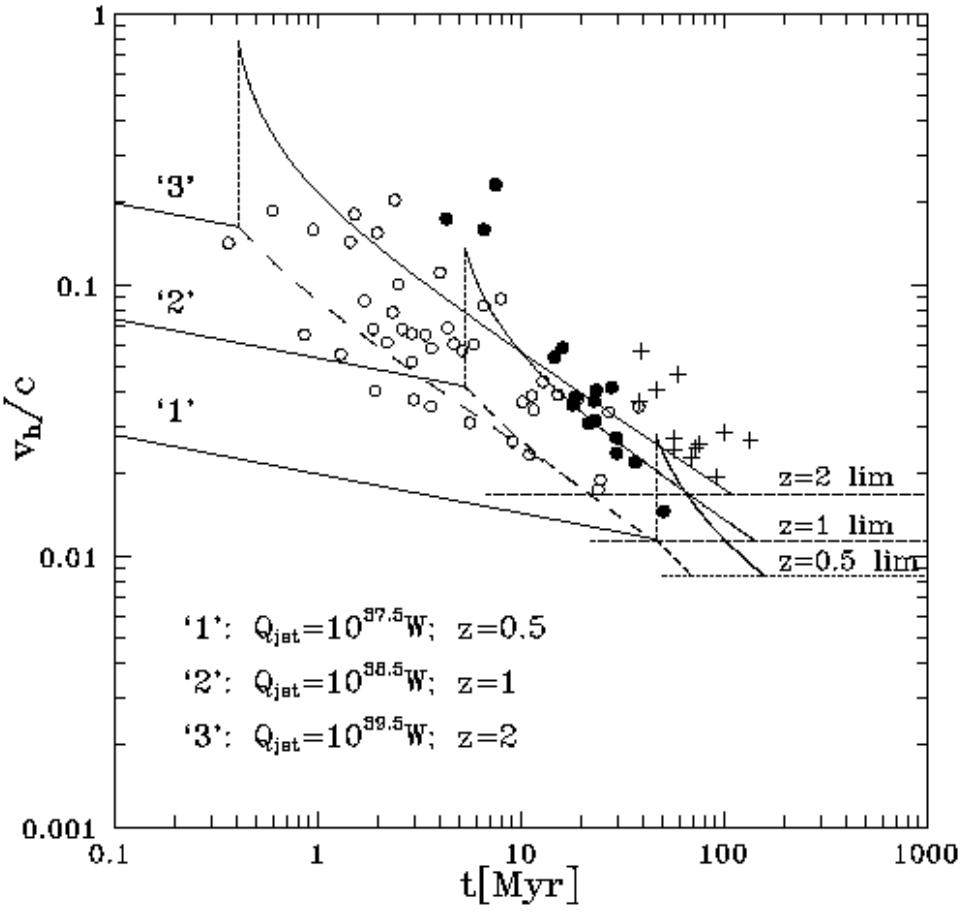

Figure 11: v_h/c vs t diagrams for the same sets of the model parameters as in Figure (10). The three horizontal dotted lines indicate the lower limits for the expansion velocity determined by the sound speed at a given redshift.

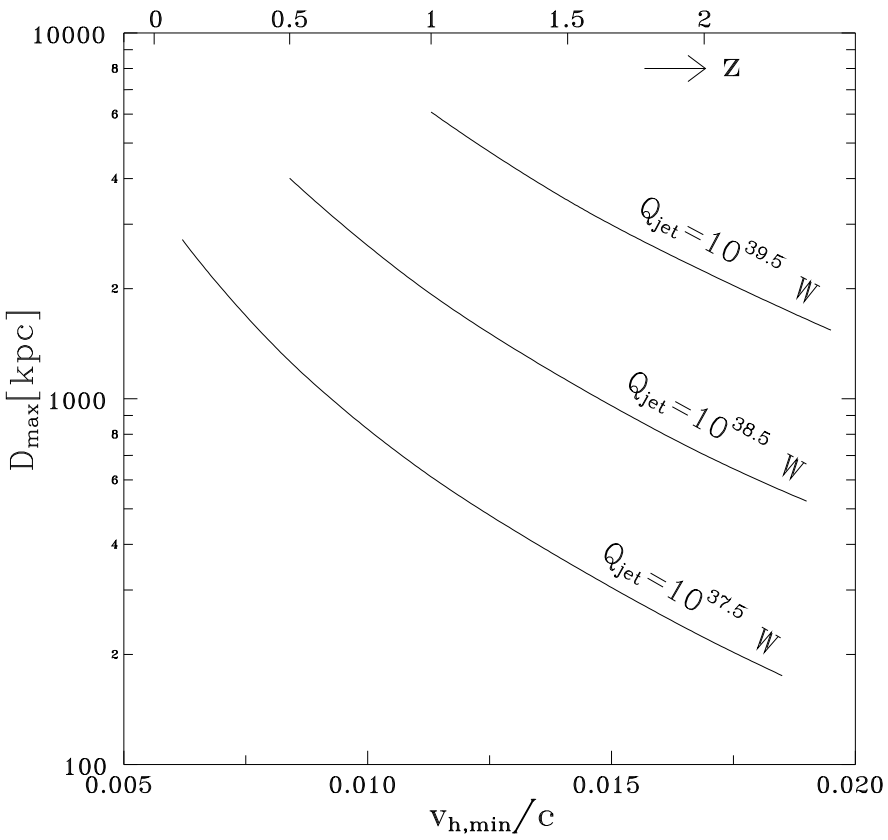

Figure 12: $D_{\max}$ vs $v_{\min}/c$ diagrams for three values of the jet power.

5.6.2 Age and physical parameters of the sample sources

The three samples used differ significantly in the distribution of fitted age of their members. A median of age in the Sample 1, 2 and 3 is 65 ± 8 Myr, 22 ± 2.5 Myr, and 4 ± 1 Myr, respectively. A median linear size in these samples is ∼1330 kpc, ∼510 kpc, and ∼145 kpc, respectively. As the Samples 1 and 2 comprise the largest sources (of FRII type only) each of them in different redshift range, and this range in the Sample 2 is twice the range of the Sample 1 – we compare the $D - z$ dependence for these sources with that found in other samples unlimited in linear size of their members (e.g. Eales 1985; Barthel & Miley 1988). Since the Sample 1, i.e. the sample of known high-redshift GRSs, is very small and consists of 12 sources only, below we also consider 12 of the largest ones from the Sample 2. The relevant medians are: $D_{\rm med} = 1330 \pm 120$ kpc at $z_{\rm med} = 0.60 \pm 0.10$, and $D_{\rm med} = 760 \pm 80$ kpc at $z_{\rm med} = 1.35 \pm 0.20$, respectively. Assuming that $D_{\rm med} \propto (1+z)^{-n}_{\rm med}$, one can find $n \approx 1.5$ which is compatible with a value of this power ∼(1–2) determined in several samples of radio galaxies and quasars (e.g. Kapahi 1989). Therefore the above result agree with the trend observed in much more abundant samples of sources and confirms that the largest linear size, which a source can achieve before dimming below the detection limit, inevitably decreases with redshift irrespective of a cosmological evolution of the IGM (cf. Nilsson et al. 1993).

In order to enlighten the latter problem, it is worth to pay an attention to the pressure at the head of lobes (along the jet's axis), $p_{\rm h}$, given in column 6 of Tables (5), (6) and (7). This pressure is determined in the DYNAGE as

$$p_{\rm h} = \mathcal{P}_{\rm hc}(R_{\rm t}) p_{\rm c}(R_{\rm t}, t), \tag{24}$$

where $\mathcal{P}_{\rm hc}$ is the pressure ratio (cf. Section 5.5), and $p_{\rm c} = (\Gamma_{\rm c} - 1) u_{\rm eq}$, where $u_{\rm eq}$ is given by Eq. (21). The median of this pressure, $p_{\rm h,med}$, for sources in the Sample 1 and Sample 2 is $\sim 10^{-12.0}$ N/m^2 and $\sim 10^{-10.8}$ N/m^2, respectively, thus a (mean) pressure at the head of lobes of the sources within the redshift range $z[1,\ 2]$ is about 16 times higher than that for the sources within $z[0.5,\ 1]$. If so, it is more than twice higher than a ratio implied from the formula giving pressure of a non-relativistic, homogeneous IGM in thermal equilibrium, $p(z) = p_0(1+z)^5$, where p_0 is the present-day pressure (Subrahmanyan & Saripalli 1993). We return to this point in the Section 5.7.

5.7 Discussion of the results and conclusion

The distribution of sources on the planes $D/sin\phi$ – t and $V_{\rm h}/c$ – t (in Figures (10) and (11), respectively) is more or less compatible with model's prediction, however the samples used to constrain the model may be to small to be decisive. So, much larger samples of sources with reliably determined ages would support or impair the inferences drawn as follows:

(i) Scenario B is rather excluded because both the maximum size, $D_{\rm max} \sim 600$ kpc, and the corresponding age, $t_{\rm max} \sim 70$ Myr allowed by the model are evidently smaller and younger then the observed values of those parameters for the sample sources. Also high-dynamics radio observations show no evidence for a flaring of the jets in FRII-type sources; oppositely the jets in these sources are rather recollimated in vicinity of the radio core.

(ii) As expected, the inferred expansion velocity, $\mathrm{v_h}/c$, of all the sources used to constrain the G-KW model are higher than the limiting sound speed marked in Figure (11). This result confirms a common believe that the heads of lobes of FRII type sources are overpressured with respect to the external gaseous medium. We note that the lowest expansion velocities of the largest sources, i.e. these in the Samples 1 and 2, are comparable to those of much smaller sources in the Sample 3.

(iii) The age of the three sources in Sample 2 is probably underestimated and the corresponding expansion velocity – overestimated (the three full dots with $t < 10$ Myr and $\mathrm{v_h} > 0.1\,c$ in Figures (10) and (11)) due to possible relativistic effects (cf. Arshakian & Longair 2000). All are classified as quasars, and the two of them (J0809+2912 and J1550+3652) are highly asymmetric in their lobes' brightness. If a probable anisotropic radiation is discerned and the proper luminosity of the cocoon is taken into calculations, the age of these sources would be older and the expansion velocity – lower than the values in Table (6).

(iv) The pressure in the diffuse lobes of the largest radio sources seems to offer a tool useful for an estimation of the IGM pressure. If the axial pressure in lobes of the largest observed sources, especially these in the Sample 2, is close to equilibrium with the IGM pressure, the inferred values of $p_{\rm h}$ would suggest even stronger density evolution of the IGM than $\rho_{\rm IGM} \propto (1+z)^3$. However, radio images of the sources in the Sample 2 evidently indicate a presence of hot spots which, in turn, may confirm that the hot spot regions are highly overpressured with respect to the IGM, and the actual age of sources cannot be considered as a lifetime. Moreover, the "DYNAGE" fits show that the jet powers of the most distant sources are significantly higher than that for sources of a similar age but at low redshifts $z < 0.2$. The median age in the Sample 2 is ~ 22 Myr. An inspection of the compilation of over 200 radio galaxies and quasars with the dynamical ages fitted using the "DYNAGE" method (the data unpublished yet) resulted in only 7 radio galaxies of age of about 25 Myr and lying within the redshift range $z \in [0.1, 0.2]$. These galaxies and their observational and dynamical parameters are listed in Table (8).

The median jet power, $Q_{\rm jet,med}$, in the Sample 2 (cf. Table (6)) is $\sim 1.8 \times 10^{39}$ W, while that for the galaxies in Table (8) is $\sim 2.8 \times 10^{37}$ W. We argue that this is very unlikely to find so young FRII type radio sources at redshift below 0.2 and driven by jets more powerful than 10^{38} W. (although this may be partly caused by the selection effect). In fact, searching for high-redshift sources we probe a much larger space volume than the volume corresponding to a low redshift. Probably therefore this

Table 5: Age and physical parameters of the sources in Sample 1.

IAU name	t [Myr]	$\alpha_{\rm inj}$	$\log Q_{\rm jet}$ [W]	$\log \rho_0$ [kg/m^3]	$\log p_{\rm h}$ [N/m^2]	$\log {\rm U_c}$ [J]	$\rm B_{eq}$ [nT]	$\rm v_h/c$
(1)	(2)	(3)	(4)	(5)	(6)	(7)	(8)	(9)
J0037+0027	59.0	0.506	38.474	−23.311	−12.13	53.00	0.16	0.047
B0654+482	57.0	0.555	38.296	−22.741	−11.68	52.92	0.33	0.024
J0750+656	39.0	0.507	38.563	−23.670	−12.20	53.02	0.18	0.057
B0821+695	135.0	0.645	38.710	−22.968	−12.45	53.84	0.17	0.027
B0854+399	69.0	0.522	38.362	−22.992	−12.04	53.24	0.29	0.023
B1058+368	57.0	0.545	38.384	−22.741	−11.66	52.98	0.32	0.027
J1130−1320	100.0	0.537	39.005	−22.431	−11.71	53.90	0.33	0.028
B1602+376	47.0	0.524	38.621	−23.648	−12.35	53.35	0.22	0.041
B1636+418	38.0	0.526	38.367	−23.229	−11.82	52.83	0.29	0.037
B1834+620	75.0	0.533	38.455	−22.688	−11.80	53.18	0.28	0.026
J1951+706	73.0	0.525	38.061	−22.921	−12.02	52.73	0.25	0.025
J2234−0224	(91.0)		(38.1)	(−22.55)				0.019

is why the only low-redshift and very powerful radio galaxy known is Cygnus A with $t \approx 8$ Myr, $D = 135$ kpc, and $Q_{\rm jet} \approx 1.4 \times 10^{39}$ W (cf. Machalski et al. (2007a), the above result strongly suggests that the dynamical evolution of FRII type radio sources at high redshifts (in earlier cosmological epochs) is different and faster than that of sources at low redshifts. The model constrained in this Section implies that giant-sized sources (with $D > 1$ Mpc) can exist at redshifts as high as ~ 2, however only if their jets are powerful enough.

Table 6: Age and physical parameters of the sources in Sample 2.

IAU name	t [Myr]	$\alpha_{\rm inj}$	$\log Q_{\rm jet}$ [W]	$\log \rho_0$ [kg/m^3]	$\log p_{\rm h}$ [N/m^2]	$\log {\rm U_c}$ [J]	$\rm B_{eq}$ [nT]	$\rm v_h/c$
(1)	(2)	(3)	(4)	(5)	(6)	(7)	(8)	(9)
J0245+0108	18.5	0.603	39.295	−22.153	−10.30	53.45	1.74	0.038
J0809+2912	7.5	0.496	39.715	−24.555	−11.65	53.59	0.41	0.233
J0839+2928	21.5	0.535	38.655	−23.031	−11.44	52.93	0.62	0.031
J0857+0906	14.6	0.564	39.111	−22.629	−10.48	53.08	1.13	0.054
J0947+5154	50.5	0.624	38.508	−21.616	−10.62	53.06	1.12	0.015
J0952+0628	23.0	0.554	38.806	−22.453	−10.75	52.98	0.89	0.037
B1011+365	18.1	0.542	38.752	−22.686	−10.76	52.94	1.00	0.036
J1030+5310	28.0	0.548	38.605	−23.408	−11.77	53.05	0.38	0.042
B1108+359	23.3	0.655	39.560	−21.913	−10.22	53.90	2.18	0.031
B1109+437	4.3	0.544	40.028	−23.238	−10.04	53.47	1.87	0.175
J1130+3628	29.5	0.536	38.180	−22.898	−11.39	52.53	0.47	0.027
J1550+3652	6.6	0.511	39.340	−24.327	−11.42	53.16	0.53	0.160
J1706+3214	36.6	0.572	38.460	−22.340	−11.00	52.90	0.72	0.022
B1723+510	23.5	0.661	39.676	−21.881	−10.09	53.92	1.98	0.041
J2345−0936	29.6	0.564	38.797	−22.308	−10.82	53.23	1.05	0.024
B2352+796	16.0	0.578	39.747	−22.155	−10.08	53.74	1.83	0.058

(v) A differentiation of the jet's (highest) power at high and low redshifts perhaps would be a strong argument for the theoretical speculations about its dependence on the properties of a black hole (BH) in AGN: the spin of the BH (Blandford & Znajek 1977) and/or the accretion process and its rate (Sikora, Stawarz & Lasota 2007; Sikora 2009). This is very likely that the accretion of matter onto the BH must play a dominant role in the jets' production. This led to a presumption that more powerful jets can be due to a larger amount of material available for the accretion processes inside AGN formed at earlier cosmological epochs.

Reasuming the above one can conclude as follows:

— An observational quest for the largest radio sources of FRII type at high redshifts $1 < z < 2$ resulted in the sample of 25 sources listed in Table (2), where 20 of 25 are found in this paper. Because the finding sky survey used was the optical SDSS survey, all the newly radio-identified optical objects appear to be quasars with the (projected) linear size from ∼400 kpc to ∼1200 kpc. The above bias precluded a detection of large, most distant and low-luminosity radio galaxies whose parent optical counterpart will likely be of ∼(22–24) R mag.

— Though the samples used to constrain the model are small, the observational data seem to be concordant with the predictions in the frame of Scenario A. However much larger samples of distant sources with reliably determined ages will be more

Table 7: Age and physical parameters of the sources in Sample 3.The age solution for the sources which name is followed by the asterix is provided by J. Machalski.

IAU name	t [Myr]	$\alpha_{\rm inj}$	$\log Q_{\rm jet}$ [W]	$\log \rho_0$ [kg/m^3]	$\log {\rm p_h}$ [N/m^2]	$\log {\rm U_c}$ [J]	$B_{\rm eq}$ [nT]	$v_{\rm h}/c$
(1)	(2)	(3)	(4)	(5)	(6)	(7)	(8)	(9)
3C6.1	5.12	0.564	39.298	−22.891	−10.08	53.03	2.75	0.057
3C13	5.87	0.583	39.606	−22.549	−9.81	53.35	3.41	0.060
3C22	4.68	0.559	39.316	−22.799	−9.92	52.96	3.03	0.060
3C34	24.0	0.630	39.012	−21.434	−9.86	53.22	2.56	0.018
3C41	1.52	0.534	39.580	−24.250	−10.34	52.85	2.21	0.182
3C54*	15.2	0.562	39.141	−22.280	−10.26	53.17	1.64	0.039
3C65	3.40	0.588	39.604	−22.881	−9.74	53.23	4.65	0.065
3C68.1*	7.94	0.564	39.784	−23.053	−10.43	53.66	1.70	0.089
3C68.2	4.35	0.771	40.209	−22.406	−9.41	53.94	6.97	0.076
3C169.1	24.7	0.575	38.611	−22.230	−10.68	53.02	1.37	0.019
3C184	0.37	0.577	39.471	−23.395	−8.46	52.01	12.83	0.142
3C196	0.60	0.579	40.042	−23.374	−8.91	52.82	10.14	0.188
3C204	11.6	0.625	39.350	−21.969	−9.76	53.36	3.28	0.035
3C205	1.45	0.584	39.949	−22.840	−8.98	52.95	6.76	0.143
3C217	1.87	0.588	39.301	−22.481	−8.97	52.41	7.08	0.068
3C220.1	11.0	0.610	38.900	−21.653	−9.53	52.78	3.74	0.024
3C220.3	1.92	0.580	38.955	−22.345	−8.97	52.21	9.01	0.040
3C239*	2.90	0.673	39.903	−22.904	−9.68	53.60	7.61	0.052
3C247*	1.70	0.547	39.182	−23.182	−9.88	52.50	3.77	0.087
3C254	5.60	0.627	39.172	−22.240	−9.60	52.98	5.18	0.031
3C263	12.8	0.557	39.126	−22.584	−10.44	53.15	1.53	0.044
3C263.1*	1.30	0.600	39.133	−23.110	−9.40	52.43	8.83	0.050
3C265*	27.0	0.609	39.415	−21.905	−10.25	53.72	1.66	0.034
3C266*	0.86	0.639	39.462	−22.674	−8.64	52.48	16.12	0.065
3C268.4	0.95	0.574	39.809	−23.280	−9.15	52.70	6.56	0.159
3C270.1*	2.35	0.568	39.708	−23.458	−10.07	53.26	4.30	0.079
3C272*	19.0	0.557	39.132	−22.484	−10.57	53.37	1.32	0.038
3C280*	2.60	0.560	39.520	−23.578	−10.23	53.16	3.76	0.068
3C280.1	2.50	0.574	39.795	−22.635	−9.23	53.03	5.24	0.100
3C289*	3.60	0.571	39.080	−23.296	−10.30	52.88	3.92	0.035
3C292*	38.0	0.566	39.180	−22.266	−10.86	53.60	0.81	0.035
3C294*	3.65	0.683	39.950	−22.611	−9.54	53.67	6.95	0.058
3C322*	4.00	0.557	39.908	−23.310	−10.16	53.58	2.66	0.111
3C324*	2.20	0.584	39.471	−23.117	−9.71	52.98	5.91	0.061
3C325*	2.90	0.566	39.320	−23.197	−9.95	52.89	3.77	0.066
3C330*	6.60	0.543	39.404	−22.699	−9.98	52.93	1.82	0.084
3C337	11.3	0.553	38.999	−22.853	−10.64	53.10	1.53	0.039
3C352	2.96	0.595	38.986	−22.631	−9.55	52.53	5.78	0.038
3C427.1*	9.10	0.592	38.903	−22.498	−10.18	52.98	2.91	0.026
3C437*	2.42	0.546	40.113	−23.405	−9.80	53.37	2.78	0.205
3C441*	10.0	0.556	38.984	−22.764	−10.45	53.05	1.91	0.037
3C470	1.97	0.550	39.973	−23.063	−9.41	53.10	4.25	0.155

Table 8: Observational and dynamical parameters of seven FRII-type radio galaxies with $0.1 \lesssim z \lesssim 0.2$, for which their dynamical age determined with the DYNAGE is 12 Myr<t<36 Myr.

Name	z	D[kpc]	$\log P_{1400}$ [W/(Hz·sr)]	t[Myr]	$\log Q_{\rm jet}$ [W]	$\log \rho_0$ [kg/m^3]
3C332	0.1515	229	25.07	36	37.45	−22.60
3C349	0.205	287	25.46	29	37.91	−22.44
3C357	0.1664	296	25.20	24	37.77	−22.96
3C381	0.1605	199	25.29	25	37.66	−22.76
B0908+376	0.1047	229	24.12	20	36.50	−23.59
B1130+339	0.2227	99	24.98	12	37.38	−23.01
B1457+292	0.146	172	24.15	28	36.80	−23.99

decisive for the above aim.

— The derived lowest values of the lobes' head pressure, $p_{\rm h}$, evidently higher than the limiting sound speed at different redshifts, strongly suggest that heads of even the largest sources at high redshifts are still overpressured with respect to the IGM.

– An existence of giant-sized radio sources at high redshifts is possible due to extremely high power of their jets up to $\sim 10^{40}$ W. Such the highest jet powers are likely related to the accretion processes onto massive black holes in the central AGN, which might be very efficient in the nuclei formed at earlier cosmological epochs.

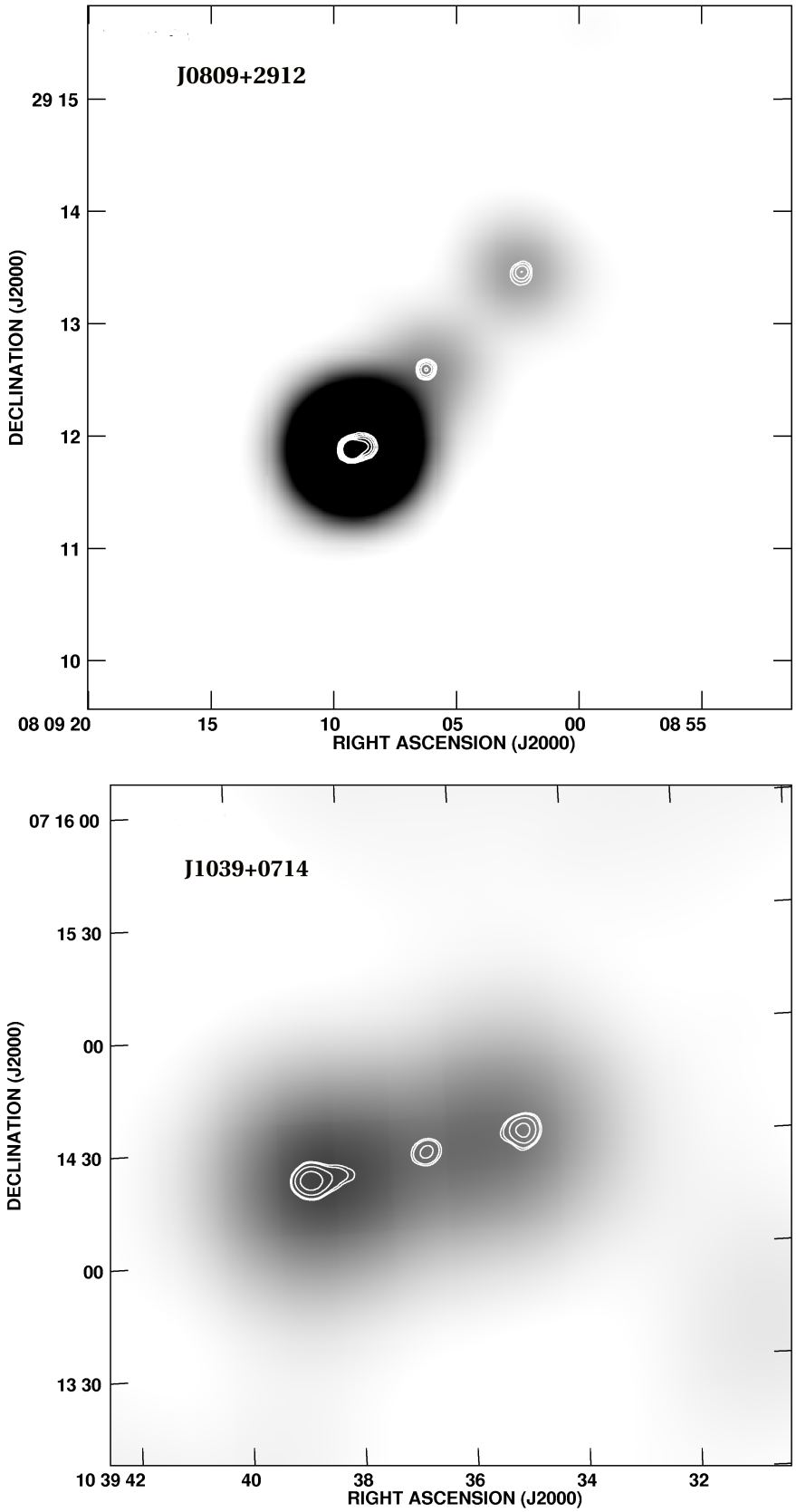

Figure 13: 1400 MHz VLA maps of the sources J0809+2912 and J1039+0714. The NVSS images (gray scale) are combined with the FIRST contour maps. Total intensity, logarithmic contours are spaced by a factor of 2, starting with a value of 1.0 mJy/beam (except J1434-0123 starting with 0.2 mJy/beam).

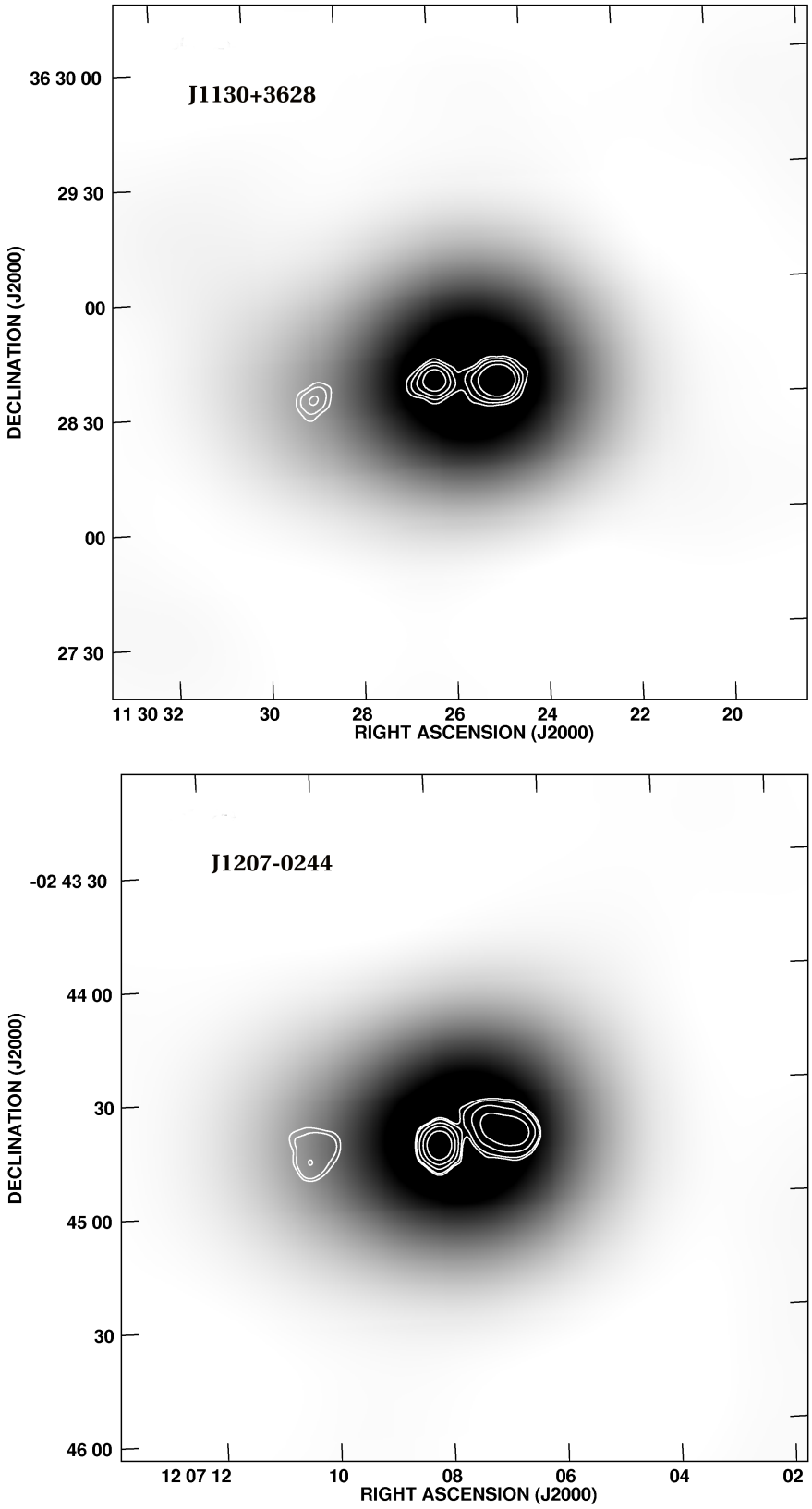

Figure 14: The same as in Figure (13) but for J1130+3628 and J1207-0244

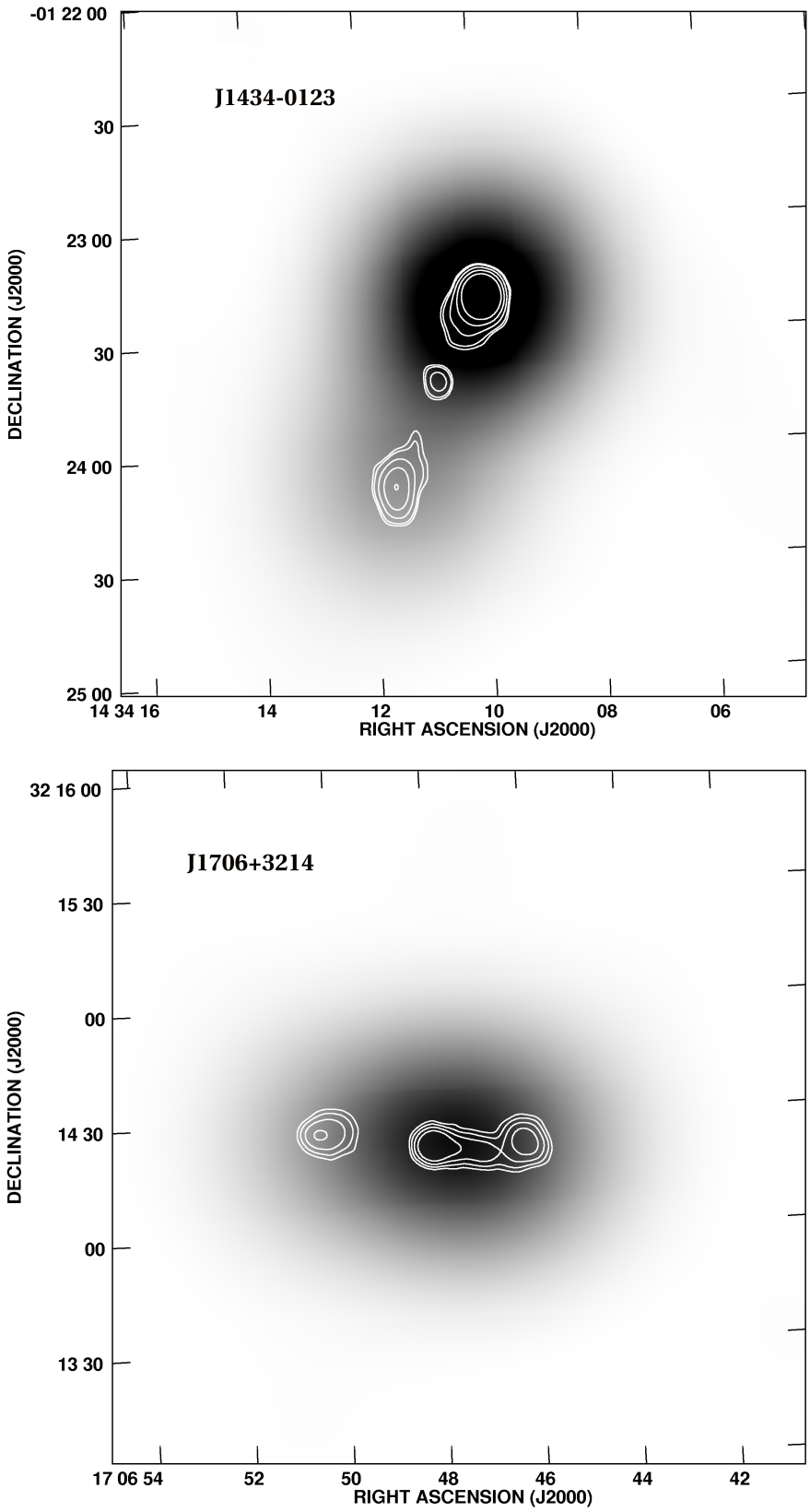

Figure 15: The same as in Figure (13) but for J1434-0123 and J1706+3214

6 Modification of KDA model to its version applicable for radio sources with non-continuous activity

6.1 The argument for an extension of the basic KDA model

The KDA model of radio galaxy's dynamical evolution is based on the assumption that the nuclear activity of FR II type radio source is continuous. That model is applicable only for the case of young radio sources with regular radio spectra. However, several observations of FR II type radio sources indicate that their high frequency spectra are steeper than $\alpha_{inj} + 0.5$ and their lobes seem to be no longer powered with an inflow of new, relativistic particles. In such a case they may be relatively old sources in which their nuclear activity stopped at some time in the past. Among the observed radio sources with steep spectra one can find many examples of giant radio sources and so-called radio sources with restarted activity (the double-double radio structure composed of outer and inner lobes) where the high-frequency spectra of the outer lobes are significantly steeper than expected from the KDA continuum-injection model (see Section 3.4.3).

Applying the original KDA model to the FR II type radio sources with highly steepened high frequency spectrum usually results in very poor fit of the model spectrum. In particular, it is difficult to determine a satisfactory age solutions by the best fit of model's free parameters to the observables. That implies that studying the dynamics of such radio sources demands a more complex tool - extended dynamical model for FR II type sources.

6.2 Extension of the original KDA model

6.2.1 General basis of the extended model

The extended model of the dynamics of FR II type radio sources with steeply bent high frequency spectra is developed in this Thesis. The following basic aspects are taken into account while developing it.

1. The new model has to describe the process of radio power's ceasing after termination of the inflow of relativistic particles to the lobes. After switching off the jet, the radio lobes starts a quicker loose of its radio power than during the continuous injection process. This appears in a much stronger steeping of the observed radio spectra at high frequencies due to rapid decrease of the highest-energy particles.

2. The information that the jets stopped to supply energy to the radio structure propagates from the AGN to the radio lobes with the speed of sound. There are arguments for a relatively low internal sound speed in the lobes. These conditions are fulfilled in the presence of significant mixing of the lobe material with the surrounding gaseous environment (Kaiser at al., 2000). It implies that after switching off the jets,

for a long time the adiabatic evolution of the cocoon is the same as it was before terminating the nuclear activity. However, for small and overpressured (with respect to the external medium) cocoon, the internal sound speed can be high and its adiabatic evolution can slow down in a relatively short time. Such a scenario was considered by Kaiser & Cotter (2002) for an inactive spherical source (their model B). That model of the source dynamics after the jet switch off is applied in the extended KDA model presented in this Section.

3. The extended model demands one more free parameter of the model i.e. the time of the jet's "switch off", t_{br}.

6.2.2 Adiabatic evolution of the cocoon in the case of terminated nuclear activity

The lifetime of the phase of preserved lobes expansion after jet's termination is strongly dependent on the internal sound speed. In the case of relatively small and young sources, or in the absence of significant mixing of the lobes material with the external gas, it may have very high values. The information about the jet termination is then travelling very fast through the cocoon and the dynamics and expansion velocity of the heading shock wave changes quickly due to this process. On the contrary, when the source is relatively large and its internal sound speed is low, the information about jets termination propagates very slowly. For a long time the lobes continues to expand at the same rate as it was in the active phase.

After switching off the supply of new particles to the cocoon, the lobe may still be overpressured with respect to the external medium and it continues to expand behind the bow shock. It enter so-called "coasting phase". As mentioned in subsection 6.2.1, the dynamical evolution of a spherical source (supernova remnant) during that phase was analysed by Kaiser & Cotter (2002). They assumed that the bow shock of the source is spherical and evolve with time according to the radius of $R_{\rm S} \propto t^{2/(5-\beta)}$, the power-law density distribution of the external gas is $\rho_a(r) = \rho_0(r/a_0)^{-\beta}$ (cf. Section 3.1), and the pressure of the cocoon, $p_{\rm c}$, is uniform. With these assumptions they solved equation of state for the spherical approximation of the source. Their solution is a steady-state similarity solutions from which one can identify the source radius $R_{\rm c}$ with the lobe's length D in the KDA model. After some transformation the extended formula for the cocoon length, describing its adiabatic evolution before and after the termination of jets activity, is given by:

$$D(t,t_{br}) = \begin{cases} c_1 \left(\frac{Q_{jet}}{\rho_0 a_0^{\beta}}\right)^{1/5-\beta} t^{3/5-\beta}, & t < t_{br} \\ D(t_{\rm br}) \left(\frac{t}{t_{br}}\right)^{\frac{2(\Gamma_{\rm c}+1)}{\Gamma_{\rm c}(7+3\Gamma_{\rm c}-2\beta)}}, & t \geq t_{br} \end{cases} \tag{25}$$

where $\Gamma_{\rm c}$ is the adiabatic index of the cocoon and $D(t_{\rm br})$ is its length at the time of

switching off the energy supply.

6.2.3 Spectral ageing in the synchrotron theory

A single, relativistic particle with the energy $\gamma \gg m_0c^2$ decelerates in the magnetic field of strength B and in the presence of photons of the CMB. Its energy changes according to the formula:

$$-\frac{d\gamma}{dtd\nu} = \frac{C_1}{C_2^2} B sin(\theta) F(\frac{\nu}{\nu_c}) \tag{26}$$

where ν_c is a "critical" frequency near the maximum of emission, and

$$F(\frac{\nu}{\nu_c}) = \frac{\nu}{\nu_c} \int_{\frac{\nu}{\nu_c}}^{\infty} K_{5/3}(z)\ dz, \tag{27}$$

where $K_{5/3}$ is the modified Bessel function of 5/3 order. Hereafter C_1 and C_2 are constants defined by Pacholczyk (1970). The total energy spectrum of radiating particles is calculated by integrating Eq. (27) over all frequencies, including energy loses due to the magnetic field, B, and the magnetic equivalent B_{iC} of the inverse Compton scaterring with CMB photons:

$$-\frac{d\gamma}{dt} = C_2\{(Bsin\theta)^2 + B_{\rm iC}^2\}\gamma^2. \tag{28}$$

This energy loss process, described by Eq.(28) causes a characteristic "break energy" in the energy spectrum comprising particles with different energies. If the source is supplied by a constant flow of the particles (the Continous Injection process, hereafter CI), the "break energy" at source's age, t, is equal to:

$$\gamma_{\rm br,CI}^{-1} = C_2\{(Bsin\theta)^2 + B_{\rm iC}^2\}^2 t \tag{29}$$

Appearance of γ_{br} causes a "break frequency" in the shape of the observed frequency spectrum:

$$\nu_{\rm br} = C_1 B sin(\theta) \gamma_{\rm br}^2 \tag{30}$$

The break frequency depends on the value of the pitch angle of the electrons and of the strength of the magnetic field present at the time of observations. The Jaffe - Perola (hereafter referred to JP) model assumes that the pitch angle of electron distribution

in the source is mostly isotropic and all the particles can have any possible pitch angles. If the time of magnetic field's izotropisation is small relative to the source's age, the break frequency is given by:

$$\nu_{\rm br,JP} = \frac{C_1}{C_2^2}\frac{B}{\{(2/3B^2 + B_{\rm iC}^2)(t - t_{\rm br})\}^2} \tag{31}$$

where $C_1/C_2^2 = 2.51422 \cdot 10^{12}$ and $B_{iC} = 0.318(1+z)^2$nT.

6.2.4 The analytical formula for integration of radio power

In the numerical modeling presented in This thesis, I use the bases of both CI and JP models of the spectral aging to introduce the new variable, $\nu_{\rm br}$, into the basic KDA model of the radio source's dynamics.

According to the superposition principle the final formula for total radio power of the selected source at a given frequency can be rewritten as the sum of two integrals. In the extended model presented here, the first integral gives the source power calculated until the time of the jet energy cut-off, t_{br}, while the second one adds the radio power emitted from t_{br} until the actual age of the source, t. Therefore, the total power of a source (eg. its lobe) can be written as:

$$P_\nu(t) = \begin{cases} P_\nu(t_{min}, t_{br}) + P_\nu(t_{br}, t) & for\ t_{br} > t_{min} \\ P_\nu(t_{min}, t) & for\ t_{br} \leq t_{min} \end{cases} \tag{32}$$

In the above equation the first term corresponds to the integral given by Eq.(8) in Section (3.2) where the upper limit of integration is changed from t to $t_{\rm br}$. The second term is given by:

$$P_\nu(t_{br}, t) = \frac{\sigma_T c}{6\pi\nu}\frac{r}{r+1} Q_{jet} P_{hc}^{\frac{(1-\Gamma_c)}{\Gamma_c}} \int\limits_{t_*}^{t} G(t_i) H(t_i) dt_i, \tag{33}$$

where $t_* = t_{br}$ if $t_{br} > t_{min}$ and $t_* = t_{min}$ if $t_{br} \leq t_{min}$,

$$H(t_i) = n_0(t_i)\frac{\gamma^{3-p} t_i^{a_1/3(p-2)}}{\{t^{-a_1/3} - a_2(t,t_i)\gamma\}^{2-p}}\left(\frac{t}{t_i}\right)^{-a_1(1/3+\Gamma_B)},$$

$$G(t_i) = \frac{\int\limits_0^1 F(\frac{\nu/\nu_{\rm br,JP}}{x^2}) x^{-p}(1-x)^{p-2} dx}{\int\limits_0^1 F(\frac{\nu/\nu_{\rm br,CI}}{x^2}) x^{-(p+1)}\{1-(1-x)^{p-2}\} dx + \int\limits_1^\infty F(\frac{\nu/\nu_{\rm br,CI}}{x^2}) x^{-(p+1)} dx},$$

and the function F is given by Eq.(27). It should be noted that transient values of $\nu_{\rm br,JP}$ and $\nu_{\rm br,CI}$ are functions of t_i, i.e. the time of initial acceleration of radiating particles. The sum of two integrals in the denominator of the function $G(t_i)$ results from different form of these integrals in the cases of $\nu < \nu_{\rm br}$ and $\nu \geq \nu_{\rm br}$. It is calculated at every step of radio power integration. All of the infinitesimal values of integrated radio power are multiplied by this function.

6.2.5 Predictions of the extended model

In order to study the influence of the extended model parameters on the observed radio spectrum and the $P_\nu - D$ diagram, I use a fiducial source with a set of fixed model parameters: α_{inj}=0.51, R_t=3.0, β=1.5, k'=0, Γ_j=Γ_C=Γ_B=5/3, a_0=10 kpc, Q_{jet}=10^{38} W and ρ_0=10^{-22} kg m^{-3}.

Figure (16) shows the radio power spectra (P_ν vs. ν) of the fiducial source expected from the extended model (solid curves) in comparison to the spectra predicted with the "continuum injection" KDA model (dashed curves). These spectra are calculated for two different values of redshift, z, and the jet switch off-time, $t_{\rm br}$.

Figure (17) shows the P_{178} - D diagrams for the fiducial source at three different values of redshift, z=0.1, 1 and 3, and for two different values of $t_{\rm br}$: 10 Myr and 100 Myr (solid curves). As in Figure (16), the dashed curves indicate the relevant P_{178} - D diagrams expected from the KDA model for a comparison. Figure (18) shows the same plots, but for three different values of β: 0, 1.5 and 1.9 and for z=0.1. Finally, Figure (19) present analogous P_{178} - D diagrams for the fiducial source with three different values of ρ_0: 10^{-21}, 10^{-22} and 10^{-23} kg$\cdot m^{-3}$, and with fixed β=1.5.

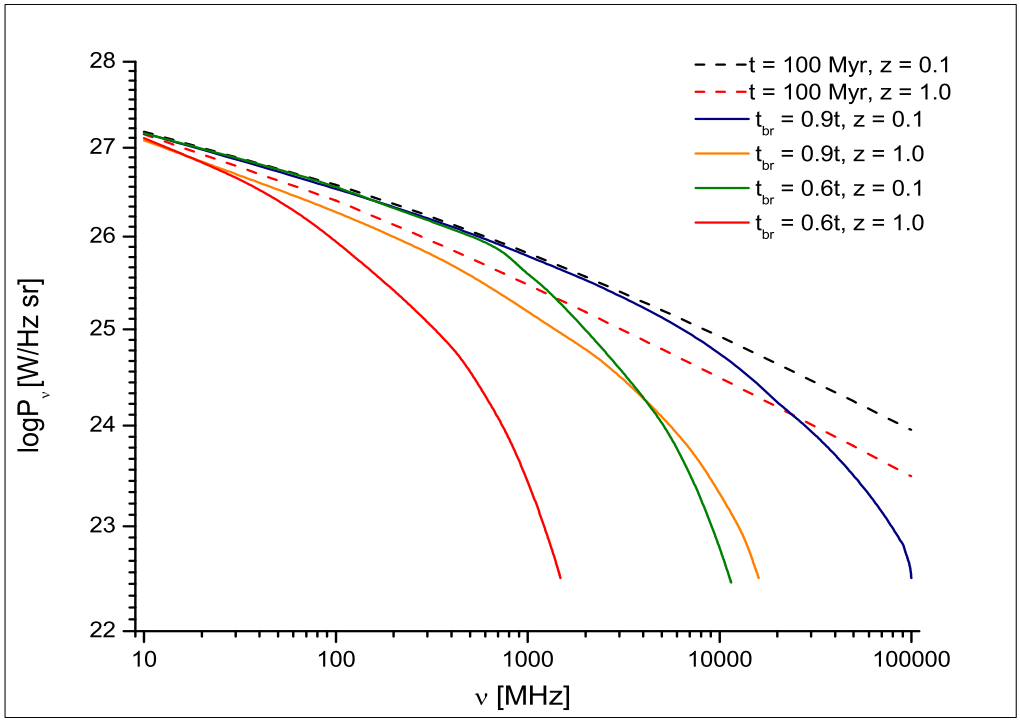

Figure 16: A comparison of the radio power spectrum (P_ν vs. ν) calculated for the extended model (solid lines) and the KDA model (dashed lines) for the fiducial source with two different values of z and $t_{\rm br}$.

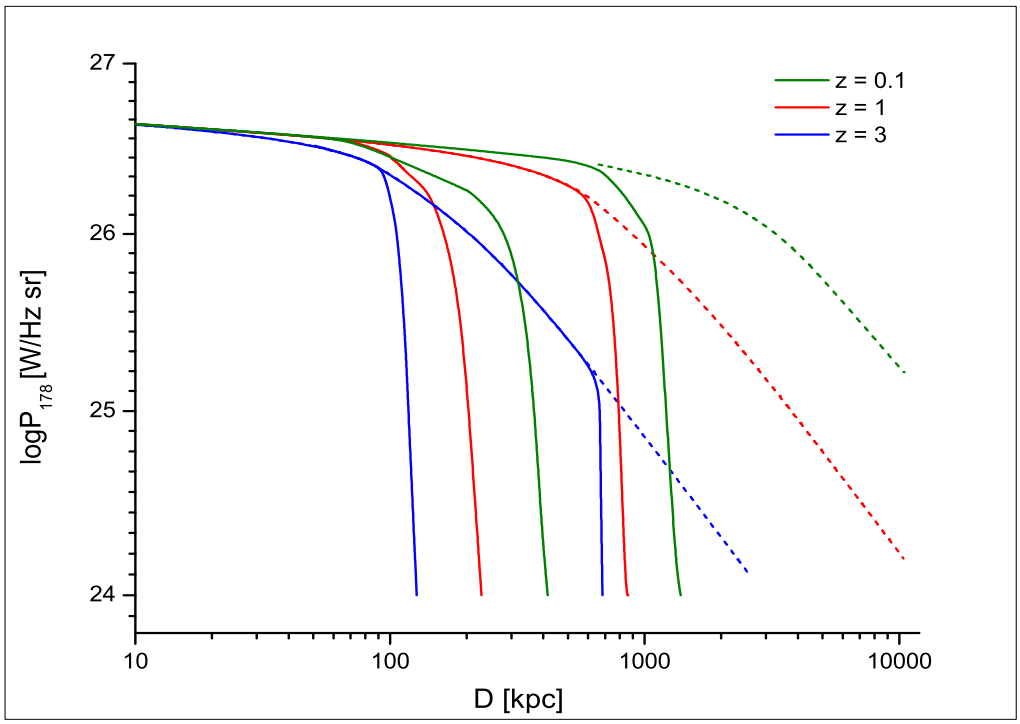

Figure 17: A comparison of the $P_{178} - D$ diagrams predicted by the KDA model and the extended model for different values of z and $t_{\rm br}$ (cf. the text). Calculations are performed for the same set of the fiducial source parameters as in Figure (16). Solid lines shows predictions of the extended model while the dashed lines trace predictions of the KDA model.

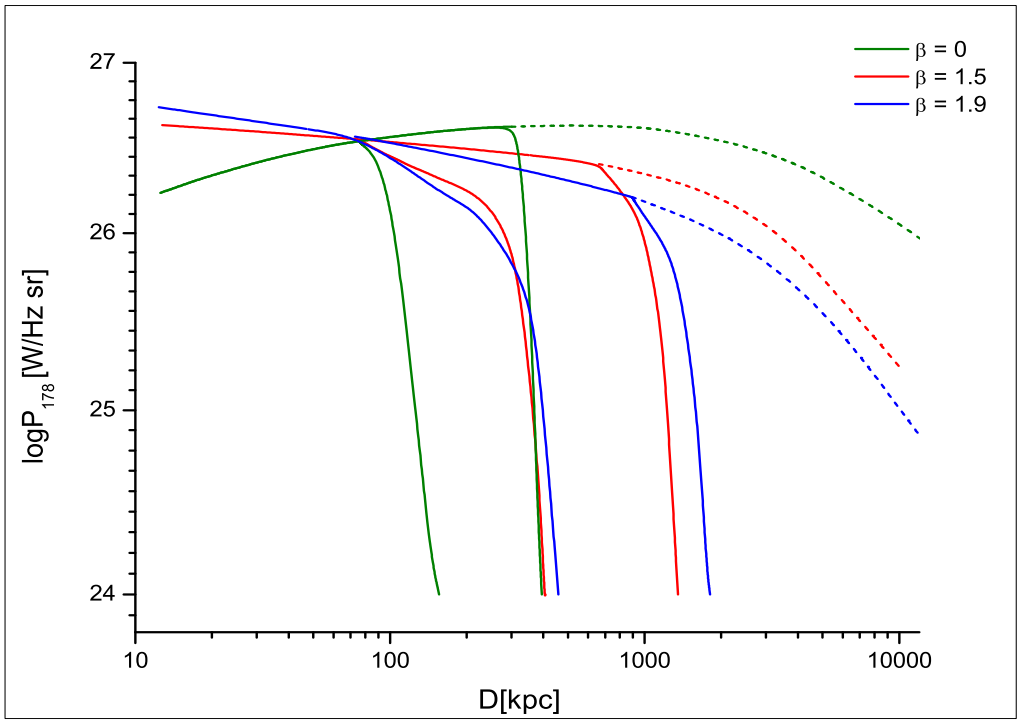

Figure 18: A comparison of the $P_{178} - D$ diagrams predicted by the KDA model and the extended model for different values of β and $t_{\rm br}$. Calculations are performed for the same set of source's parameters as on Figure (16), but with $z = 0.1$ only.

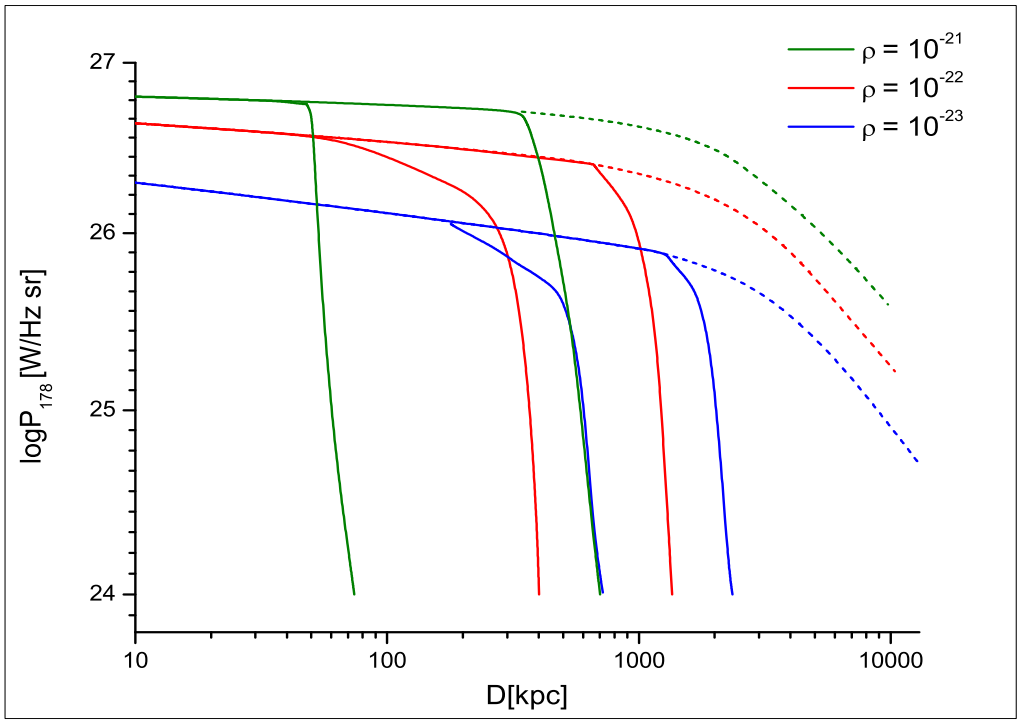

Figure 19: A comparison of the $P_{178} - D$ diagrams predicted by the KDA model and the extended model for different values of ρ_0 and $t_{\rm br}$. Calculations are performed for the same set of source's parameters as on Figure (16), but with $z = 0.1$ only.

6.2.6 Discussion

In this Section, I presented the dynamical evolution of FR II type sources and its evolutionary tracks through the power-linear size (hereafter $P_\nu - D$) diagrams (Shklovskii 1963). These diagrams, being a powerful tool for investigation of the time evolution of radio sources, show evolving (decreasing) radio luminosity of a source determined at a given frequency, P_ν, as a function of its linear size, D, enlarging with time.

Kaiser, Denett-Thorpe & Alexander (1997) presented the $P_\nu - D$ diagrams for the original KDA model applied to fiducial FR II type radio sources with parameters adopted according to the present knowledge about their physics. On the contrary, I presented here analogous diagrams for the case of terminated source's nuclear activity. They indicate the very strong effect of this termination on both linear size and radio luminosity of the lobes, especially for the values of $t_{\rm br}$ much lower than the actual age od a source, t. The characteristic breake of the $P_\nu - D$ curves is more rapid in the case of higher redshifts and lower values od β and ρ_0.

The radio power spectrum for the fiducial source (Figure (16)), plotted for the comparison of the influence of redshift and $t_{\rm br}$ on both KDA and extended model, shows that the strongest breaking of the spectra due to the rapid energy loses occurs for the higher redshift and the lower value of $t_{\rm br}$. One can conclude that both the power spectra and the P-D evolutionary tracks are in a good agreement with our knowledge about the FR II type radio sources and their energy loses.

I analysed also the relations between the source's age and its lobes velocity, as well as source's age and its lobes internal pressure, for the selected $P_\nu - D$ tracks. The instantaneous bow shock velocity v_h (cf. Figure (3)) is

$$v_h(t) = \frac{\partial}{\partial t} D(t) \tag{34}$$

and is reduced to differentiation of Eq. (25) that gives:

$$v_h(t) = \begin{cases} c_1 \frac{3}{5-\beta} \left(\frac{Q_{jet}}{\rho_0 a_0^\beta} \right)^{\frac{1}{5-\beta}} t^{\frac{\beta-2}{5-\beta}}, & t < t_{br} \\ c_4 D(t_{br}) t_{br}^{-c_4} t^{c_4-1}, & t \geq t_{br} \end{cases} \tag{35}$$

where $c_4 = \frac{2(\Gamma_c+1)}{\Gamma_c(7+3\Gamma_c-2\beta)}$.

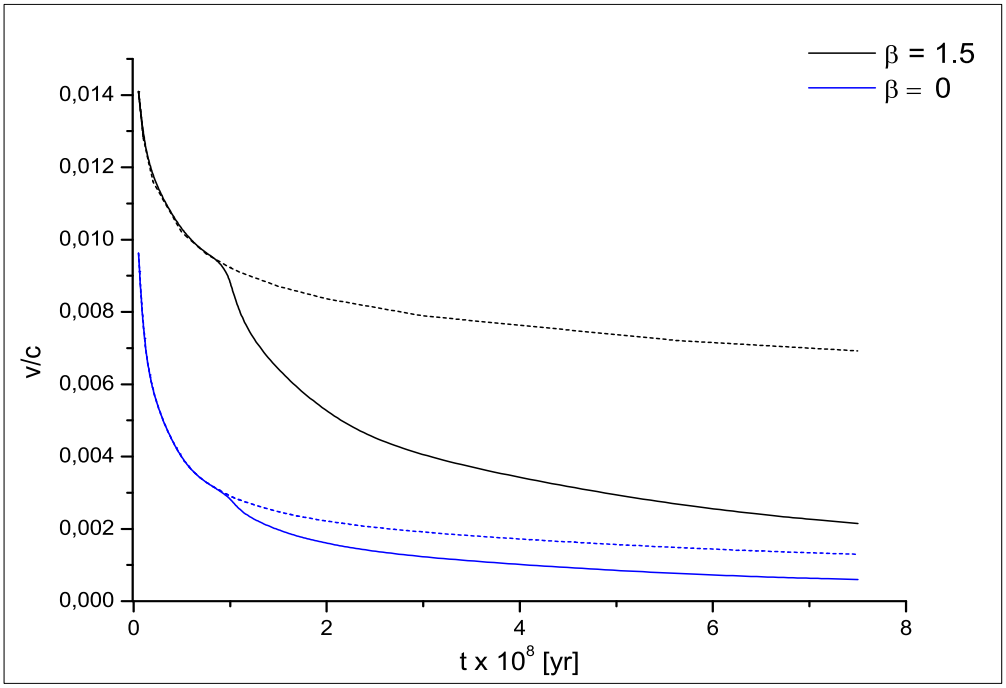

Figure 20: Velocity of expanding lobes vs. time. Solid curves correspond to the extended model of sources dynamics and dashed lines follows the KDA model of continuous activity. Parameters are the same as in the case of Figure (16), with $t_{\rm br} = 100$ Myr and $\Gamma_c = 5/3$.

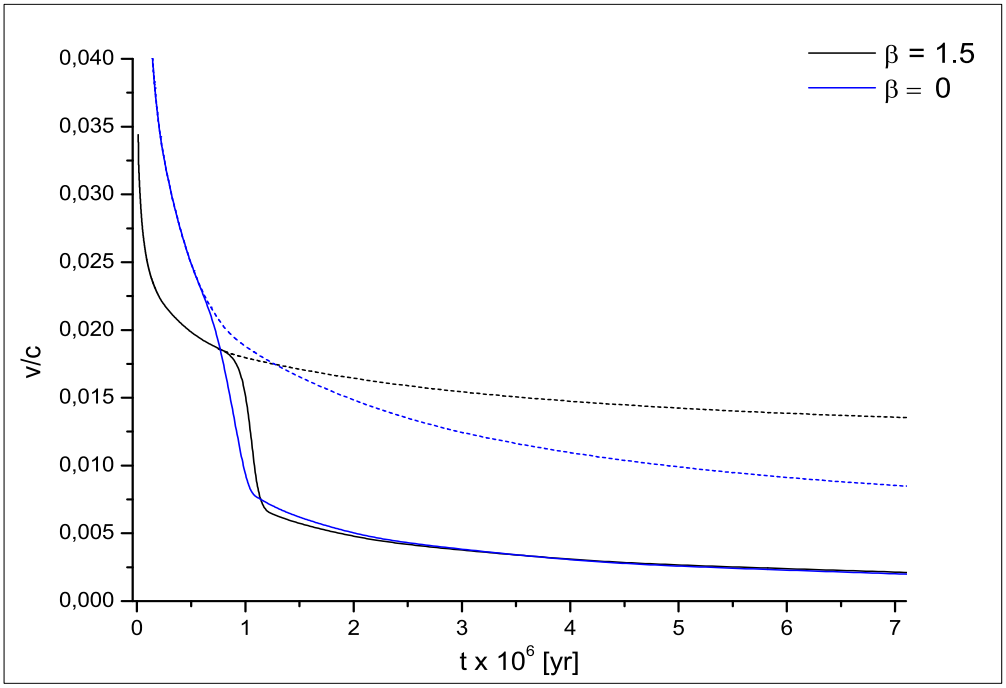

Figure 21: Velocity of expanding lobes vs. time - the same as in Figure (20), but for $t_{\rm br} = 1$ Myr.

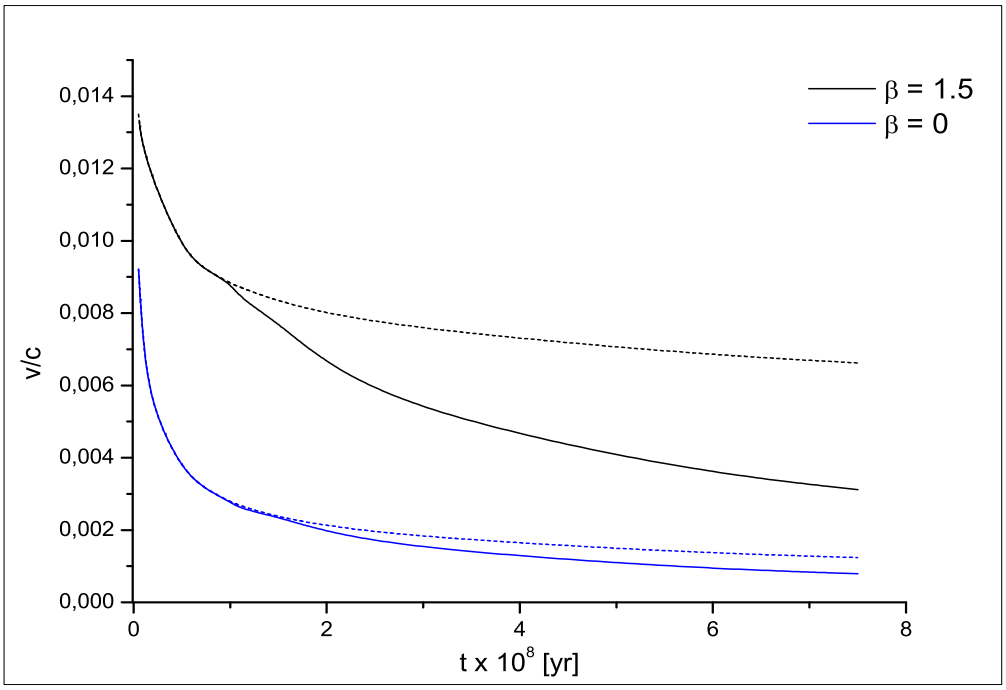

Figure 22: The same as in Figure (20), but for $\Gamma_c = 4/3$.

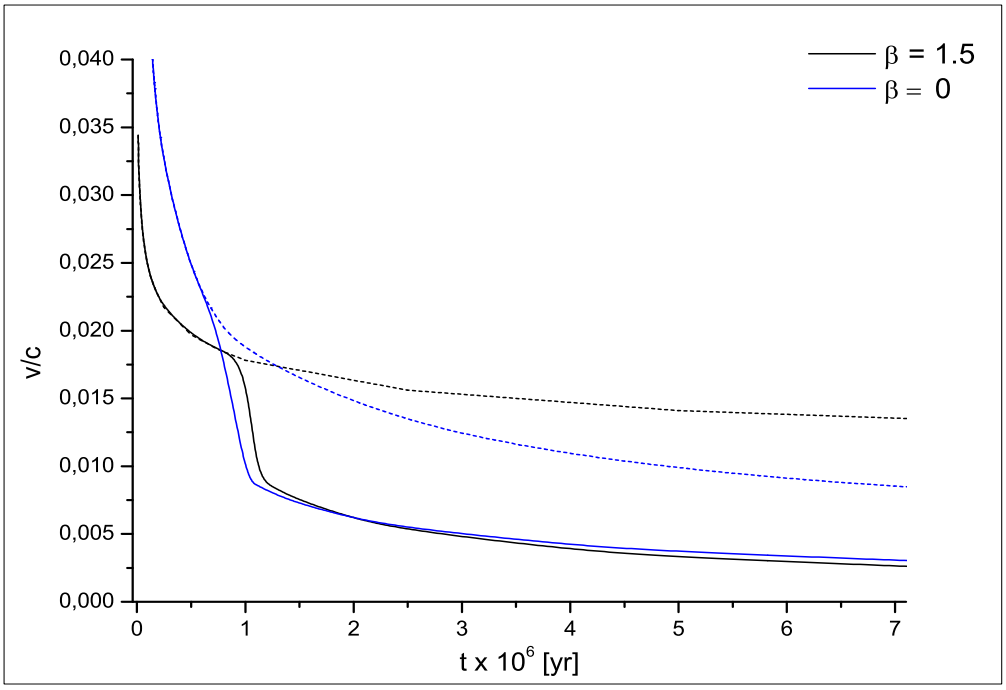

Figure 23: The same as on Figure (21), but for $\Gamma_c = 4/3$.

Figures (20) - (23) present evolution of the lobe's head velocity given as the ratio of c in function of the source's age for both KDA and extended model. It is worth to note that the rate of a decrease of this velocity depends not only on t_{br} and β exponent, but also is slightly different for the values of Γ_c (for relativistic and cold cocoon material). Diagrams indicate that the process of termination the source's activity strongly affects the rate of lobes propagation also. The difference of this rate calculated for continuum-injection and non continuum-injection model increases due to the higher value of β exponent, describing the density profile of the external medium.

In the case of young age of the source lobe's expansion velocity strongly depends on the density profile of that medium (cf. Figures (21) and (23)). Due to more and more advanced ageing of the radio source this dependence is rapidly declining. For radio sources with jet cut-offs (cf. Eq. (35)) it is even faster decreasing with age, because the β parameter is here relatively small contribution in the formula describing the lobe's head velocity, but, on the contrary, the same velocity begins to depend more strongly on the value of Γ_c as the source is ageing. It is visible also that for the assumed value of $\beta = 0$ the distinction in lobe's velocity resulting from both models is very difficult starting from a given source's age, and the same difference is much more explicit in the case of these two models calculated for $\beta = 1.5$

Following the discussion given by Kaiser & Cotter for their model B, I also assume that the time evolution of the lobes pressure, p_c (cf. Section 3.1), after switching off the sources nuclear activity, changes its former decrease according to formula:

$$p_c(t > t_{br}) = p_c(t_{br}) \left(\frac{t}{t_{br}} \right)^{-3\Gamma_c c_4} . \tag{36}$$

Figures (24) - (25) present the behaviour of internal pressure of fiducial source's expanding lobes due to source's growing age. Similarly to the lobe's head velocity analysis, this evolutionary tracks had been calculated for both KDA and extended model and for different values of β exponent. In the case of both models the slope of pressure's function is more steep for the $\beta = 1.5$, according to Eq. (36). Regardless of that factor the time evolution of lobe's internal pressure is faster and much more rapid in the extended model, what is in good agreement with out physical intuition - in the case of jet's termination not only the decrease of the lobe's head velocity, but also the gradual decline of that pressure is expected to be observed. It is also noteworthy that in the case of the extended model one can observed the exponential decay of the internal pressure that, starting on the particular age, is independent of the β value. Finally, the evolution of the lobe's internal pressure depends very weakly of the value of Γ_c.

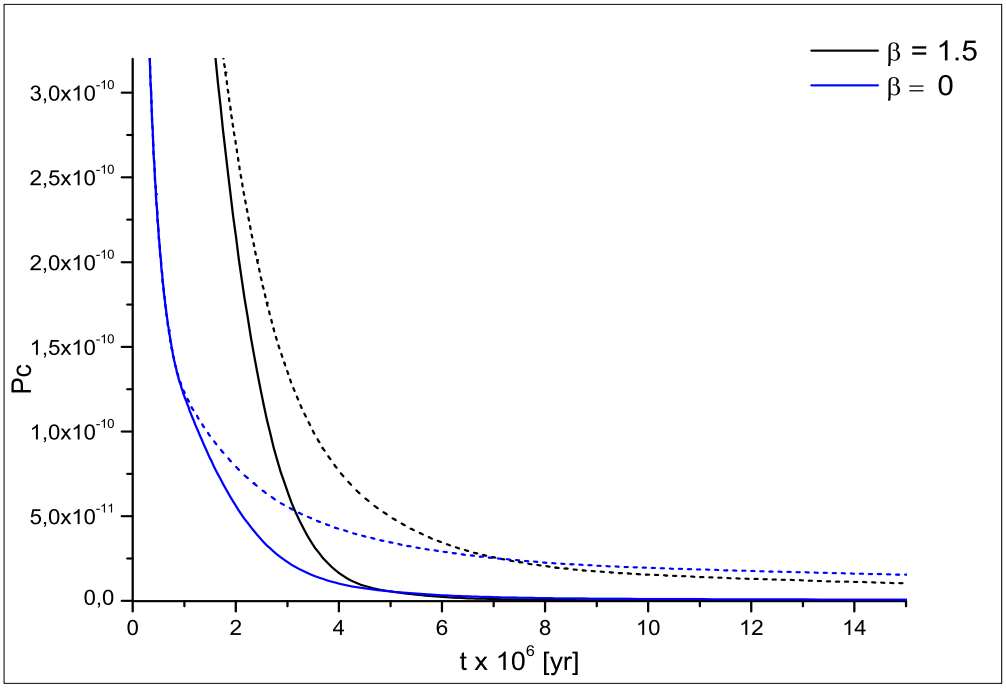

Figure 24: Internal pressure of expanding lobes vs. time. Solid curves correspond to the extended model of sources dynamics and dashed lines follows the KDA model of continuous activity. Parameters are the same as in the case of Figure (16), with $t_{\rm br} = 1$ Myr and $\Gamma_c = 5/3$.

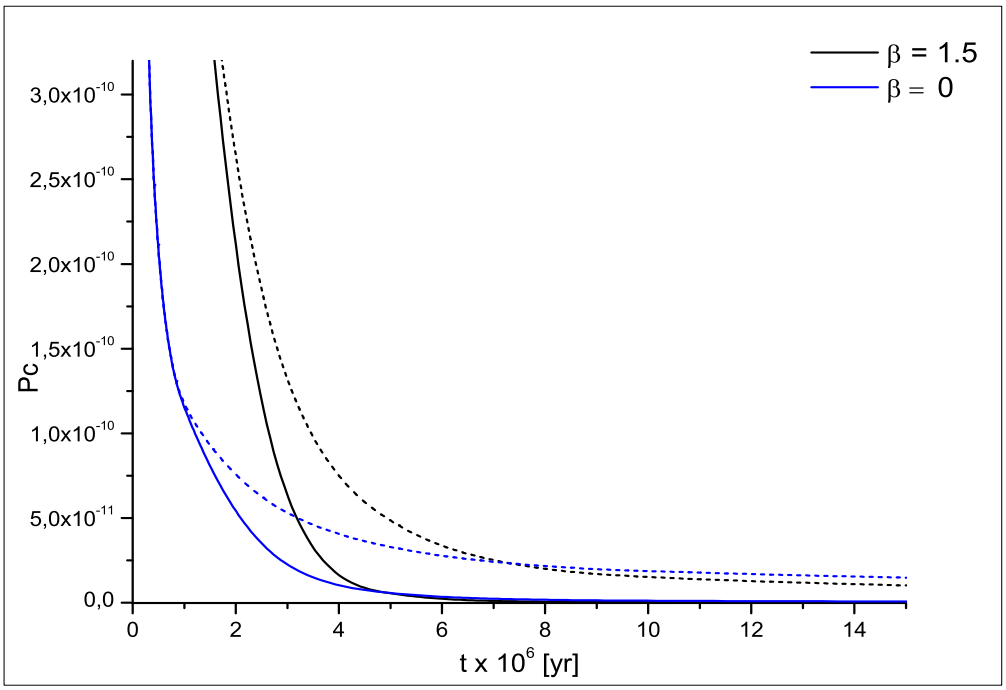

Figure 25: The same as on Figure (24), but for $\Gamma_c = 4/3$.

PART III

7 Application of the extended model to a few selected radio sources

In the previous Sections, I introduced the new, extended model of the dynamics and expected radio emission of FR II type radio sources, indicating the grounds for its development. As it is shown in Section 6.2.5, this new model predicts the shape of the radio spectra for sources with terminated activity, for which the KDA model is no longer applicable. To verify the accuracy of the model, I derive the spectra resulting from the "best age-solution" with the KDA model (cf. Machalski et al. 2007a) and these found with the extended model in order to compare the above model spectra with the observed data (radio spectra derived from multifrequency observations) in a small sample of real radio sources with steeply bent high frequency spectra.

The modelling procedure relies on fitting the values of free parameters of a given model to the observed data. Despite of its function of controlling the accuracy of the model, this procedure also allows us to study physical conditions in FR II type source, eg. the age vs. linear size relation for sources with steep radio spectra, and (in the case of the extended model only) to estimate the age at which their activity dims or even is terminated, which may be an important contribution for better understanding of the nuclear activity processes and time scales. Application of the extended model may also contribute to the evaluation of the properties of the intergalactic medium, especially in the case of high-redshifted radio galaxies with large sizes, that are a valuable tool for looking for a possible fluctuations of that medium in earlier cosmological epochs. The preliminary results presented in this Section indicate that the extended model reproduces the data with much better accuracy then the KDA model. Moreover, a typical time of the jet cuts-off can be estimated using this method.

7.1 Sample of examined radio sources

The extended model is applied to a small sample of various radio sources showing strong break-up in their radio spectra, probably due to the past jets cut-offs. One can expect that the model is especially useful in the case of studying the giant FR II type radio galaxies. For this reason two giant sources, J1428+3938 (Machalski et al. 2006) and J1453+3308 (Konar et al. 2006), large radio source with restarting activity (J1548−3216, Machalski et al. 2010), and two smaller 3C sources with bent spectra are included in this sample, as well as extremely high-redshifted radio galaxy 6C1232+3942 (Eales & Rawlings 1993). Table (9) presents the observational data and Figure (26) shows the radio maps for the sample sources.

Table 9: Observational data for the sample of FR-II type sources with strongly curved spectra.

3C217	z=0.898		LAS=12".1	R_t=4.0	
26 MHz	43000 ± 6000	10	750 MHz	4060 ± 208	10
38 MHz	39000 ± 5900	8	1400 MHz	2087 ± 63	6
74 MHz	25380 ± 2590	1	1400 MHz	2102 ± 63	15
86 MHz	24400 ± 1300	10	2695 MHz	1011 ± 80	10
151 MHz	15940 ± 798	15	4850 MHz	550 ± 49	11
178 MHz	12317 ± 616	10	4850 MHz	469 ± 9	15
327 MHz	8970 ± 359	15	10550 MHz	161 ± 3	15
365 MHz	8372 ± 121	4	10700 MHz	122 ± 38	10
408 MHz	7090 ± 215	15			
3C438	z=0.290		LAS=22"	R_t=2.7	
74 MHz	81560 ± 8160	1	750 MHz	14510 ± 800	5
178 MHz	46300 ± 3704	2	750 MHz	13700 ± 700	5
325 MHz	29940 ± 1123	3	1400 MHz	6855 ± 220	6
365 MHz	26402 ± 393	4	2695 MHz	3260 ± 150	5
408 MHz	25180 ± 1980	5	4850 MHz	1607 ± 143	11
408 MHz	23760 ± 1190	15	10700 MHz	40 ± 40	8
6C1232+3942	z=3.22		LAS=9"	R_t=3.0	
74 MHz	6520 ± 660	1	408 MHz	1130 ± 45	15
151 MHz	3320 ± 200	16	1400 MHz	255 ± 8	6
151 MHz	3270 ± 168	15	4850 MHz	40 ± 5	11
325 MHz	1630 ± 065	15	10550 MHz	16 ± 1	15
365 MHz	1472 ± 076	4			
J1428+3938	z=(0.5)		LAS=269"	R_t=3.4	
151 MHz	971 ± 109	9	408 MHz	270 ± 31	15
151 MHz	990 ± 95	16	1400 MHz	83 ± 4	6
232 MHz	810 ± 100	7	4860 MHz	13 ± 13	12
325 MHz	428 ± 34	3	10550 MHz	3 ± 2	15
J1453+3308	z=0.249		LAS=336"	R_t=3.8	
151 MHz	2165 ± 110	13	605 MHz	970 ± 75	13
178 MHz	2020 ± 200	13	1287 MHz	442 ± 34	13
240 MHz	1667 ± 250	13	1400 MHz	426 ± 36	13
325 MHz	1365 ± 140	13	4860 MHz	104 ± 8	13
334 MHz	1456 ± 112	13			
J1548−3216	z=0.1082		LAS=522"	R_t=2.9	
160 MHz	8400 ± 840	14	1384 MHz	1733 ± 87	14
334 MHz	4737 ± 710	14	2495 MHz	963 ± 30	14
619 MHz	3141 ± 252	14	4860 MHz	415 ± 42	14

References to the flux densities: [1]-VLSS, Cohen et al. (2007); [2]-4C, Pilkington & Scott (1965); [3]-WENSS, Rengelink et al. (1997); [4]-TXS, Douglas et al. (1996); [5]-Kühr et al. (1981); [6]-NVSS, Condon et al. (1998); [7]-Miyun, Zhang et al. (1997); [8]-Kellermann & Pauliny-Toth (1973); [9]-7C, Waldram et al. (1996); [10]-Laing & Peacock (1980); [11]-GB6, Gregory et al. (1996); [12]-Machalski et al. (2006); [13]-Konar et al. (2006); [14]-Machalski et al. (2010); [15]-B3-VLA, Vigotti et al. (1999); [16]-6CII, Hales et al. (1988).

The "largest angular size" (LAS) estimated from radio maps, are given in arc seconds. The R_t values are adopted from radio maps or earlier publications. The flux densities, given in Jy, are taken from various radio surveys (4C, 6C, 7C, WENSS, TXS, VLSS, NVSS, GB6) or from the "Cataloque of Radio Sources" compiled by Kühr et. al (1982). The flux density data from dedicated observations with the GMRT and VLA arrays for the outer lobes of J1453+3308 and J1548−3216 are taken from the original publications.

Table (10) presents the projected linear size of the sample sources, the presumed inclination angle of their jets' axis, θ, and the radio power at at least five observing frequiencies, i.e. their physical parameters used to confine free parameters of the models (cf. Section 3.3) both the KDA and the developed extended model (hereafter referred to as KDA EXT).

The linear size of the sources, D, and the radio powers, P_ν, are calculated from their angular size and flux densities given in Table 9, accorfing to the formulae:

$$D = 4.848 \cdot 10^{-6} L_A(z) \cdot LAS, \text{ and} \tag{37}$$

$$P_\nu = S_\nu L_D(z)^2 (1+z)^{(\alpha_\nu - 1)} \tag{38}$$

where $L_A(z)$ and $L_D(z)$ are angular and luminosity distances of a source, respectively, determined with the "Cosmological Calculator" of Wright (2006) assuming flat Universe with Hubble Constant H_0=0.71 $\mathrm{km\,s^{-1}Mpc^{-1}}$ and the ΛCDM model with cosmological parameters $\Omega_m = 0.27$ and $\Omega_\Lambda = 0.73$, and α_ν is index measured as the spectrum slope gradient calculated separately for every pair of the neighbouring radio flux densities.

It is worth noting that the frequency coverage of the radio spectra of some sample sources is wider than for the other ones, and these spectra contain the very extreme (low or high) flux values. In these cases the model fit is assumed to be much more precise than in those without information about the radio emission at extreme low and high frequencies. Moreover, for the sources with restarting activity (J1453+3308 and J1548−3216), Table (9) and (10) give the parameters or the outer, older lobes that are used to model their extended, outer FR II - type structure only.

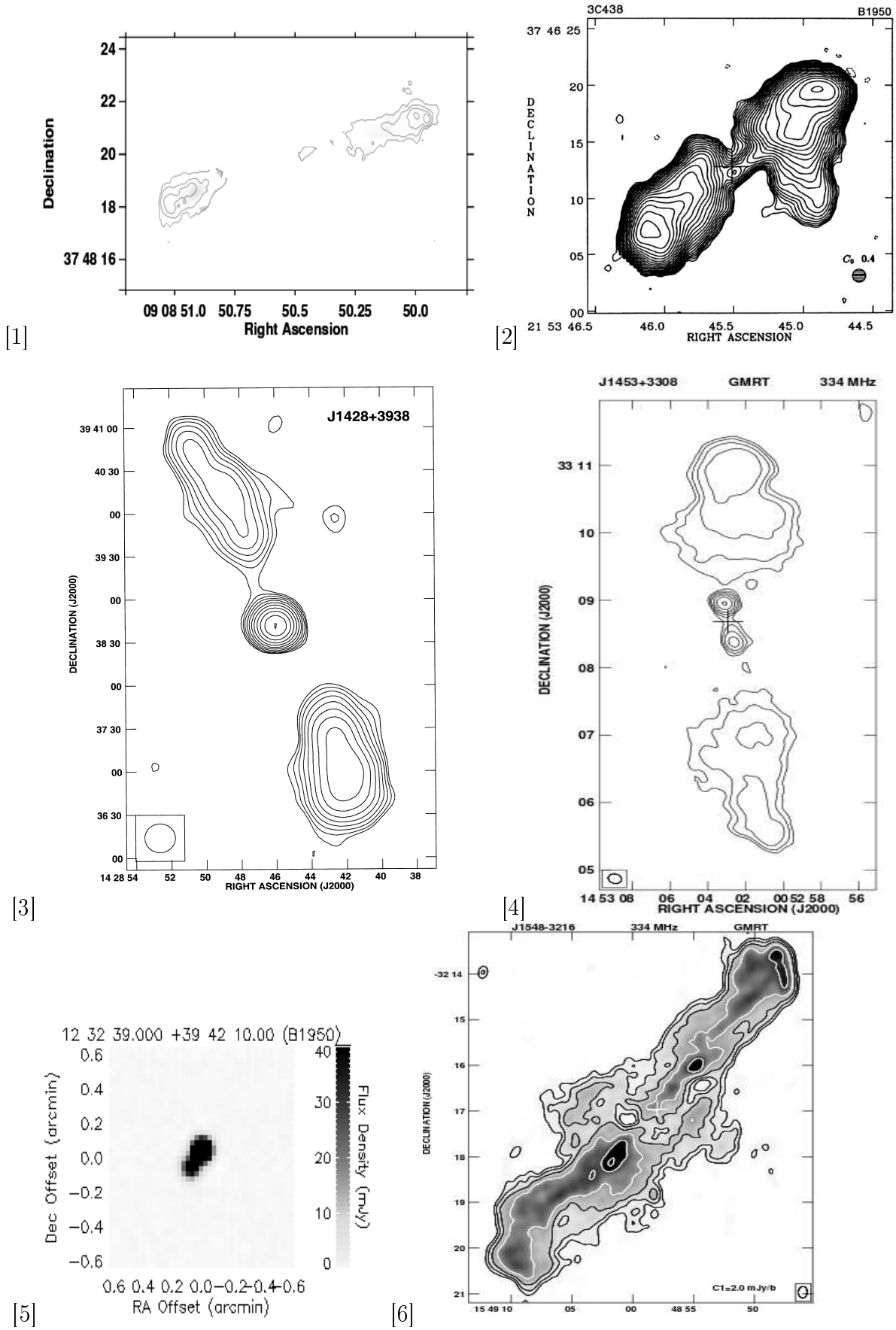

Figure 26: Radio maps of the sample sources: [1] VLA map of 3C217 at 4800 MHz, Best et al. (1997); [2] VLA map of 3C438 at 1452 MHz, Leahy & Perley (1991); [3] VLA map of J1428+3938 at 4860 MHz, Machalski et al. (2006); [4] GMRT map of J1453+3308 at 334 MHz, Konar et al. (2006); [5] VLA map of 6C1232+3942 at 1400 MHz (NVSS), [6] GMRT map of J1548-3216 at 334 MHz, Machalski et al. (2010).

7.2 Fitting procedure

The fitting procedure consists of two steps In the first one, I am searching for the best "age-solution" with the KDA model using the "DYNAGE" algorithm. However, as expected, the best fit model and the resulting spectrum are always poor as long as we try to reproduce observed highly-steepened spectrum with the model assuming the CI process of the energy supply to the radio lobes that is the case of KDA model. Therefore to solve this problem, I performed the KDA fits using only the low-frequency parts of the flux density data, i.e. rejecting the extremely high-frequency fluxes that increase curvature of the source's observed spectra.

Table 10: Physical data of the sample sources used to fit the KDA model. The (log) values of radio power are given in $\mathrm{WHz^{-1}s^{-1}}$.

	3C217	3C438	6C1232+3942	J1428+3938	J1453+3308	J1548−3216
D [kpc]	85	95	59	1630	1297	998
θ [^{o}]	70	90	70	90	90	90
log P_{74}	28.115	27.192	28.635			
log P_{151}	27.850		28.396	25.825	25.448	
log P_{160}						25.282
log P_{178}	27.816	26.955				
log P_{232}				25.718		
log P_{240}					25.351	
log P_{325}		26.780	28.225	25.532		
log P_{334}					25.288	25.029
log P_{605}					25.258	
log P_{619}						24.853
log P_{1384}						24.606
log P_{1400}	27.253	26.156	27.590	24.885	24.778	
log P_{2495}						24.363
log P_{2695}	26.897	25.833				
log P_{4850}	26.615	25.585	26.667			
log P_{4860}				23.994	24.198	24.008
log P_{10550}			26.394			

Following the original KDA's analysis, I adopted their Case 3 where both the cocoon material and the ambient medium are assumed to be described by the "cold" equation of state (i.e. $\Gamma_{\rm c} = \Gamma_{\rm x} = 5/3$). I also assume the equipartition condition for the initial ratio of the energy densities between the source's magnetic field and relativistic particles, $\zeta \equiv u_{\rm B}/u_{\rm e} = (1+p)/4$, that is well supported by the X-ray observations of the lobes in powerful radio sources (Kataoka & Stawarz 2005). Finally, following Daly (1995) and Blundell et al. (1999), I adopt $\beta = 1.5$ for all of the examined sources. The remaining model free parameters are the same as in Table (4) in Section 5.4.

The final result of this step is determination of four parameters of the model, i.e. the initial particle-energy distribution described by α_{inj}, the fitted age, t, the corresponding values of the jet power, Q_{jet}, and the central core density, ρ_0.

In the second step, I select a number of values for the jet "switch-off", t_{jet}, fulfilling $t_{jet} < t$. For each of these values, Eqs. (32), i.e. Eq. (8) and Eq. (33) are solved numerically, providing the sources power, $P_{\nu_{em}}$, at the number of frequencies (in the source frame) corresponding to a given t_{jet} value. A value of t_{jet} providing the best fit of the extended model predictions to the observed radio spectrum is considered as the time of the jet termination, t_{br}. The best fit is determined using the least-squares method by minimizing the expression:

$$\chi^2_{red} = \frac{1}{n-3} \sum_n \left(\frac{S_{\nu_0} - S_{MOD}}{\Delta S_{\nu_0}} \right)^2 , \tag{39}$$

where S_{ν_0} and ΔS_{ν_0} are flux densities and their errors given in Table (9), and S_{MOD} are the model flux densities re-calculated from the model values of $P_{\nu_{em}}$ according to

$$S_{MOD} = P_{\nu_{em}} \left(\frac{1+z}{L_D^2(z)} \right) = P_{\nu_{0(1+z)}} \left(\frac{1+z}{L_D^2(z)} \right) . \tag{40}$$

7.3 Application of different dynamical models to the sample sources

The KDA EXT model developed in this Section was used to fit the observed radio spectra of the sample sources. In order to compare this model's results with similar results obtained for the sample sources (including these from KDA model for entire sources or their radio lobes only), I calculated the values of χ^2_{red}, determining so-called godness of the fit, for all of the best fits of the KDA models and the best fit of the KDA EXT model.

Table (11) presents values of the model free parameters and some derivative physical parameters of the sample sources derived from their best fit of the KDA EXT model. These physical parameters, determined after the jet "switch off", are: the cocoon pressure, $p_{\rm c}$, the total emitted energy, $\rm U_c$, strength of the magnetic field, $\rm B_{eq}$, and radial expansion speed of the cocoon's head, $\rm v_h$. The values of these parameters are calculated for $\rm t > t_{br}$ in contrast to similar quantities presented for the sources analysed in Section 4. Eg. $p_{\rm c}$ for $\rm t > t_{br}$ is calculated with Eq. (36), $\rm U_c$ is given by the formula $\rm U_c(t) = u_c(t) V_c(t) = p_c(t) V_c(t)/(\Gamma_c - 1)$; $\rm B_{eq}(t)$ is calculated with Eq. (24) and $\rm v_h(t)$ with (35).

The list presented below is a short compilation of the results obtained for the individual sources from the sample. Their best-fitting models are then compared to observed spectra are summarized in tables (12)-(17). The resulting spectra are plotted in Figures (27) - (32).

Table 11: Physical parameters of the radio sources from the sample derived from the best fit of the KDA EXT model.

IAU name	t [Myr] (1)	t_{br} [Myr] (2)	$\alpha_{\rm inj}$ (3)	$\log Q_{\rm jet}$ [W] (4)	$\log \rho_0$ [kg/m^3] (5)	$\log p_{\rm c}(t>t_{br})$ [N/m^2] (6)	$\log U_{\rm c}$ [J] (7)	$B_{\rm eq}$ [nT] (8)	$v_{\rm h}/c(t>t_{br})$ (9)
3C217	1.91	1.89	0.58	39.30	−22.49	−10.24	52.79	4.59	0.057
3C438	6.9	6.8	0.60	38.49	−22.12	−10.65	53.07	2.19	0.016
6C1232+3942	1.60	1.57	0.62	39.71	−21.44	−8.94	53.41	15.89	0.031
J1428+3938	158	145	0.58	37.87	−22.16	−13.05	53.53	0.15	0.008
J1453+3308	91.2	82	0.51	37.77	−23.35	−13.58	53.29	0.08	0.017
J1548−3216	79.4	67	0.60	37.61	−23.06	−13.36	52.94	0.11	0.013

7.3.1 3C217

Table 12: Flux densities resulting from KDA and KDA EXT model for 3C217 and their godness of the fit to the observed data.

$\nu_0/\nu_0(1+z)$	$S_{\nu_0} \pm \Delta S_{\nu_0}$	S_{MOD}	S_{MOD}
		KDA	KDA EXT
26/50	43000 ± 6000	60184	54888
38/72	39000 ± 5900	46610	42314
74/141	25380 ± 2600	28806	25971
86/163	24400 ± 1300	25614	23146
151/287	15940 ± 798	16614	14876
178/338	12417 ± 616	14571	13016
327/621	8970 ± 359	8861	7825
365/693	8372 ± 121	8081	7120
408/774	7090 ± 215	7336	6449
750/1424	4060 ± 208	4310	3737
1400/2657	2086 ± 62	2441	2077
1400/2657	2102 ± 63	2441	2077
2695/5115	1011 ± 80	1314	1090
4850/9205	469 ± 90	739	598
10550/20024	161 ± 30	345	254
10700/20309	122 ± 38	334	247
		$\chi^2_{red} = 14.31$	$\chi^2_{red} = 12.31$

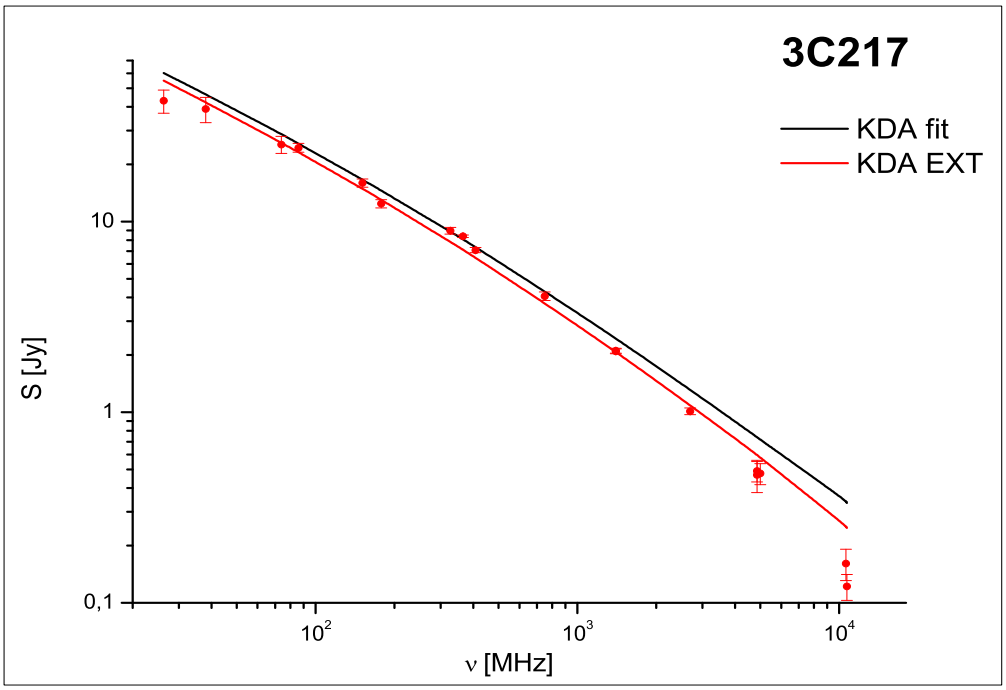

Figure 27: The best KDA fit (black solid line) and KDA extended fit (red solid line) for the radio galaxy 3C217. The values of flux density and frequency are presented in logarithmic scale. The observed flux densities and their errors are marked with the red data points.

7.3.2 3C438

Table 13: Flux densities resulting from KDA and KDA EXT model for 3C438 and their godness of the fit to the observed data.

$\nu_0/\nu_0(1+z)$	$S_{\nu_0} \pm \Delta S_{\nu_0}$	S_{MOD}	S_{MOD}
		KDA	KDA EXT
74/96	81560 ± 8160	105207	101703
178/230	46300 ± 3704	49698	48232
325/419	29940 ± 1123	28929	28011
365/471	26402 ± 393	25962	25138
408/526	25180 ± 1980	23406	22664
408/526	23760 ± 1190	23406	22664
750/968	14510 ± 800	13132	12657
750/968	13700 ± 700	13132	12657
1400/1806	6855 ± 220	7118	6829
2695/3477	3260 ± 150	3684	3502
4850/6257	1607 ± 143	2011	1889
10550/13610	640 ± 40	892	808
		χ^2_{red} =8.07	χ^2_{red} =5.98

Table 14: Flux densities resulting from KDA and KDA EXT model for 6C1232+3942 and their godness of the fit to the observed data.

$\nu_0/\nu_0(1+z)$	$S_{\nu_0} \pm \Delta S_{\nu_0}$	S_{MOD}	S_{MOD}
		KDA	KDA EXT
74/312	6520 ± 660	7869	7456
151/637	3320 ± 200	3684	3432
151/637	3270 ± 168	3684	3432
325/1372	1630 ± 65	1609	1461
365/1540	1472 ± 76	1421	1281
408/1722	1130 ± 45	1255	1136
1400/5908	255 ± 8	316	268
4850/20467	40 ± 5	65	55
10550/44521	16 ± 1	26	15
		$\chi^2_{red} = 38.07$	$\chi^2_{red} = 4.70$

Table 15: Flux densities resulting from KDA and KDA EXT model for J1428+3938 and their godness of the fit to the observed data.

$\nu_0/\nu_0(1+z)$	$S_{\nu_0} \pm \Delta S_{\nu_0}$	S_{MOD}	S_{MOD}
		KDA	KDA EXT
151/227	971 ± 109	991	891
151/227	990 ± 95	991	891
232/348	810 ± 100	656	582
325/488	428 ± 34	471	413
408/612	270 ± 31	376	326
1400/2100	83 ± 4	107	83
4860/7290	13 ± 3	29	15
10550/15825	3 ± 2	13	4
		$\chi^2_{red} = 21.91$	$\chi^2_{red} = 1.94$

Table 16: Flux densities resulting from KDA and KDA EXT model for J1453+3308 and their godness of the fit to the observed data.

$\nu_0/\nu_0(1+z)$	$S_{\nu_0} \pm \Delta S_{\nu_0}$	S_{MOD}	S_{MOD}
		KDA	KDA EXT
151/189	2165 ± 110	2500	2399
178/222	2020 ± 200	2272	2158
240/300	1667 ± 250	1830	1751
325/406	1365 ± 140	1467	1378
334/417	1456 ± 112	1437	1347
605/756	970 ± 75	894	843
1287/1608	442 ± 34	463	426
1400/1749	426 ± 26	429	394
4850/6058	104 ± 8	129	115
		$\chi^2_{red} = 3.84$	$\chi^2_{red} = 2.09$

Table 17: Flux densities resulting from KDA and KDA EXT model for J1548−3216 and their godness of the fit to the observed data.

$\nu_0/\nu_0(1+z)$	$S_{\nu_0} \pm \Delta S_{\nu_0}$	S_{MOD}	S_{MOD}
		KDA	KDA EXT
160/177	8400 ± 840	8705	8391
334/370	4737 ± 710	5405	4975
619/686	3141 ± 252	3379	3096
1384/1534	1733 ± 87	1786	1577
2495/2765	963 ± 30	1059	917
4860/5386	415 ± 42	569	476
		$\chi^2_{red} = 8.66$	$\chi^2_{red} = 2.61$

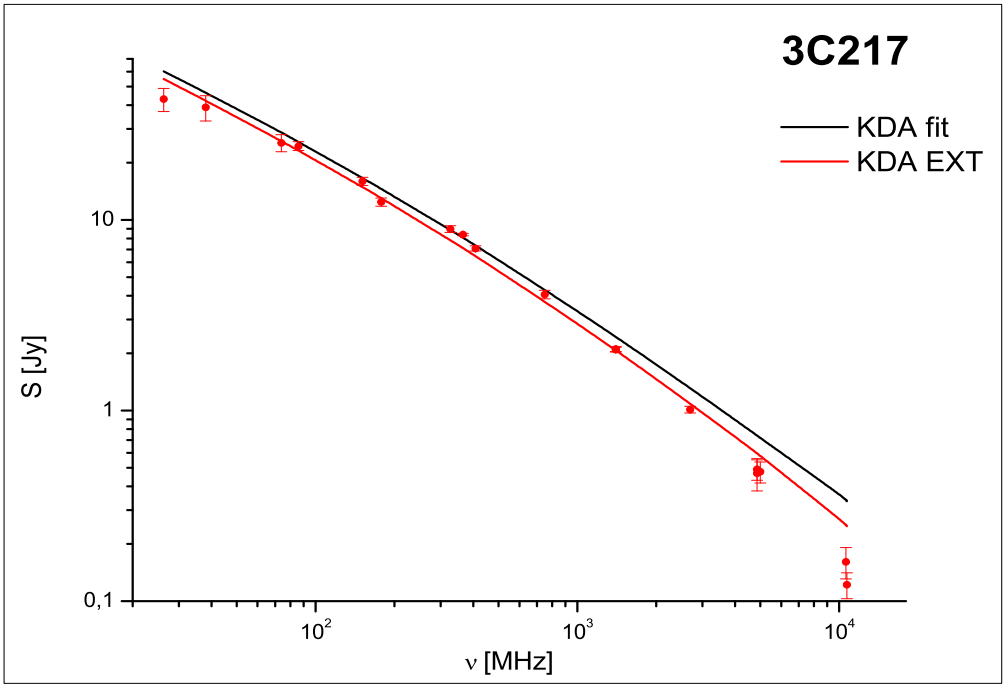

Figure 28: The best KDA fit (black solid line) and KDA extended fit (red solid line) for the radio galaxy 3C217. The values of flux density and frequency are presented in logarithmic scale. The observed flux densities and their errors are marked with the red data points.

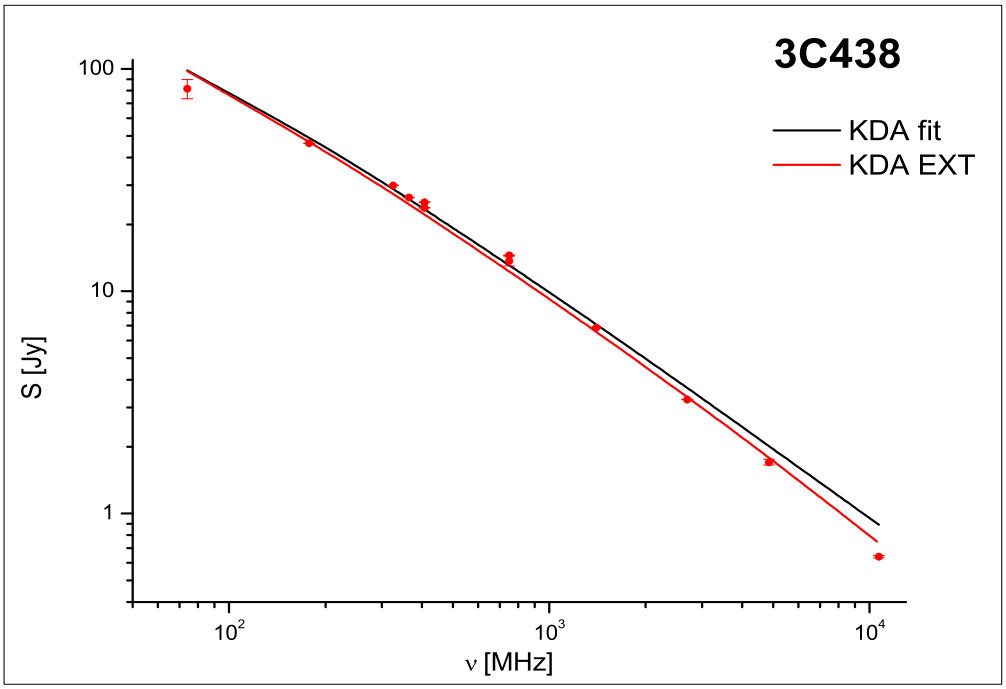

Figure 29: The same as Figure (27) but for 3C438.

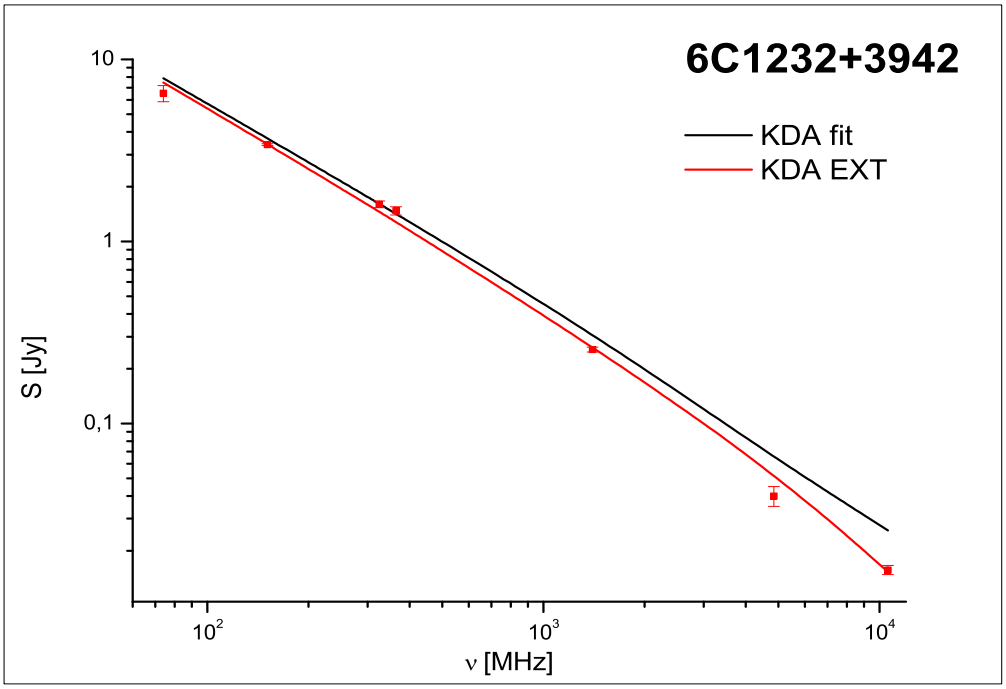

Figure 30: The same as Figure (27) but for 6C1232+3942.

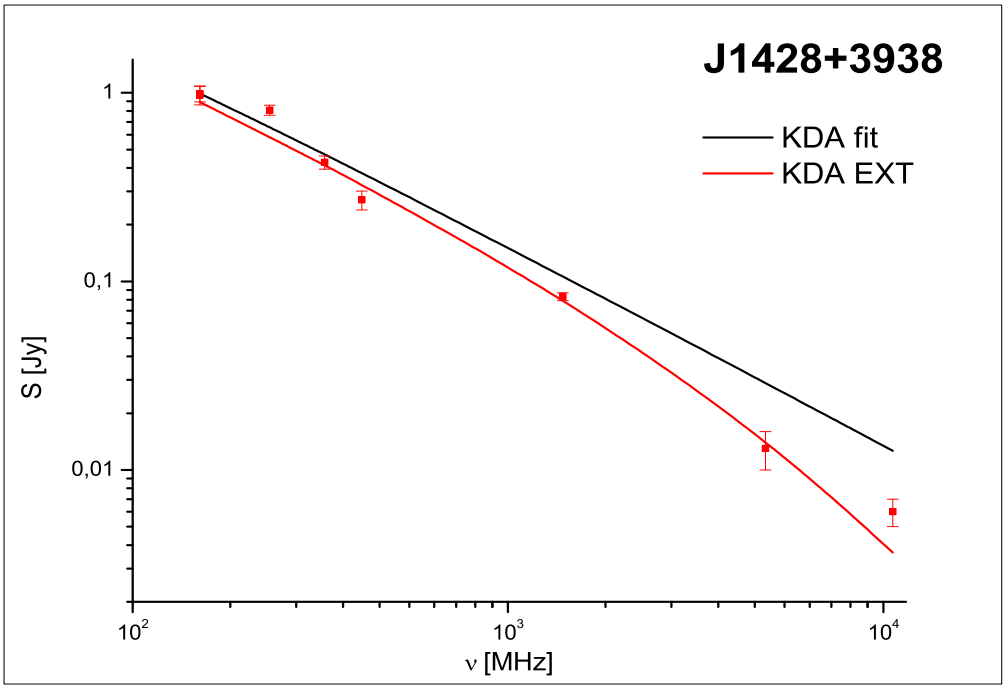

Figure 31: The same as Figure (27) but for J1428+3938.

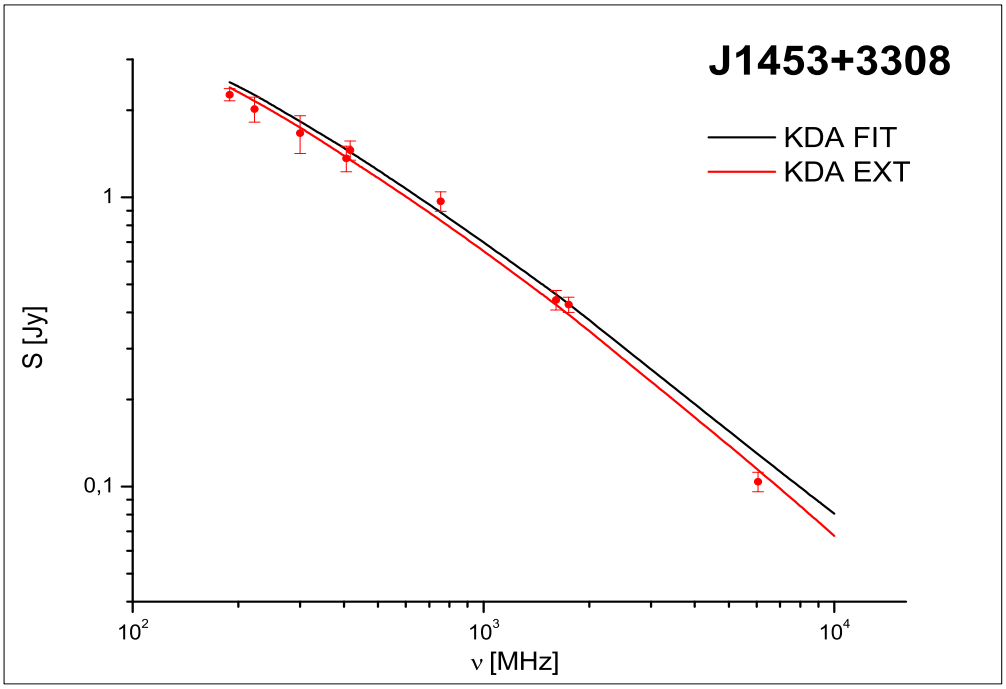

Figure 32: The same as Figure (27) but for J1453+3308.

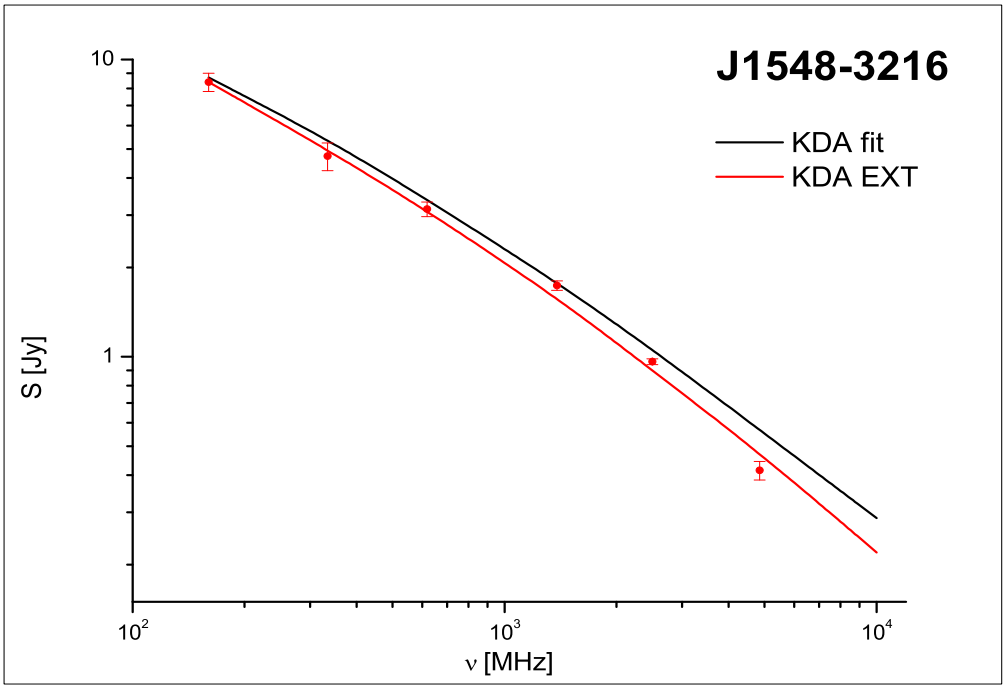

Figure 33: The same as Figure (27) but for J1548-3216.

7.4 Discussion and final conclusions

In this Section, I developed a new model for the dynamical evolution of the lobes of FR II type radio galaxies after the jets stopped supplying them with the energy. The best fit of this model (KDA EXT) to the observed radio spectra for the small sample of radio sources with steep and strongly curved radio spectra is was determined in order to evaluate the accuracy of this new model.

These preliminary results indicate that KDA EXT model can provide a satisfactory solution for the case of radio sources with presumed stopped activity. However, the agreement of the resulting fit with the observed radio spectra is high for some certain radio sources only. The plots and data lists presented above suggest that in the case of giant and very old radio sources (J1428+3938, J1453+3308 and J1548−3216) the superiority of the KDA EXT model fit over KDA fit is evident. The high accuracy of that fit is also noticeable in the case of high-redshifted radio galaxy 6C1232+3942

On the contrary, in the case of 3C217 and 3C438 the KDA EXT fit to the observed spectra differ significantly from the shapes of these spectra. This effect is visible especially for the medium and low frequencies. In these cases determined the age of jet's cut-off and other source's parameters (Table (11)) should be considered as very uncertain. One may notice also that KDA EXT fits do not differ significantly from the KDA fits for these sources. 3C438 χ^2 values calculated for both model's fits are almost the same.

I suggest that possible reasons of this model/observable inconsistency may be:

— more complicated changing of the rate of particles transport in jets, not taken into account while constructing of KDA EXT model, i.e. the situation when jet's activity is not simply stopping, but undergo with temporarily weakening (and, eventually, resuming),

— not including in the model some unknown initial energy distribution in the lobe's head, different from the one implied by the KDA model,

— any other, unknown differences in the dynamics of FR II type radio sources showing highly-steepened spectra, demanding new approach to the understanding of the physics of these sources,

— Inaccuracy in the determining of initial, pure KDA model's parameters obtained for certain sources and then used to perform a KDA EXT fit. It is very probable in the case of 3C438, where both KDA and KDA EXT fits are poor and their χ^2 values are very high.

Taking into account all the above, one can conclude that the KDA EXT model developed and presented in this Section is an appropriate tool for solving the problem of modeling the strongly curved spectra of FR II radio galaxies with large linear sizes, i.e. giant radio galaxies and DDRG with restarting activity (their older radio structures). However, it does not work properly in the case of some other radio sources with curved spectra, especially the ones that does not exhibit the characteristics of a typical old

and very large sources, but also have strongly spectra curved on the high frequency part.

8 References

Allen S.W. et al., 2006, MNRAS, 372, 21
Adelman-McCarthy et al., 2007, ApJ Suppl. Ser., 172, 634
Arshakian T.G., Longair M.S., 2000, MNRAS, 311, 846
Baade M., Minkowski R., 1954, ApJ, 119, 206
Barai P., Wiita P.J., 2006, MNRAS, 372, 381
Barthel P.D., Miley G.K., 1988, Nature, 333, 319
Becker R.H. et al., 1995, ApJ, 450, 559
Belsole E. et al., 2007, MNRAS, 381, 1109
Best P.N. et al, 1997, MNRAS, 292, 758B
Blandford R.D., Znajek R., 1977, MNRAS, 179, 433
Blandford R.D., 1999, KITP Program: Black Hole Astrophysics
Blandford R.D., Rees M.J., 1974, MNRAS 169, 395
Blundell K.M. et al., 1999, AJ, 117, 677
Brocksopp C. et al., 2011, MNRAS, 410, 484
Cassano R. et al., 2007, MNRAS, 378, 1565
Cohen A.S. et al., 2007, AJ, 134, 1245
Condon J.J. et al., 1998, AJ, 115, 1693
Cotter G., 1998, ASSL, Eds. M.N. Bremer et al. (Dordrecht: Kluwer Academic Publishers), p. 233
Cotter G. et al., 1996, MNRAS, 281, 1081
Croston J.H. et al., 2008, MNRAS, 386, 1709
Daly R.A., 1995, ApJ, 454, 580
Douglas J.N., 1996, VizieR Online Data Catalog, 8042
Eales S.A., 1985, MNRAS, 217, 149
Eales S.A., Rawlings S., 1993, ASPC, 41, 313
Fanaroff R., Riley C.S., 1974, MNRAS, 167, 31
Gopal-Krishna, Wiita P.J., 1987, MNRAS, 226, 531
Gregory P.C. et al., 1996, ApJ Suppl. Ser., 103, 427
Griffith M.R. et al., 1995, ApJ Suppl. Ser., 97, 347
Hales S.E.G. et al., 1988, MNRAS, 234, 919
Kaiser C.R., Alexander P., 1997, MNRAS, 286, 215
Kaiser C.R., Best P.N., 2007, MNRAS, 381, 1548
Kaiser C.R., Cotter G., 2002, MNRAS, 336, 649
Kaiser C.R. et al., 1997, MNRAS, 292, 723
Kaiser C.R., 2000, A&A, 362, 447
Kapahi V.K., 1989, AJ 97, 1
Kardashev N.S., 1962, SvA, 6, 317
Kataoka J., Stawarz, Ł, 2005, ApJ, 622, 797
Kellermann K.I., Pauliny-Toth I.I.K.,1973, AJ, 78, 828

King, I.R., 1972, Apj, 174, L123
Konar C. et al., 2006, MNRAS, 372, 693
Komissarov W., Gubanov W., 1994, A&AS, 285, 27
Kozieł-Wierzbowska D., 2008, Ph D Thesis, Jagellonian Univ., Kraków
Kühr H. et al., 1981, A&A Suppl. Ser., 45, 367
Kuligowska E. et al., 2009, AcA, 59, 431
Laing R.A., Peacock J.A., 1980, MNRAS, 190, 903
Laing R.A. et al., 1983, MNRAS, 204, 151
Lara L. et al., 2000, A&A, 356, 63
Lara L. et al., 2001, A&A, 370, 409
Leahy J.P., Perley, R.A., 1991, ApJ, 102, 2
Longair M.S., Riley J.M., 1979, MNRAS, 188, 625
Machalski J. et al., 2006, A&A, 454, 85M
Machalski J. et al., 2007a, A&A, 462, 43
Machalski J. et al., 2007b, AcA, 57, 227, Paper I
Machalski J. et al., 2008, Apj, 679, 149
Machalski J. et al., 2009, MNRAS, 395, 812
Machalski J. et al., 2010, A&A, 510, A8
Machalski J., 2011, MNRAS 413, 2429
Manolakou K., Kirk J.G., 2002, A&A 391, 127
McGilchrist M.M. et al., 1990, MNRAS, 246, 110
Merrit D., Ekers R.D., 2002, Science, 297, 1310
Murgia M., 1996, PhD Laurea Thesis, Univ. Bologna
Nilsson K. et al., 1993, ApJ, 413, 453
Pacholczyk A.G., 1970, "Radio Astrophysics" (San Francisco; Freeman)
Pilkington J.D.H., Scott P.F., 1965, MNRAS, 69,183 Rengelink R.B. et al., 1997, A&A Suppl. Ser., 124, 259
Riley J.M.W. et al., 1999, MNRAS, 306, 31
Shklovskii I.S., 1963, SvA, 6, 465
Schoenmakers A.P. et al., 2000, MNRAS, 315, 371
Sikora M., 2009, Astron. Nachr., 330, 291
Sikora M. et al., 2007, ApJ, 658, 815
Subrahmanyan R., Saripalli L., 1993, MNRAS, 260, 908
Subrahmanyan R. et al., 1996, MNRAS, 279, 257
Thompson D. et al., 1994, ApJ, 108, 3
Vigotti M. et al., 1999, A&A Suppl. Ser., 139, 359
Waldram E.M. et al., 1996, MNRAS, 282, 779
Willis S. et al., 1974, Nature, 250, 625
Wilson A.S., Colbert E.J.M., 1995, ApJ, 438, 62
Wright E., 2006, PASP, 118, 1711
Zhang X. et al., 1997, A&A Suppl. Ser., 121, 59